AN INVESTIGATION INTO THE CAUSE OF THE PERSISTENCE OF REGULAR REFLECTION

Terence Herron

A dissertation submitted to the Faculty of Engineering and the Built Environment, University of the Witwatersrand, in fulfilment of the requirements for the degree of Master of Science in Engineering.

Johannesburg, February 2011

Declaration

I declare that this dissertation is my own, unaided work. It is being submitted for the Degree of Master of Science in Engineering at the University of the Witwatersrand, Johannesburg. It has not been submitted previously for any degree or examination in any other University.

Terence John Gordon Herron

13 February 2011

Abstract

This research was undertaken to attempt to resolve a discrepancy between observations and theoretical predictions in shock wave reflections. Known as the von Neuman Paradox in this context, it is the failure of theory to predict when reflection geometry of a shock wave reflecting off a wedge inclined to its path will take the form of regular or Mach reflection, reflection geometries that are characterised by two and three shock waves respectively. The theory predicts transition at a lower Mach number than has been repeatedly observed, for a given wedge angle. It has been postulated that the cause of the discrepancy is due to thermal and viscous transport phenomena on the surface of the reflecting wedge. The proposed mechanism is that the thermal and viscous interaction of the shock wave with the surface creates a boundary layer that relaxes the assumptions of the theory. This postulation has been borne out by numerical investigation and an experimental investigation that is free from boundary layer effects at a single wedge angle. That investigation, like the two angles investigated in this research, reflected a pair of equal strength shock waves symmetrically off each other in a manner that is representative of shock wave reflection off a wedge. The inferred wedge, formed by the plane of symmetry of the shock reflection, is free from the boundary layer effects that are postulated to be the cause of the discrepancy. The research presented here found that the two angles investigated did not suffer from a persistence of regular reflection within experimental accuracy. For the 20° wedge a transition Mach number of 1.022 was found when the transition value calculated from the detachment criterion was nearest at Mach 1.018. The experiment representative of a 48° wedge indicated transition at Mach 1.372 which is almost identical to the sonic criterion's predicted value of Mach 1.376. These results broaden the range of the experimental validation that surface transport phenomena are the cause of the persistence of regular reflection, as the observations on an adiabatic, inviscid surface imply that there is no persistence.

Contents

List of figures

List of tables

Nomenclature

Symbol	Description	Units
x	Distance	mm
t	Time	s
M	Mach	*
v	Velocity	m/s
a	Speed of sound	m/s
T	Temperature	°K
γ	Ratio of specific heats	*
R	Specific gas constant	J/(kg·°K)
p	Pressure	Pa
θ	Angle subtended by flow into a oblique shock wave	rad
ϕ	Angle subtended by flow out of an oblique shock wave	rad
χ	Triple point trajectory angle	rad
ψ	Mis-synchronisation	mm
δ	Boundary layer thickness	mm
δ*	Displacement thickness	mm
ε	Angle change in wall due to displacement thickness	rad

*Dimensionless

1. Introduction

Shock wave phenomena are of practical importance in diverse applications from aerodynamic effects on supersonic aircraft, to effects within the exhaust of jet engines and rocket motors, to mine-blasting and the breaking up of kidney stones. As a result the ability to predict their behaviour and effects is of considerable importance and practical use.

In many of the phenomena described above the area of interest involves a shock wave interacting with the surface of a body, potentially at an angle, i.e. the shock originating from the intake of a fighter-aircraft impinging on the wing or a shock wave from blasting reflecting off the walls of a mine-tunnel.

To understand and predict the forces and pressures that result from these interactions an appreciation and certainty of the fundamental physics is required. To investigate a three dimensional phenomenon's fundamentals an investigation of a two-dimensional analogue that is amenable to three dimensional generalisation is often the most feasible approach.

When a shock wave encounters a wedge inclined at an oblique angle to its direction of travel it can reflect off its surface in a number of different ways. Each type of reflection is characterised by different reflection geometries that are dependent on the Mach number of the incident shock wave and the angle that the surface is inclined to with respect to the shock wave. It is important to be able to distinguish which type of reflection geometry will result from a known strength of incident shock wave and surface inclination as the different reflection geometries result in different pressures and temperatures on the reflecting surface, which is of practical significance to many applications.

Two of the simpler types of reflection are 'regular' and 'Mach' reflection, reflection processes that occur at the weakest incident shock wave strengths. The transition between the two types of reflection has been subject to debate since the earliest experimental efforts to determine the transition between the types of reflection were carried out. Simply put, experiments to validate the theoretically-predicted transition Mach number are systematically in error. The experiments consistently resulted in regular reflection being observed well into the domain of Mach reflection. As there have been no experimental validation of the postulated transition criteria it has not been possible to identify which of the proposed mechanisms of transition is the correct one.

Other investigations that have not experienced the persistence of regular reflection have suffered from significant errors that are a fundamental part of the experimental technique, rendering their findings inconclusive. The internal-cavity type experiments reflect shock waves off a v-shaped end wall and use the symmetry plane of the reflected waves as a reflecting surface.

It was postulated that the cause of the discrepancy was due to a failure in the assumptions of the transition criteria. This investigation aims to obtain an ideal result by accurately simulating the assumptions of the theory, and hence by the distinction between this and ‘normal’ investigations identify the cause of the discrepancy between theory and observation.

The latter of the two angles investigated in this research is located in a region in the domain of regular to Mach reflection transitions where the transition criteria differ significantly in the predicted transition point. This should allow the identification of which transition criterion is correct, in addition to the main task of identifying the cause of the persistence of regular reflection.

Other investigations implied that the amount of persistence varied with both the Reynolds number and temperature of the reflecting surface, implying that the persistence had both a viscous and thermal dependency.

Research into the problem using a specifically designed bifurcated shock tube to synchronously symmetrically reflect a pair of incident shock waves off each other by Filipe Barbosa (Barbosa & Skews, 2002) showed no persistence of regular reflection, and thus indicated that persistence was due to thermal and viscous effects. The current research is a continuation and extension of that work.

2. Objectives

The objectives of this research are to expand on the findings of (Barbosa & Skews, 2002) as to the cause of the persistence of regular reflection and to expand the range of experimental data for the transition that are free from viscous and heat transfer effects. Hence the objectives of this research are:

1. To determine the transition from regular to Mach reflection in the absence of viscous and thermal effects using the bifurcated shock tube at two new wedge angles.
2. If possible to determine the correct mechanism for the transition from regular to Mach reflection.

3. Literature review

3.1. Shock waves

3.1.1. Normal shock waves

A shock wave results from a sudden release of energy. It is a wave front that propagates from a sufficient source of energy at speeds greater than the signal speed of the medium through which it travels. For air the signal speed of the medium is the speed of sound, which is approximately 343 m/s at 20°C.

A shock wave brings about a discontinuous pressure, density and temperature change in the medium as a result of its passage. It also induces velocity in the fluid it has traversed. It is the means by which disparate energy states are brought into equilibrium.

A shock waves' strength is characterised by its Mach number, M, which is a non-dimensional relationship between its speed, v, and the sound speed of the medium, a.

Equation 3.1

$$\mathrm{M} = \frac{\mathrm{v}}{\mathrm{a}}$$

For an ideal gas the local speed of sound is given by Equation 3.2.

Equation 3.2

$$\mathrm{a} = \sqrt{\gamma \mathrm{RT}}$$

γ is the ratio of specific heats for the medium which is 1.4 for air. R is the specific gas constant of 287.06 for air. T is the temperature in Kelvin.

A shock wave propagating from its source forms a surface perpendicular to its direction of travel. If unconstrained it would form a sphere about its source. When generated in a duct it forms a plane surface normal to the sides of the duct. The position of the shock wave then separates duct into two regions; the portion that lies in front of the shock wave and is at its original equilibrium state [1] and the region that the shock wave has travelled over [2], with altered temperature, pressure and entropy.

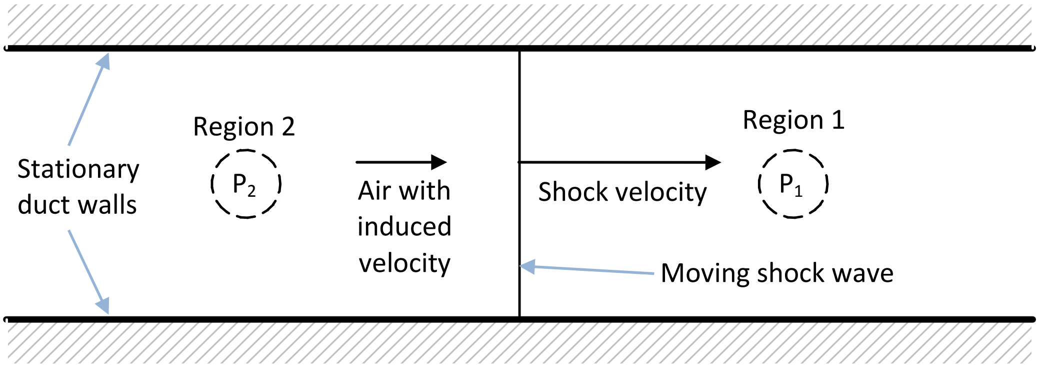

Figure 3.1 Shock wave travelling through a duct

By performing a velocity transformation to bring the shock wave to rest the following figure is obtained which is useful to develop relationships between the various flow regions. From this perspective the shock wave is stationary from the observer's point of view with both the air and, importantly for this investigation, the walls of the duct are moving relative to it.

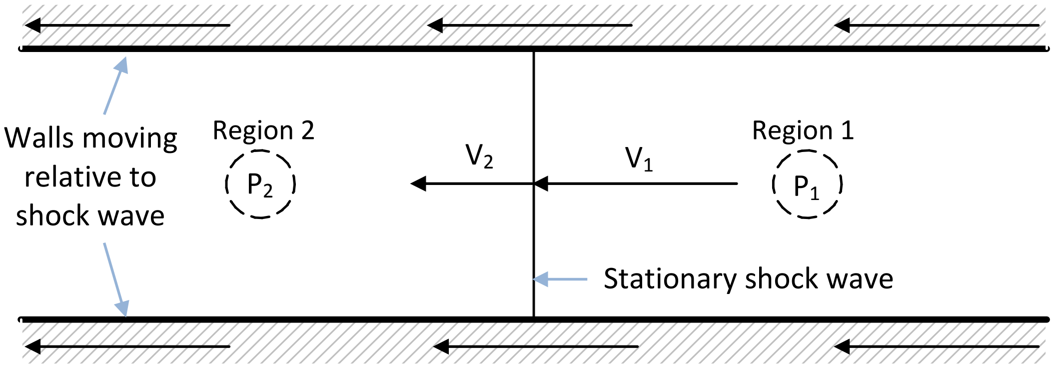

Figure 3.2 Flow relative to a stationary shock wave

If the following assumptions are made, a theory governing the properties in the various regions of a shock wave reflection process can be developed:

- The normal shock wave is travelling in a frictionless duct.
- The duct has a constant cross-sectional area.
- The shock wave is perpendicular to the stream-lines of the flow.
- The flow process is adiabatic.
- Body forces are negligible.
- The gas behaves as an ideal gas.
- The gas has a constant specific heat.

By applying conservation of mass, energy and momentum across the shock wave the following relationship between the pressure in the air before and after the shock is found (Zucrow & Hoffman, 1976).

Equation 3.3

$$\frac{p_2}{p_1} = \frac{2\gamma}{\gamma + 1} {M_1}^2 - \frac{\gamma - 1}{\gamma + 1}$$

In addition for the stationary shock wave the relationship between the Mach numbers of the flow entering and leaving the two regions, denoted subscripts 1 and 2 respectively, is given by the following expression.

Equation 3.4

$$\mathrm{M}_2 = \left(\frac{\mathrm{M}_1^2 + \frac{2}{\gamma - 1}}{\frac{2\gamma}{\gamma - 1}\mathrm{M}_1^2 - 1} \right)^{\frac{1}{2}}$$

3.1.2. Oblique shock waves

An oblique shock wave is a planar shock wave where the streamlines of the flow intersect the plane of the shock wave at an oblique angle i.e. the shock wave is inclined with respect to the streamlines of the flow entering it.

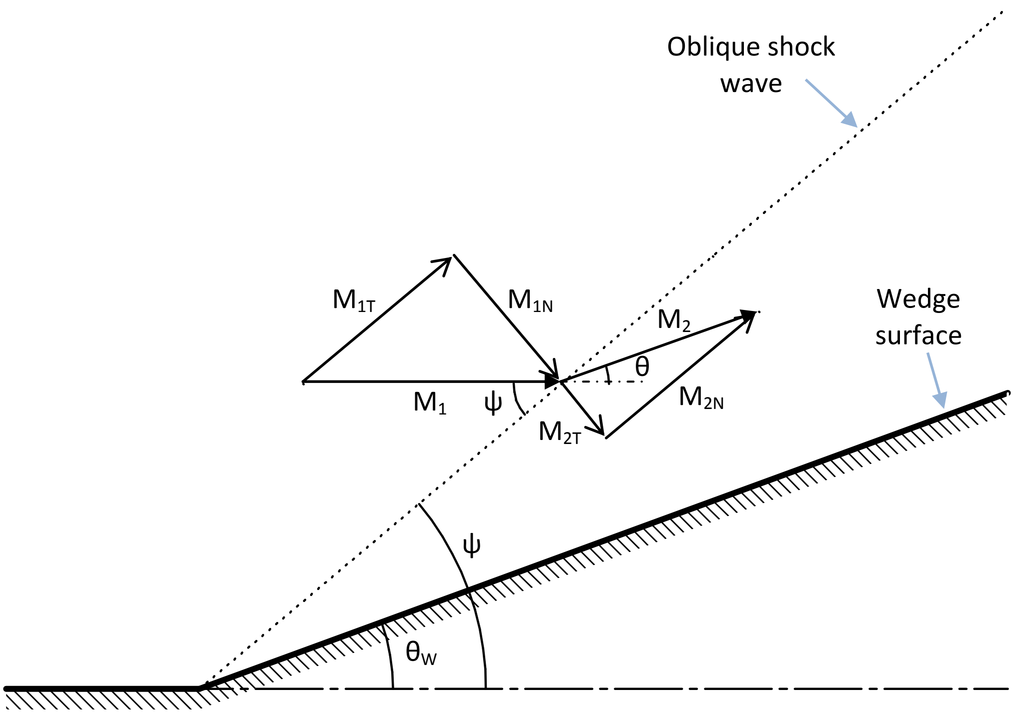

Figure 3.3 Oblique shock wave reflection nomenclature

Oblique shock waves only affect the component of the flow that is perpendicular to the shock wave. In Figure 3.3 the subscripts 1 and 2 refer to the flow properties before and after the shock wave and the letters T and N refer to the tangential and normal components of the flow. In this manner the oblique shock wave causes the flow leaving the shock to subtend a vector angle that is more acute than that of the flow entering the shock i.e. θ is smaller than ψ.

From the geometry in the above figure and Equation 3.4 the pressure ratio across the shock wave is given by the following (Zucrow & Hoffman, 1976).

Equation 3.5

$$\frac{p_2}{p_1} = \frac{2\gamma}{\gamma+1} M_1^2 \sin^2\phi - \frac{\gamma-1}{\gamma+1}$$

The flow deflection angle, θ, as a function of the Mach number and the inflow angle ϕ is given by:

Equation 3.6

$$\tan\theta = \frac{M_1^2\sin^2\varphi - 1}{\tan\varphi\left[(\gamma+1)\frac{M_1^2}{2} - M_1^2\sin^2\varphi + 1\right]}$$

The change in Mach number across the oblique shock wave is a modification of Equation 3.4 incorporating the effects of an oblique shock:

Equation 3.7

$$M_2 = \frac{1}{\sin(\phi-\theta)}\sqrt{\frac{(\gamma-1)M_1^2\sin^2\phi + 2}{2\gamma M_1^2\sin^2\phi - (\gamma-1)}}$$

For an oblique shock wave turning a flow there are two important values for the angle which the shock wave makes with respect to the streamlines. The first is the angle at which the flow leaving the shock attains Mach one, called the sonic angle, ϕs, (Zucrow & Hoffman, 1976) which is calculated from the following expression.

Equation 3.8

$$\sin\varphi_s = \frac{1}{\gamma M_1^2}\left\{\frac{\gamma+1}{4}M_1^2 - \frac{3-\gamma}{4} + \left[(\gamma+1)\left(\frac{9+\gamma}{16} - \frac{3-\gamma}{8}M_1^2 + \frac{\gamma+1}{16}M_1^4\right)\right]^{\frac{1}{2}}\right\}$$

The other important angle is the maximum inflow angle of an oblique shock wave and is given by ϕm. This is the theoretical maximum inflow angle into an oblique shock where the shock wave remains attached to the leading edge of the wedge (Zucrow & Hoffman, 1976).

Equation 3.9

$$\sin\phi_m = \frac{1}{\gamma M_1^2}\left\{\frac{\gamma+1}{4}M_1^2 - 1 + \left[(\gamma+1)\left(1-\frac{\gamma-1}{2}M_1^2+\frac{\gamma+1}{16}M_1^4\right)\right]^{\frac{1}{2}}\right\}$$

3.2.Shock wave reflection

3.2.1. Regular and Mach reflection

If a planar shock wave encounters a wedge inclined to its direction of motion it can reflect off it in a number of different ways, each of which is characterised by geometrical features of the reflection. The various types of reflection that have been observed have domains that have been defined depending on the incident angle of the wedge with respect to the shock wave path, θ_W, and the strength of the incident shock wave, M_s, described in detail in the *Handbook of Shock Waves* (Ben-Dor, 2007). The regions of interest are summarised in Figure 3.4.

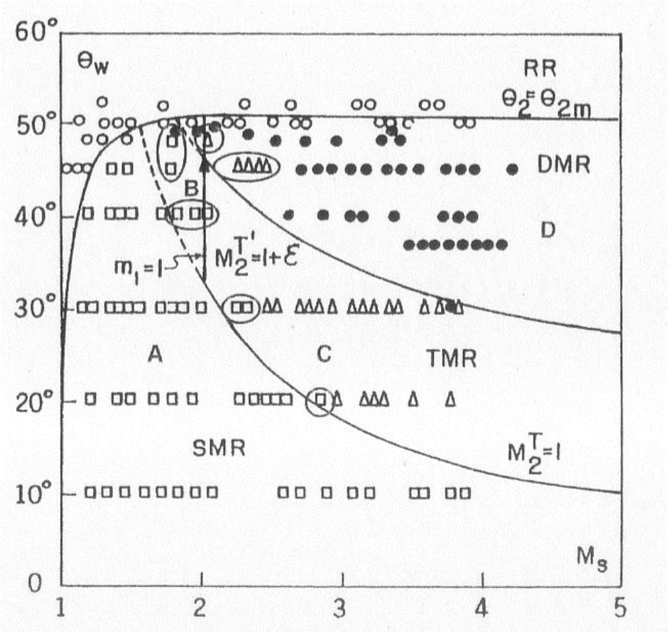

Figure 3.4 Reflection domains in terms of Mach number and wedge angle (Ben-Dor, 2007)

The present study aims to investigate the transition from regular reflection (RR) to single Mach reflection (SMR). SMR will be referred to as Mach reflection (MR) from this point for simplicity's sake as both double-Mach-reflection (DMR) and triple-Mach-reflection (TMR) are outside the domain of the present study. The domain of transition from RR to MR implies wedge angles of less than 50° and Mach numbers of less than two.

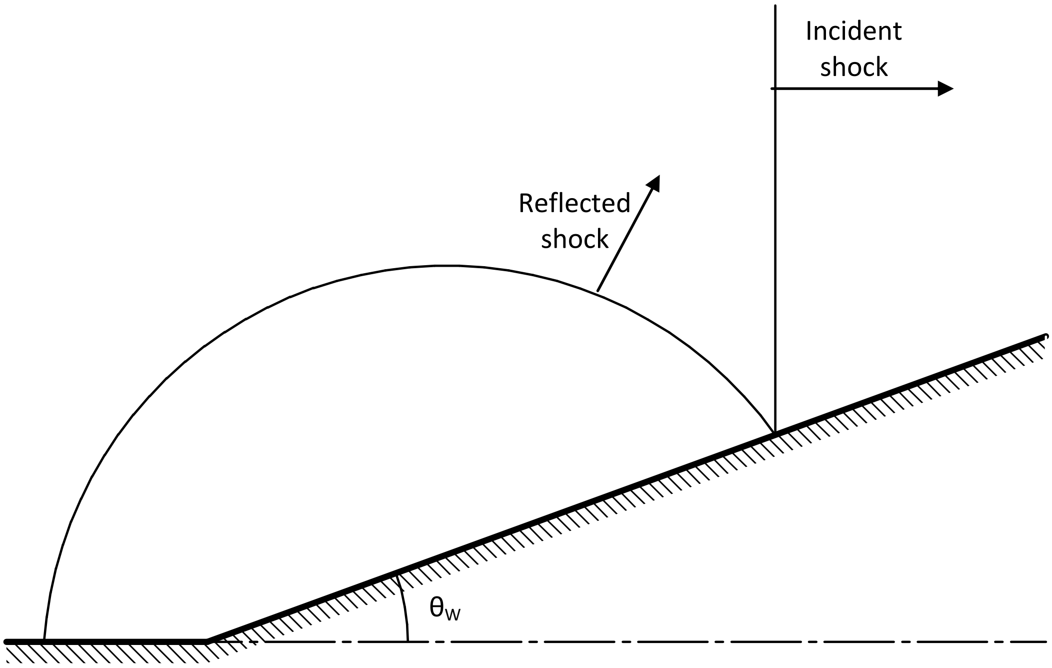

Figure 3.5 Regular reflection

RR is characterised by an incident and a reflected shock wave that meet at the reflection point on the surface of the wedge.

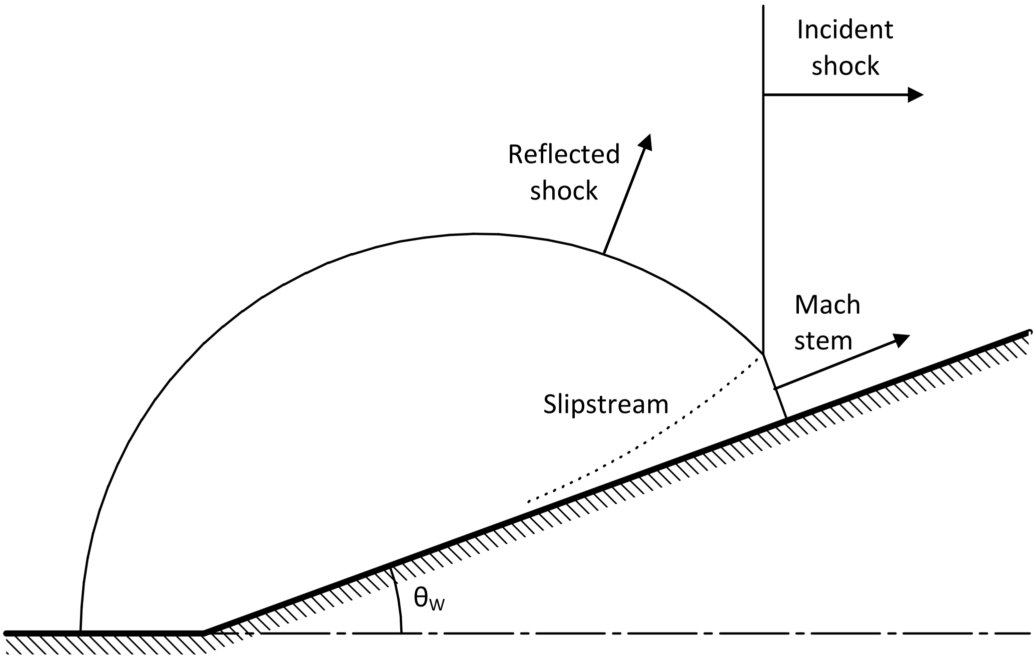

Figure 3.6 Mach reflection

MR has three shock waves, in addition to the incident and reflected waves it has a Mach stem which grows perpendicularly to the surface of the wedge. All three shock waves meet at the triple point. MR occurs in a different flow regime to RR which can be described in two ways: MR either occurs at a smaller wedge angle for a given Mach number than RR, or alternatively and equivalently, for a fixed wedge angle MR occurs at a greater Mach number than RR. These two explanations parody the primary methods used to investigate the transition from RR to MR, namely varying the wedge angle at a fixed Mach number and varying the Mach number for a fixed wedge angle.

As the Mach reflection geometry moves along the wedge air that has been passed over by the incident and reflected shock waves has a different thermodynamic history to the air that has been passed over by the Mach stem. The two regions of air have equal pressure are separated by a contact discontinuity called a slipstream.

3.2.2. Two-shock theory

The notation is based on a pseudo-stationary reference frame attached to the reflection point, where the reflection point has been brought to rest by a velocity transformation and flow velocities are measured with respect to it. This is a valid transformation as the reflection geometry is self-similar as it progresses along the reflecting surface (Bleakney & Taub, 1949).

A pseudo-steady reference frame has the effect of treating a shock wave moving into still air within a shock tube as if it were a stationary, steady shock wave in moving air in a supersonic wind tunnel.

One aspect of a pseudo-steady reference frame that differs significantly from a steady reference frame is that the wall appears to be moving relative to the reflection point of the shock waves at the same speed that the reflection point was progressing along the surface of the wedge prior to the transformation.

The relationships between the flow properties in different regions of RR are described by two shock theory. It is the basis of the theory used to predict the transition from regular to Mach reflection. The notation used is illustrated in Figure 3.7.

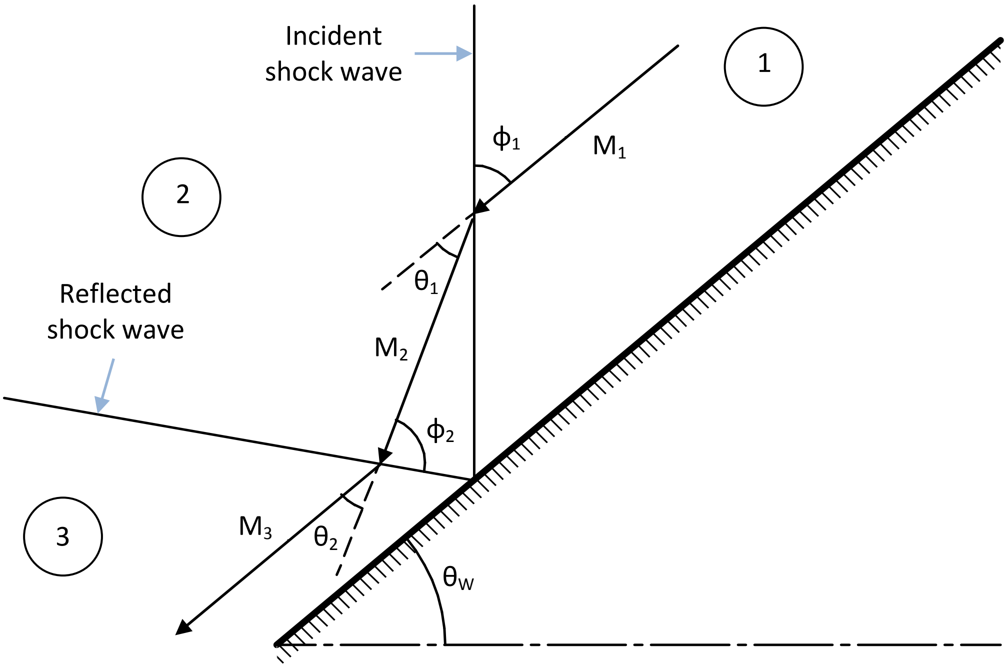

Figure 3.7 Notation for two shock theory

The basic equations of two shock theory were formulated by John von Neumann (von Neuman, 1943) and the equations assume that the fluid is inviscid and that the shock waves are planar close to the reflection point.

The incident shock wave divides the fluid in region 1 which has not passed through the shock from the fluid in region 2 which has. The fluid in region 3 has passed through both the incident and reflected shock waves. Equation 3.5, Equation 3.6 and Equation 3.7 applied across both the incident and reflected shock waves relate the pressure ratio, the flow deflection angle and the Mach number in these three regions, typically based on information of the flow prior to the incident wave in region one, typically ambient values, yielding six equations.

A fixed geometric relationship exists between the inflow angle to the incident shock wave, ϕ_1, and the wedge angle, θ_w:

Equation 3.10

$$\varphi_1 = 90 - \theta_w$$

The relationship between the moving planar shock wave, with its shock-strength Mach number denoted by M_s, and the incident shock wave in the pseudo-stationary reference frame of the theory is related by the speed at which the reflection point moves up the wedge, which is the same as the flow velocity into the incident shock wave.

Equation 3.11

$$M_1 = \frac{M_s}{\sin\phi_1}$$

The last geometric relationship evident from Figure 3.7 is that the flow deflection angles from the incident and reflected shock waves need to be equal for the flow to be turned back parallel to the wedge, to ensure a physically realistic model of the flow. A relaxation of this assumption may be the cause of the inconsistency between experimental observations and the predicted transition behaviour.

Equation 3.12

$$\theta_1 = \theta_2$$

These equations form a closed set that allow the properties of regular reflection to be calculated from the initial pressure in region 1, the wall angle, θw, and the incident shock wave Mach number, Ms.

3.2.3. Transition criteria

The mechanisms by which the transition from regular to Mach reflection occurs were postulated by von Neumann in 1943 (von Neuman, 1943). He postulated and provided the mechanisms for two criteria for the transition, namely the sonic and detachment angles. von Neumann also suggested the mechanical equilibrium criterion which was investigated by (Henderson & Lozzi, 1975). The mechanical equilibrium criterion has no solution for weak shock waves ($Ms < 1.5$), according to (Barbosa & Skews, 2002), which is the domain of transition for the wedge angles investigated in this study and as a result will be neglected.

According to the detachment criterion, transition from regular to Mach reflection occurs when the limiting inflow angle given by Equation 3.9, ϕ_m, is reached for the reflected shock wave. A physical interpretation of this is the angle at which the reflected shock can no longer turn the flow back parallel to the wedge, resulting in a physical impossibility of flow into the wedge surface.

The transition Mach number for a particular wedge angle can be solved for iteratively by withholding the incident Mach number and adding the following relationship to two shock theory.

Equation 3.13

$$\phi_2 = \phi_m$$

The postulation of the sonic criterion proposes that the transition from regular to Mach reflection occurs when the flow leaving the reflected shock wave achieves the sonic speed, the rationale is that this is the minimum speed at which information from the corner can propagate to the reflection point, communicating the physical information required for a transition from RR to MR.

The transition values of the sonic criterion are solved for by withholding the incident Mach number and adding the following equation:

Equation 3.14

$$\phi_2 = \phi_s$$

The values of transition from regular to Mach reflection given by the sonic and detachment criteria are illustrated below. This image is similar to Figure 3.4, with only the regions of interest to this study shown.

As can be seen in Figure 3.8, the sonic and detachment criteria give similar values for the transition from RR to MR, with the sonic criterion suggesting transition at a slightly lower Mach number for a given wedge angle. The most notable difference given by the two criteria in terms of the transition values with respect to Mach number is where the two theories asymptote to infinite Mach number for transition, at a wedge angle of approximately 50°.

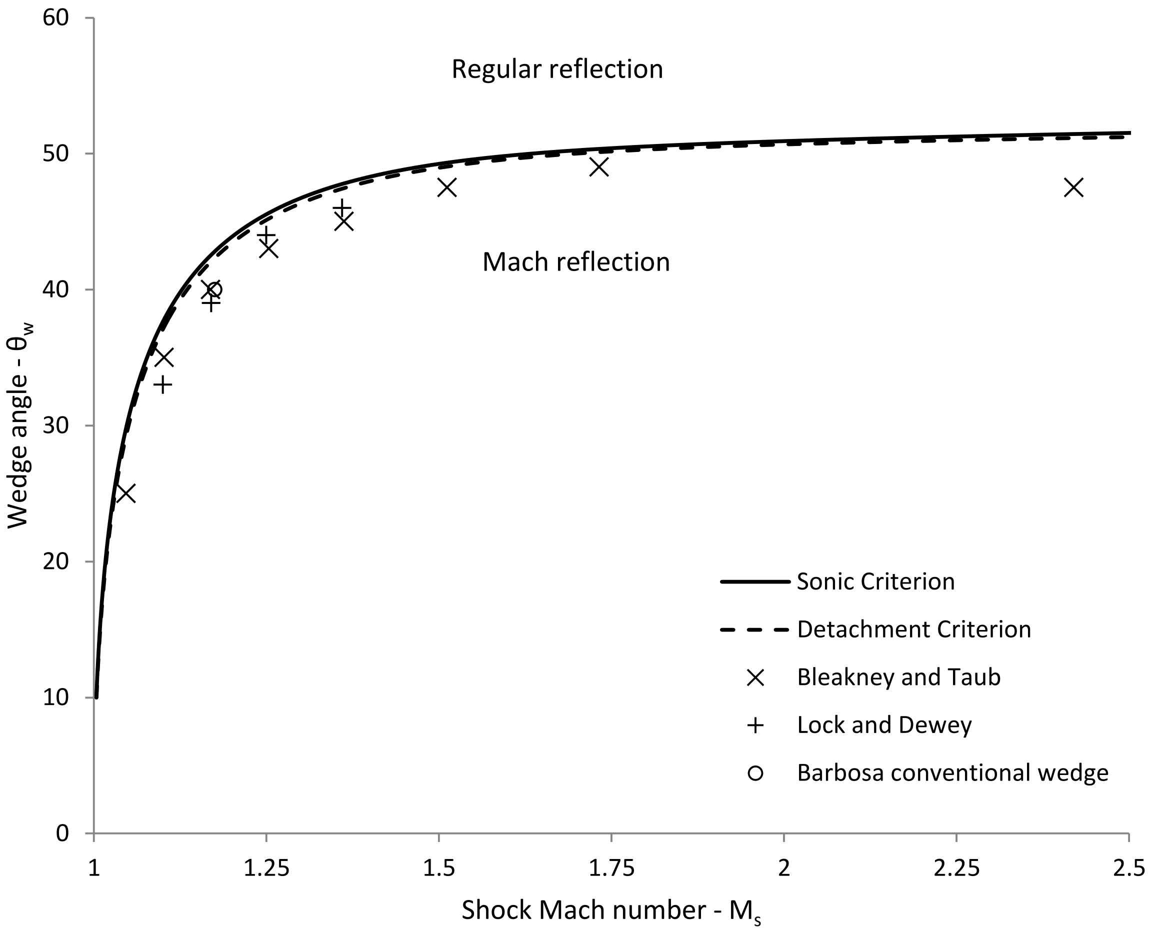

Figure 3.8 Experimental vs. theoretical transition values

In addition to the theory lines, the locations of transition that were experimentally obtained are plotted on the above figure. The findings of (Bleakney & Taub, 1949) and (Lock & Dewey, 1989) are included with the addition of the findings of a conventional wedge investigation carried out by (Barbosa & Skews, 2002). In attempts to experimentally determine the transition point, and hence confirm the mechanism that brings about the transition, persistence of regular reflection into the Mach reflection domain has been observed. The mechanism of the detachment criterion infers that regular reflection should not be possible in the domain of Mach reflection.

3.3. Persistence of regular reflection

3.3.1. Initial discovery of discrepancy

Experimental validation of the transition criteria has proved difficult. In 1945 an investigation of shock wave reflection in air was carried out by L.G Smith (1) over a range of wedge angles and Mach numbers. He observed that regular reflection was occurring for combinations of Mach number and wedge angle that are in the domain of Mach reflection.

In 1976, (Bleakney & Taub, 1949) published the results of their re-measurement of L.G. Smith’s images (L. G. Smith, 1945), plotted in Figure 3.8, in addition to reporting on their own experiments. They measured the angle the triple point subtended with respect to the tip of the wedge, as illustrated in Figure 3.9. They then extrapolated their results in terms of Mach number to zero triple point trajectory angle, χ, to determine the transition Mach number.

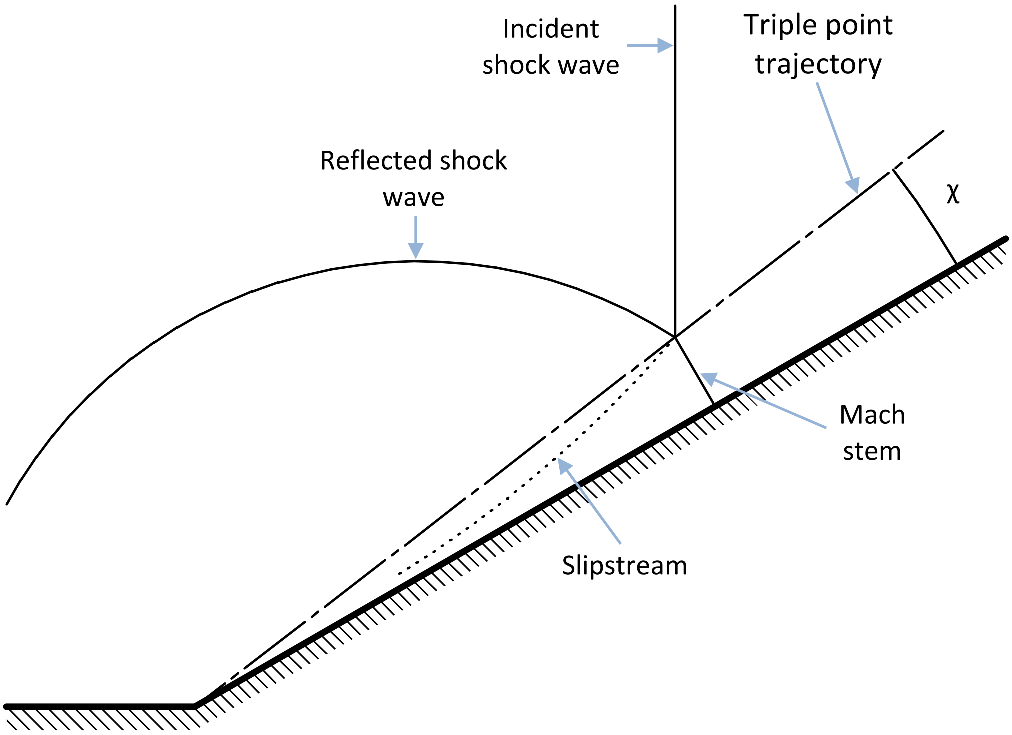

Figure 3.9 The triple point trajectory angle, χ, subtended by the Mach stem

(Bleakney & Taub, 1949) confirmed the findings of (L. G. Smith, 1945) and observed the persistence of regular reflection into the Mach reflection domain.

3.3.2. Viscous dependency

(Hornung, Oertel, & Sandeman, 1979) concluded in their 1979 report that the amount of persistence in the findings of (Takayama & Sekiguchi, 1977) changed with Reynolds number, implying that the persistence of regular reflection has a viscous dependency. They explained how the persistence of regular reflection could be due to the boundary layer immediately behind the shock by providing a mechanism whereby the boundary layer could relax the assumptions of the two shock theory that the transition calculation is based upon.

(Hornung, Oertel, & Sandeman, 1979) explained how the presence of a boundary layer could cause the persistence of regular reflection beyond the constraint of the detachment criterion i.e. that the reflected shock wave could apparently turn the flow in excess of the maximum deflection angle. The presence of the boundary layer relaxes the angle through which the flow is turned by the reflected shock wave and thus delays the limiting turning angle of the detachment criterion from being achieved.

The mechanism which (Hornung, Oertel, & Sandeman, 1979) proposed shows how the boundary layer acts as a mass sink which acts as if to curve the wall away from the reflection point.

In a stationary reference frame the boundary layer grows from zero at the wall to a uniform velocity equal to the gas velocity, Vg, behind the shock wave at a distance normal to the wall equal to the boundary layer thickness, δ. The effect of the boundary layer on an inviscid flow may be modelled by moving the wall boundary to the position indicated by the displacement thickness, δ*.

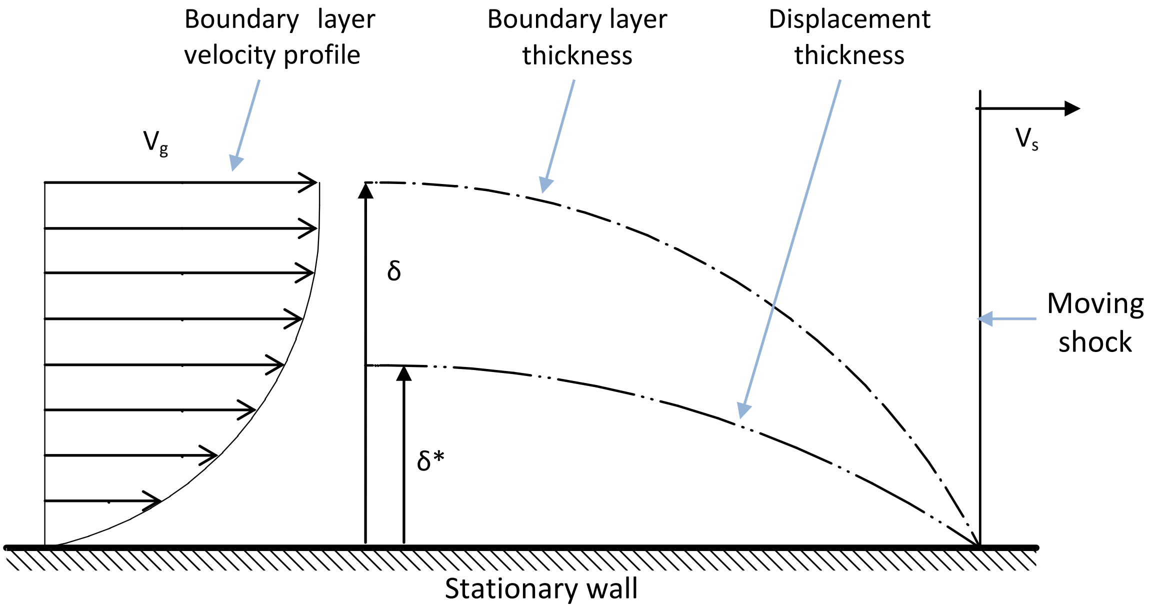

Figure 3.10 Boundary layer with moving shock and stationary wall

In a reference frame attached to the reflection point, the velocity profile of the boundary layer is inverted as the reflection point, and hence the wall appears to be moving more rapidly than the gas.

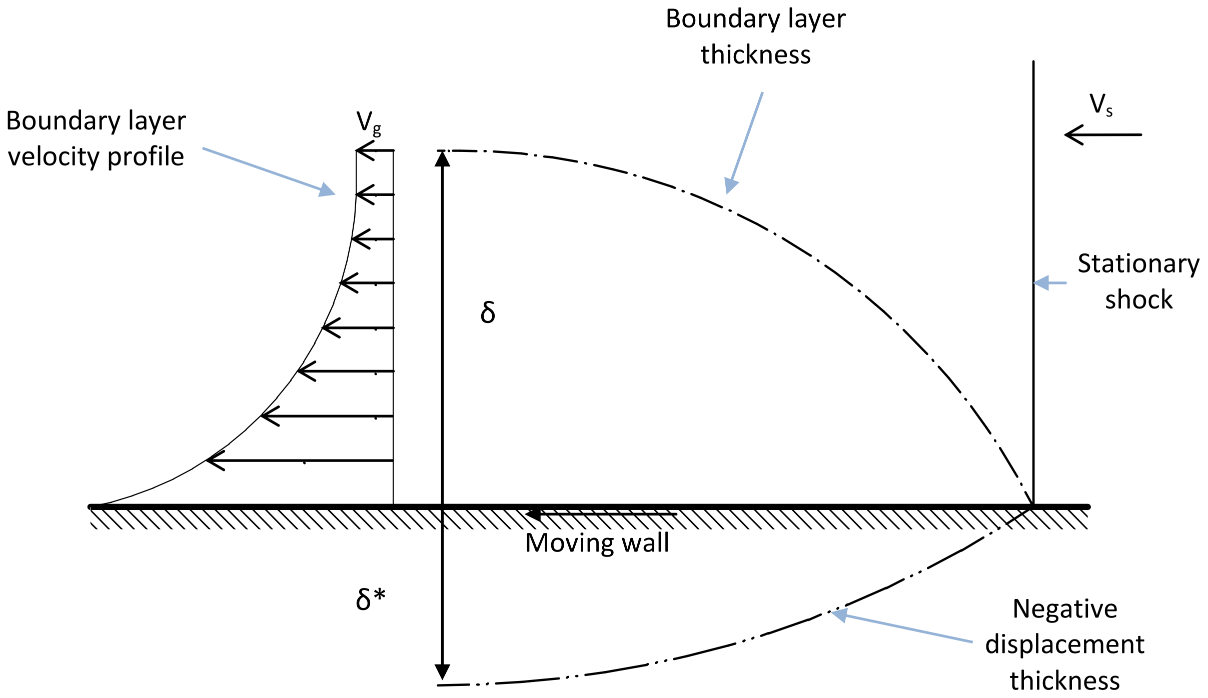

Figure 3.11 Boundary layer with moving wall and stationary shock

The mass sink created by the negative displacement thickness in the inviscid model of the interaction can be illustrated by a displaced wall behind the reflection point in an inviscid flow.

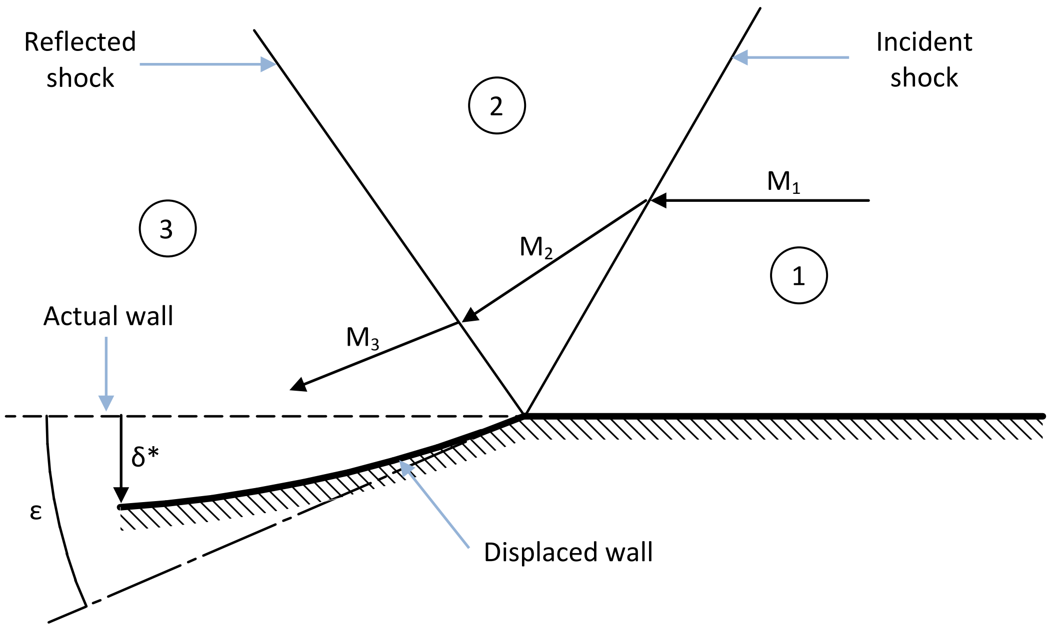

Figure 3.12 The negative displacement effect of the boundary layer

This has the effect of relaxing the angle through which the flow has to be turned back parallel to the wall by the reflected shock wave by ε at the reflection point, implying that regular reflection is possible at a greater range of wedge angles by relaxing the restrictions on the assumptions on which both the sonic and detachment transition criteria are based. This gives rise to the persistence of regular reflection by delaying both the onset of both the sonic and maximum-deflection inflow angles to the reflected shock wave, expressed in Equation 3.8 and Equation 3.9 respectively.

(Hornung, Oertel, & Sandeman, 1979) suggested that the viscous displacement effect could be studied by varying the Reynolds number. A study was undertaken by (Hornung & Taylor, 1982) on strong shock wave reflections at Ms = 5.5 in Argon. They carried out a number of transition experiments by varying the wedge angle and extrapolating the dimensionless Mach stem height (found by dividing the Mach stem height by its' base's distance to the tip of the wedge, an analogue of the Mach stem angle) to zero, for four different Reynolds numbers. Their results were then extrapolated to infinite Reynolds number to determine the transition under inviscid conditions. They concluded that the transition occurred at the theoretical sonic value and that the persistence of regular reflection is due to viscous effects. The viscous dependence of the persistence of regular reflection was confirmed by the experiments of (Wheeler, 1986).

(Lock & Dewey, 1989) observed that transition occurred when the signal speed of the flow behind the reflected shock was equal to that of the reflection point in support of the sonic transition criterion's mechanism. However, the transition point they found did not coincide with either the sonic or detachment criteria and indicated a persistence of regular reflection.

3.3.3. Thermal dependency

(Barbosa & Skews, 2002) explained how the extrapolation to infinite Reynolds number carried out by Hornung and Taylor (2) did not account for thermal effects, which had been shown to affect the persistence of regular reflection.

In a study in 1994, (van Netten, Dewey, & von Haimberger, 1994) observed that the reflection was affected by the temperature of the reflecting surface. von Netten et.al. derived this result by reflecting shocks over wedges that had been heated and cooled with respect to the ambient conditions and observing varying degrees of persistence depending on the temperature of the wedge surface.

This effect can be explained by the temperature difference between the hot gas behind the shock wave and the cold wall of the test section. The heated post-shock gas immediately adjacent to the relatively cool reflecting surface has an increased density due to its lower temperature. This dense gas acts as a mass-sink causing the thermal boundary layer to relax the conditions of the transition criteria in a manner similar to that of the viscous boundary layer. The opposite effect can be achieved by heating the reflecting surface.

Both the viscous and thermal causes of the persistence of regular reflection were confirmed by the detailed numerical experiments of (Henderson, Crutchfield, & Virgona, 1997). Their findings await experimental confirmation.

The findings of the various researchers have indicated that the persistence of regular reflection is due to both heat transfer and viscous interaction of the reflection with the reflecting surface, in contradiction to the assumptions of two shock theory and hence the transition criteria.

3.3.4. Internal cavity experiments

One method of investigating shock wave reflection that excludes the effects of thermal and viscous interaction is the internal cavity experiment, initially conducted by (W. R. Smith, 1959).

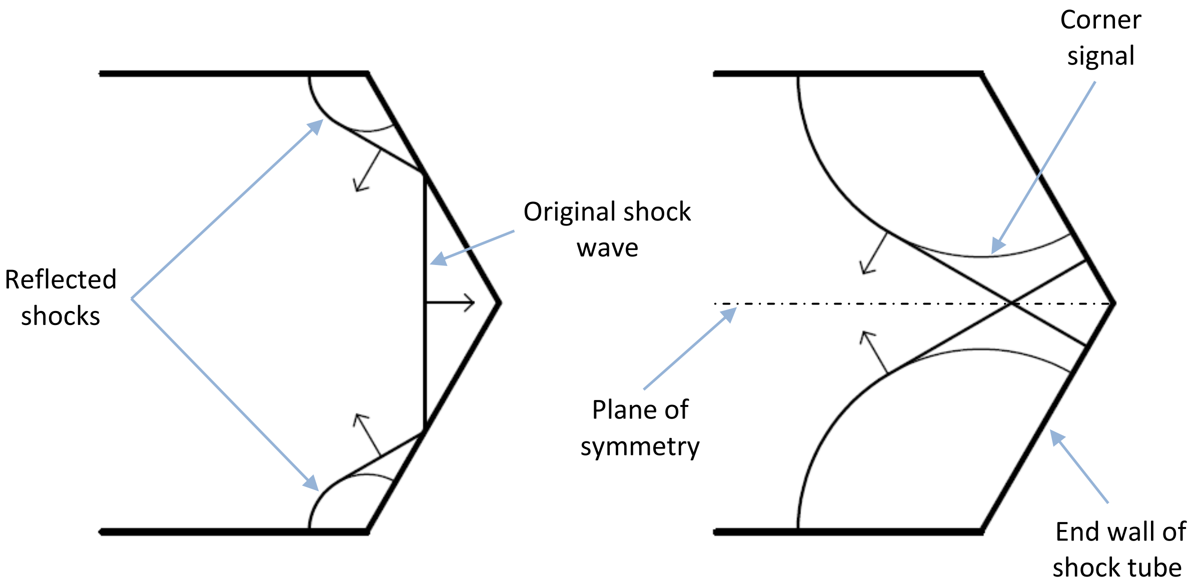

Figure 3.13 Internal cavity reflection process

An internal cavity experiment utilises a v-shaped end wall of a shock tube to reflect a single incident shock wave as a pair of inclined shocks that then reflect off each other. The plane of symmetry of their reflection forms an ideal adiabatic inviscid reflecting surface of infinite stiffness. The plane of symmetry simulates a reflecting surface inclined to the reflected shock waves' paths which is analogous to a wedge inclined to the path of a planar shock wave.

(W. R. Smith, 1959) found that he did not observe the persistence of RR within his experimental accuracy but attributed his findings to the more precise optical measurements rather than the properties of the reflecting surface. At transition in a typical shock wave reflection investigation off a physical wedge both the Mach stem and the slipstream are close to the wall and are difficult to resolve from it.

(Barbosa & Skews, 2002) explained that there are systematic flaws with the internal cavity experiments of (W. R. Smith, 1959) and later experiments of the same type reported by (Henderson & Lozzi, 1975). These flaws include difficulties measuring the strength of the shock waves that reflect off the end walls and the small distances available to take measurements before the reflection is overtaken by corner signals. The data derived from these experiments are subject to large errors as a result, and the uncertainty has an amplified effect on the extrapolation to determine the transition values.

(Skews, 1995) suggested in 1995 that the symmetrical reflection of a pair of separate equal strength shock waves meeting at the trailing edge of a wedge, illustrated in Figure 3.14, would cause their plane of symmetry to act as an ideal inviscid reflecting surface. Each half of the reflection, about the plane of symmetry, is analogous to a shock wave reflecting off a wedge inclined to its path described by two shock theory, with the analogue-wedge having an angle of half of the wedge in the apparatus due to the symmetry of the interaction.

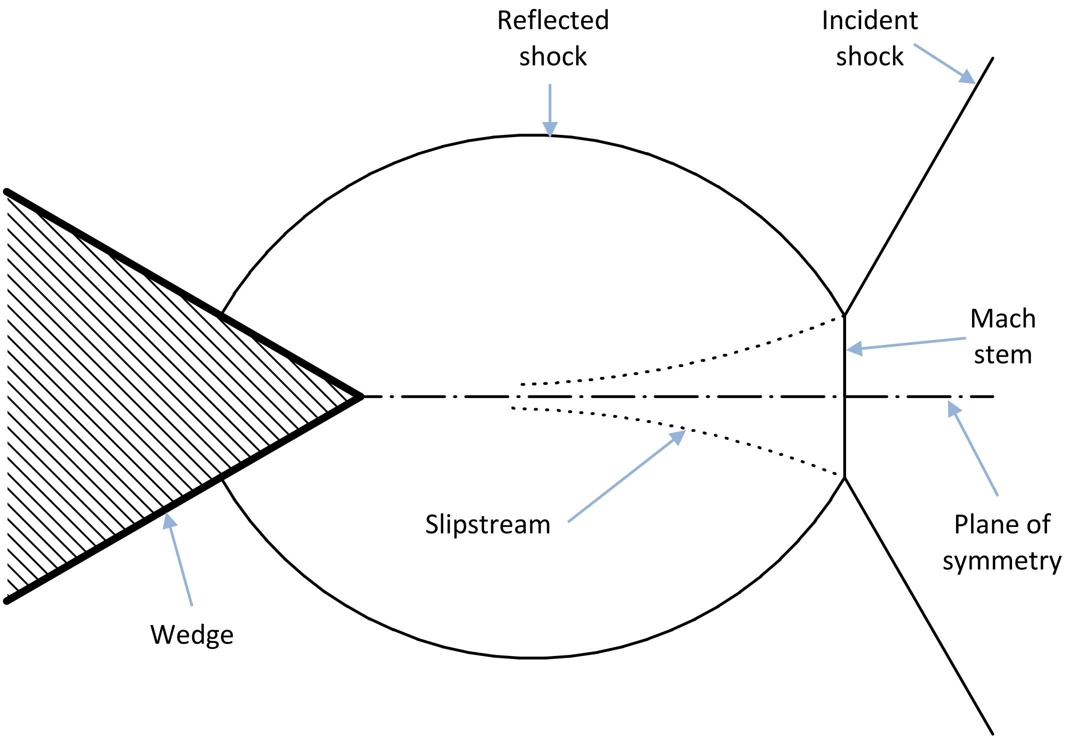

Figure 3.14 Mutual reflection at the trailing edge of a wedge

(Skews, 1995) found that the only suitable method of generating the required shock wave geometry with sufficiently-synchronised shock waves was in a bifurcated shock tube. In a bifurcated shock tube, a single shock wave generated by a driver is split into two waves. The waves are then guided from their diverging course through symmetrically curved tube sections to converge at the trailing edge of a wedge in the test section. One feature of a bifurcated shock tube is that the entire section downstream from the splitter has to be changed for each angle that is investigated.

Following on from the work of Skews a larger facility was commissioned and an investigation was undertaken by F.J. Barbosa whose findings were reported in (Barbosa & Skews, 2002).

The bifurcated shock tube and the diaphragm-less piston-actuated shock tube driver were designed and manufactured by Barbosa to conduct research on persistence of regular reflection. During his investigation another use for the bifurcated apparatus became apparent - the interaction of shock waves with vortices. This interaction is a result of what is often an undesirable side-effect in a bifurcated shock tube, as far as investigations into the persistence of regular reflection are concerned. This is the instance where the shock waves from each leg of the bifurcated section arrive at the test section with a distinct time interval between them. The shock wave from the first leg generates a vortex on the corner formed by the apex of the wedge, the vortex then interacts with the shock wave from the second wave. As a result of this discovered use Barbosa investigated shock wave vortex interactions and investigated the persistence of regular reflection on only one of the three angles of bifurcated section that were manufactured for the study.

The remaining two bifurcated sections, 40° and 96°, which correspond to transition investigations on wedges inclined at 20° and 48°, are the subject of the current research.

Barbosa investigated the transition from RR to MR on a bifurcated section of 80° which, due to the symmetry of the interaction, corresponds to a reflecting surface inclined at an angle of 40° to the shock's path. He obtained contact shadowgraph images of the mutual reflection of a pair of equal strength synchronous shock waves at strengths of $1.17 < Ms < 1.35$.

The extrapolation of his data to zero stem angle to determine the transition point indicated a transition from RR to MR at the theoretical value within experimental statistical accuracy. The bifurcated shock tube experiments initially indicated that the transition occurred at $Ms = 1.144$ where the sonic and detachment criteria values were 1.128 and 1.135 respectively.

Barbosa then conducted a multivariate nonlinear regression study of his data to accommodate the mis-synchronisation between the shock waves from each of the legs. He postulated that mis-sychronisation was the dominant cause of uncertainty in his measurements. This had the effect of fitting a three dimensional surface to the data in terms of the incident shock Mach number, Ms, the triple point trajectory angle, χ, and the mis-synchronisation between the incident shock waves, ψ. A planar slice through the three dimensional surface for zero mis-synchronisation, resulted in a quadratic curve fit that had been corrected for mis-synchronisation and was extrapolated to zero stem angle to determine the transition from RR to MR free from the effects of mis-synchronisation.

Barbosa rationalised the undertaking by explaining how the slight mis-synchronisation between the shocks from each of the two legs can affect the measurements.

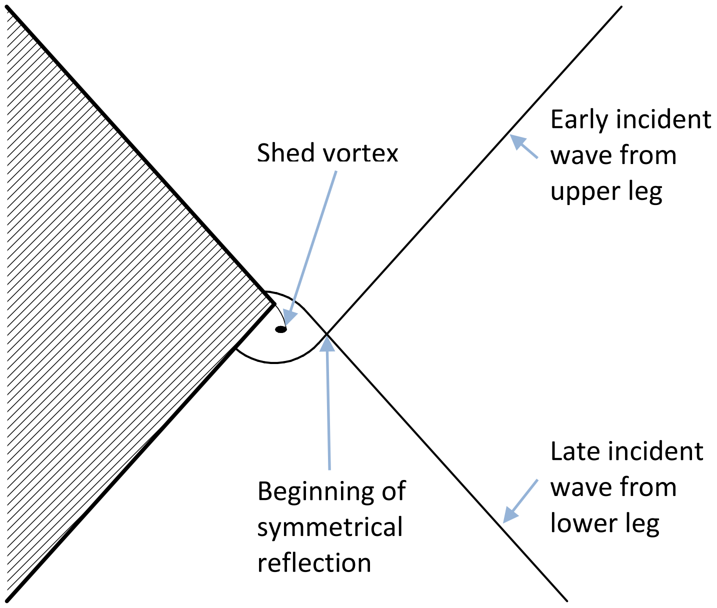

Figure 3.15 Exaggerated interaction of mis-synchronised shock waves (early)

Figure 3.15 illustrates the features of the early interaction of a pair of mis-synchronised shock waves (Barbosa & Skews, 2002). The early shock wave creates a vortex as it rounds the corner of the wedge, and the second wave passes over the vortex, interacting with it. As a result the symmetrical interaction of the shock waves is delayed, forming the interaction illustrated in the figure below.

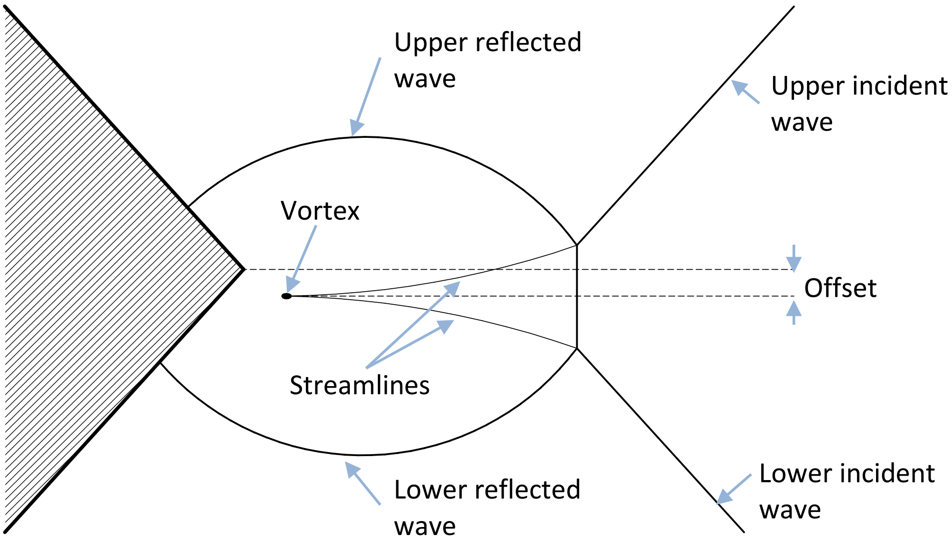

Figure 3.16 Exaggerated interaction of mis-synchronised shock waves (late)

The delayed onset of the interaction has the effect of reducing the length over which the Mach stem has to form, in addition to creating a parallax effect when the angle is measured with respect to the apex of the wedge. Both of these effects cause systematic errors in the measurement of the angle. Handily the error is proportional to the mis-synchronisation and the multivariate analysis can accommodate it.

The result of the multivariate analysis was a transition Mach number of 1.135, which is exactly the same as the theoretical Mach number determined from the detachment criterion for the reflection surface inclined at 40°. As the result was free from transport effects from the surface (due to the symmetrical equal strength reflection) the hypothesis of (Hornung, Oertel, & Sandeman, 1979) was confirmed.

4. Experimental facilities

4.1.The shock tube

4.1.1. Overview of a bifurcated shock tube

The apparatus used to investigate the cause of the persistence of regular reflection is the bifurcated shock tube. The functional components are illustrated below:

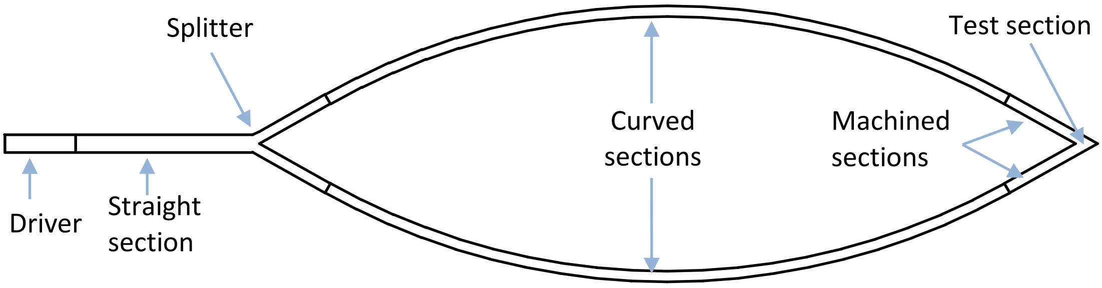

Figure 4.1 Bifurcated shock tube layout

The driver is used to generate a planar shock wave in the shock tube. In this investigation shock waves were generated using two different drivers on the bifurcated apparatus. The two drivers, hereafter the ‘piston-actuated’ driver and the ‘simple’ driver, were required as they operated in different Mach strength regions, which are the domains of transition for the different wedge angles investigated.

After the shock wave is generated it travels down a long straight section before it is divided in the bifurcated section. This section allows the effects of the launch process to smooth out and the shock wave to form a uniform planar wave.

The splitter, as the name suggests, divides the wave generated by the driver into a pair of synchronous, equal-strength shock waves and guides the waves into the two legs that make up the bifurcated section of the shock tube. The splitter is manufactured from CNC (Computer Numerically Controlled) machined sections of steel bolted together.

The curved pipes form the middle piece of the bifurcated portion of the apparatus. The pipe is structural tubing that has been rolled to the required radius for the angle being investigated. The radius is such that, in the length available between the straight lengths leaving the splitter and the straight sections prior to the test section, the curved section guides the normal waves leaving the splitter from their diverging course onto a converging course so that the waves meet in the test section. The curvature is as gentle as possible in the space available to ensure that the shocks maintain their planar structure. The last 800mm in each leg of the bifurcated section are a pair of straight CNC milled sections to smooth the shock waves before the arrive in the test section. Located within each of the machined sections is a pair of tappings for pressure transducers to measure the strength and speed of the shock waves in each leg of the shock tube. These transducers also allow the measurement of the synchronisation between the waves in the different legs of the apparatus.

The test section forms the angled wedge at the apex of the bifurcated section. The test section is made up of CNC machined halves that are bolted together. The test section has a pair of 200mm diameter windows that allow the interaction of the shock waves to be visualised at the trailing edge of the wedge.

4.1.2. The bifurcated shock tube at Wits

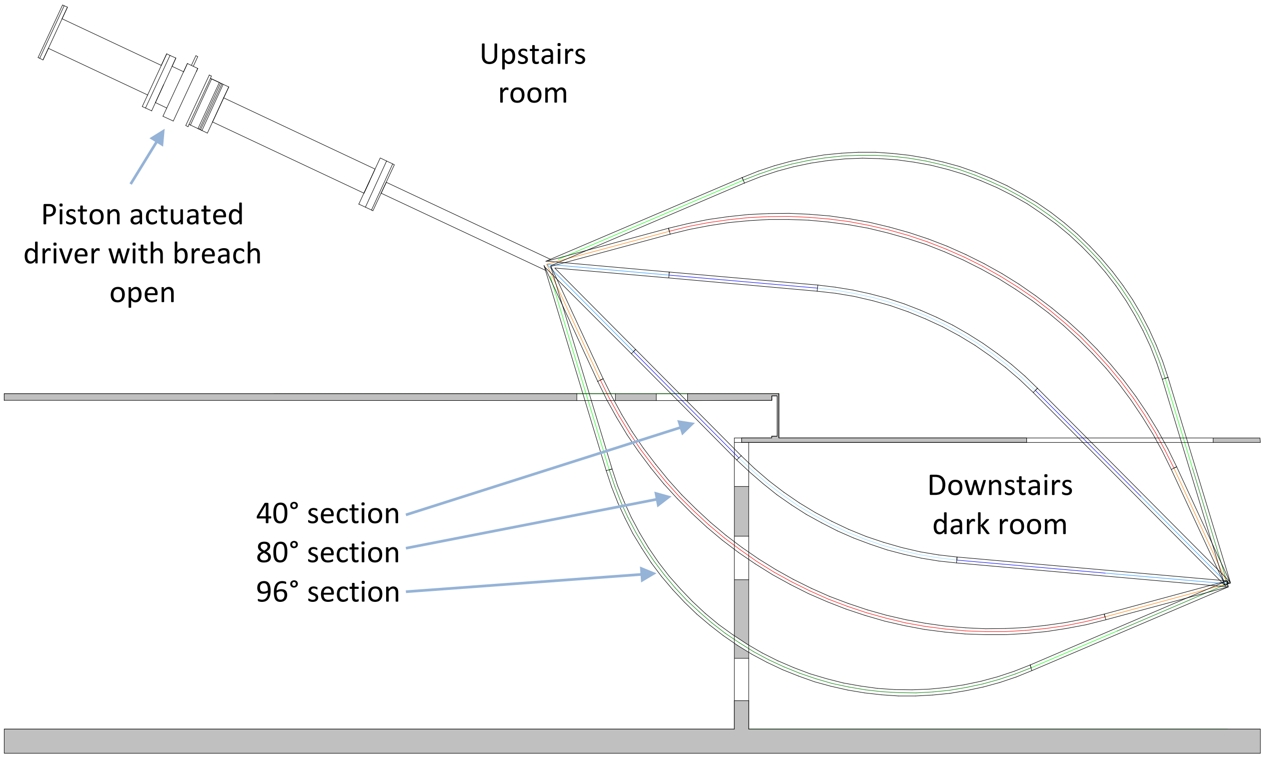

Figure 4.2 Schematic layout of Bifurcated facility at Wits

The above illustration shows the three different bifurcated sections that were investigated in the North West Engineering Laboratory. The facility is nearly 11m long from the back of the piston actuated driver to the end of the test section.

All of the bifurcated sections have an equal length from the splitter to the test section. This is to ensure that the test section is placed at a convenient height for the shadowgraph optics and leaves sufficient space for the widest angle's curved section to clear the floor.

The apparatus spans three rooms, with the bottom right room in the figure sealed from light to enable the camera to be operated with its shutter held open waiting for the flash from the light source in response to the presence of a shock wave in the apparatus.

As the apparatus spans three rooms it has to pass through both walls and floors. Some holes in the floor and walls existed for the apparatus prior to this investigation, however some were modified to accommodate the new sections being assembled as necessary. This modification involved cutting through the steel grid that supports the upstairs floor with an angle grinder, in addition to enlarging the holes in the wall with a large hammer. The hole in the roof was enlarged with a wood saw and a steel frame was fitted to it that supported loosely-fitted planks that allowed the hole to be covered in all the regions that were not currently occupied by the apparatus.

4.1.3. The bifurcated section

The bifurcated section of the shock tube has a source of error peculiar to its arrangement in the North West Engineering Laboratory. The upper and lower legs of the shock tube run in different rooms in the laboratory.

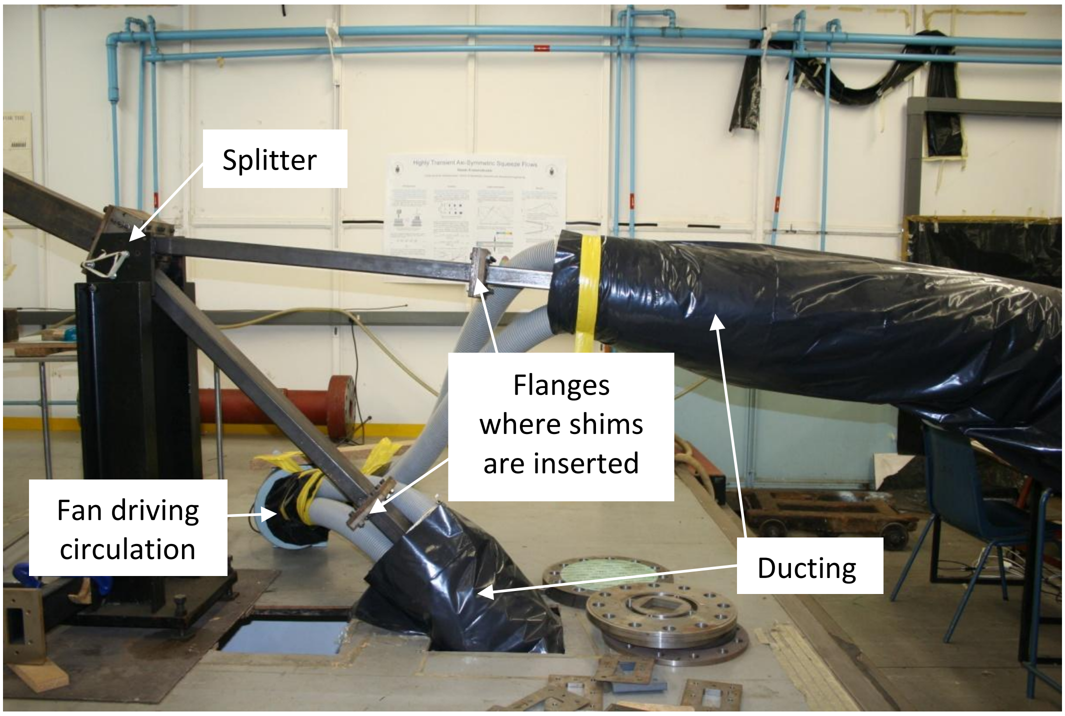

Figure 4.3 Upstairs portion of the bifurcated section

The upstairs room is situated below the roof of the laboratory and experiences much greater variation in temperature than the downstairs room. As a result the two legs of the shock tube, no matter what the arrangement of the bifurcated section, experience different temperatures. The temperature difference fluctuates continuously as the upstairs room follows atmospheric conditions and the downstairs room remains at an approximately constant temperature.

As the temperature varies, so does the local speed of sound in each of the legs, following from Equation 3.2. As the shock waves dividing into the bifurcated section are synchronous and equal strength, their equal Mach number means that they have different velocities due to this temperature difference that varies throughout the day. This velocity difference causes the shock waves to traverse the equal-length legs of the bifurcated section in different times and arrive at the apex of the wedge out of sync, except for two narrow time periods each day when the temperatures equalise.

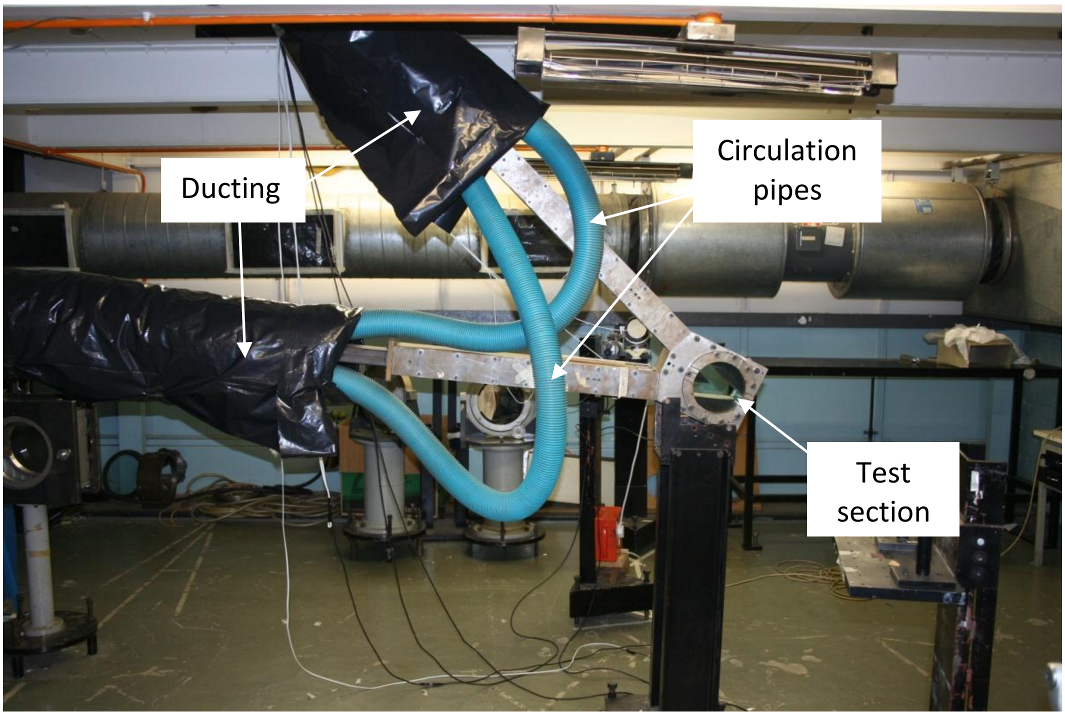

Figure 4.4 Downstairs portion of the bifurcated section

Insulated ducting that circulates air around both legs of the shock tube was installed to eliminate the temperature dependence of the synchronisation of the shock waves. Any remaining miss-synchronisation is constant and due to manufacture and assembly. This was compensated for by inserting shims into joints in the bifurcated section until the displacement between the shock waves was less than one millimetre on arrival at the wedge apex.

4.1.4. The ‘simple’ driver

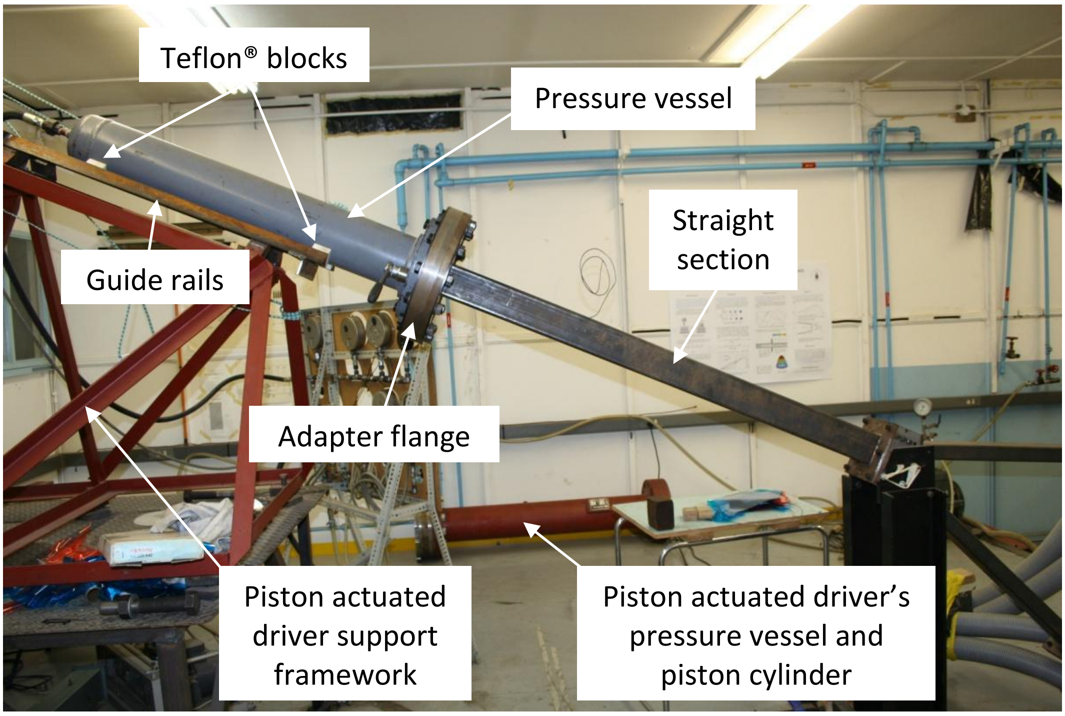

Figure 4.5 Simple driver and straight section

The piston-actuated driver has a limitation; the weakest shock wave that can be reliably generated has a Mach number of 1.1. A probable cause of this is the mechanism by which shock waves are generated in the piston-actuated driver. In the piston-actuated driver the piston is released and the pressurised gas in the pressure vessel drives it away before discharging down the shock tube as a shock wave. If the pressure used is too low to drive the piston rapidly the gas escapes gradually and a shock wave is not formed. Thus there exists a minimum pressure at which the driver generates a shock wave and as a result a minimum pressure ratio at which shock waves can be generated.

This Mach number is far removed from the theoretical transition Mach number for the 40° bifurcated section, where the Mach number of transition on a wedge of 20° is 1.02. This difference of Mach number implied that an extrapolation of the experimental data that could be obtained from using this driver would have to be over an extensive range resulting in large uncertainties.

To minimise the extrapolation range images at Mach numbers near the theoretical value needed to be obtained. It was assumed that a simple driver (a driver where a diaphragm, separating a pressurised region from the downstream region of the shock tube, is burst to generate the shock wave) would allow the weakest possible shock waves to be generated. To this end, the support structure of the diaphragm-less driver was adapted to receive a suitable pressure vessel that had been located in the laboratory.

To support the new pressure vessel in the place of the diaphragm-less driver's vessel and piston-cylinder a supporting framework was designed and manufactured to align the new pressure vessel with the downstream bifurcated section. The supporting framework attaches to the existing support structure via the blocks that the piston-actuated driver's pressure vessel had rested on. The support framework and block thickness accommodated the differences in diameter between the pressure vessels of the 'simple' and 'piston-actuated' drivers.

The new driver required that the pressure vessel be able to move relative to the downstream section of the shock tube, unlike the diaphragm-less driver where a breach was used to access the diaphragm on the reverse-side of the piston. To allow the motion of the new pressure vessel it was supported by and slid on blocks manufactured from Teflon®.

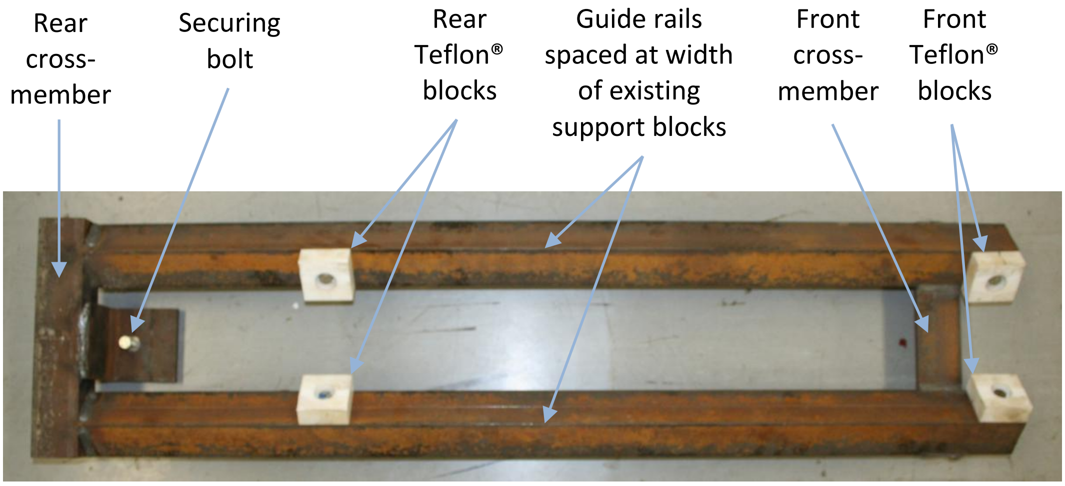

Figure 4.6 Guide rails

The guide rails were manufactured from steel members of the same cross-section as those used in the support frame for the existing driver. Angle iron sections were placed so that they fitted over the support blocks of the existing pressure vessel and provided a point of attachment for the supports of the new vessel.

The cross-members ensured that the rails maintained their relative position. This was important at the front of the guide rails nearest the attachment to the downstream portion of the shock tube, where the weight of the pressure vessel acts to drive the supporting blocks apart where their position not maintained between the support blocks of the piston-actuated driver, like the rear Teflon® blocks.

A flange with a securing bolt is attached to the rear cross-member. This allows the guide-rails to be secured to the existing framework of the piston-actuated driver. The securing bolt was necessary to counterbalance the weight of the pressure vessel, which had its centre of gravity beyond the supports that the guide rails rested on.

The pressure vessel’s centre of gravity was between the Teflon® blocks at all points in its travel and thus was not at risk of pitching out of the guide rails.

The new pressure vessel would plumb in directly to the bifurcated section of the shock tube via an adapter-flange that was designed and manufactured for the purpose.

The adapter-flange was water-jet cut from 44mm thick steel and was faced-off on a numerical milling machine to ensure that the surface was flat and smooth as the flange and pressure vessel would have to make an airtight seal. Holes corresponding to the bolt diameters and locations on the flange of the straight section were cut into the flange. In addition a ring of tapped holes were fitted concentrically within the outer ring that corresponded to the bolt locations on the new pressure vessel and allowed the new pressure vessel to be fastened to and tightened onto the face of the adapter-flange, sealing the joint.

A pair of 5mm thick ring flanges with smaller bolt holes and a larger bolt-circle radius were water-jet cut to act as washers and to clamp the adapter flange to the flange at the end of the straight section. The larger radius of the circle allowed the face of the pressure vessel to meet the adapter flange unhindered.

The piston actuated driver was fired by releasing the piston that contained the pressurised gas. The mechanism of the simple driver was to pressurise gas within the pressure vessel that had been sealed off from the downstream section by a sheet of diaphragm. The shock wave was generated by bursting the diaphragm by puncturing it using a wire-pricker that was inserted through a vent hole in the downstream section.

A guide vane was welded into the hole in the middle in the shape of a cross with a ring in the centre to guide the pricker. The pricker was inserted via the vent hole in the straight section prior to the bifurcated section to prick the diaphragm in its centre, causing an even burst.

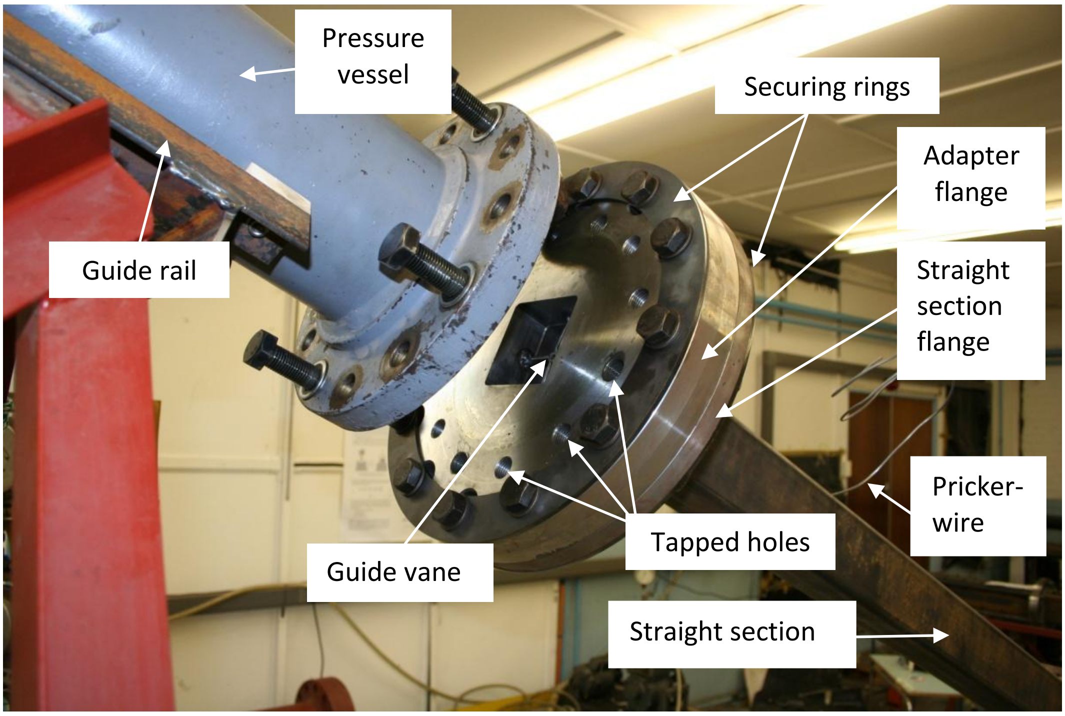

Figure 4.7 Adapter flange

To assist the motion of the pressure vessel a pulley system was arranged between the pressure vessel and the remaining components of the diaphragm-less driver. The assembly of the 40° bifurcated section in place of the 80° section was fairly seamless.

Through trial and error it was discovered that the material that allowed the weakest shock waves to be generated was cellophane wrapping paper, which gave shattering type bursts instead of tearing similarly to the diaphragm material used previously. The cellophane burst at minimal indicated pressure ratios (across the diaphragm to generate the shock wave) of approximately 1.1 when pricked, generating remarkably weak shock waves of $M = 1.029$. Using this driver there is only an extrapolation of $\Delta M = 0.01$ to be carried out instead of an extrapolation of $\Delta M = 0.1$.

Interestingly the different shades of cellophane wrapping paper burst at different pressures, with certain shades not shattering when pierced by the pricker, instead they dissipated the pressure through the hole left by the pricker and caused the test to fail. It was found that dark blue shaded cellophane shattered most readily.

The simple driver was used to obtain 11 well synchronised images of mutual reflection of synchronous equal strength shock waves at the apex of a 40° trailing wedge.

It was intended to use the simple driver for all the experiments, to forgo the time and effort of reinstalling the large pressure vessel of the diaphragm-less driver, however experiments at higher Mach numbers showed that the simple driver was not suitable.

The tests at higher Mach numbers showed a large scattering of mis-synchronisation between the two legs of the apparatus in spite of the effect of the ducting. A running plot that was used to identify this error is included below. The ellipses bracket series of tests that were conducted at the same driver settings.

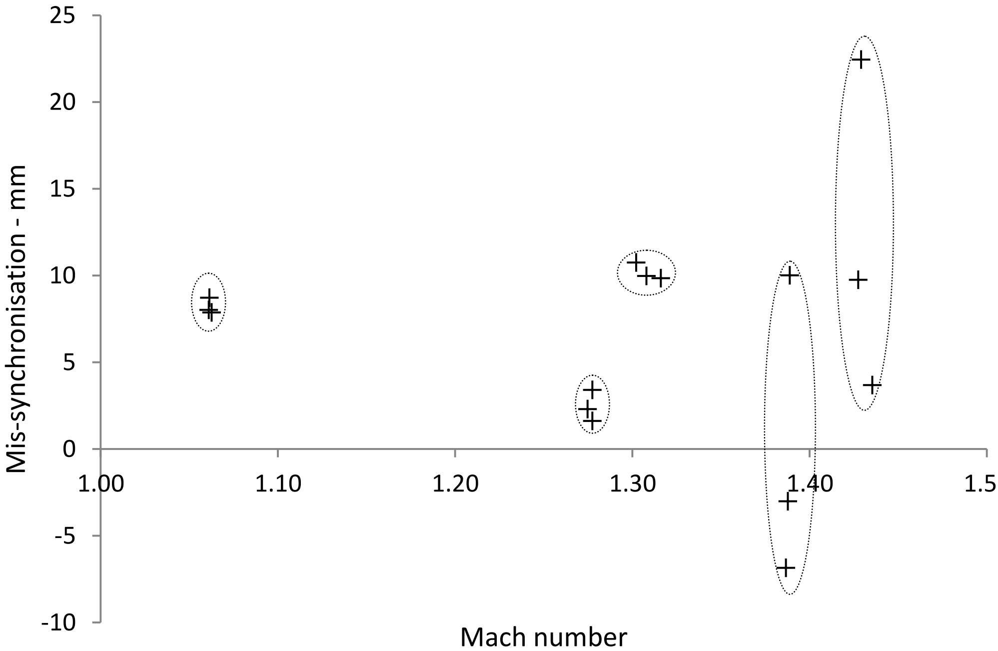

Figure 4.8 Running plot of Mach number and mis-synchronisation

From Figure 4.8 it can be seen that three groups at lower Mach numbers had a small scatter between them in terms of Mach number and synchronisation, as is typical in tests using the bifurcated shock tube. The middle group of the three has a different mean-mis-synchronisation due to the fitting of a shim to one of the legs. The two groups at higher Mach numbers however, using the 'simple' driver above Mach numbers of approximately 1.35, the scatter on sequential tests became large and erratic.

Consistent mis-synchronisation is compensated for by shimming the appropriate leg of the apparatus. Mis-synchronisation due to temperature variation was accommodated for by installing ducting on the legs of the shock tube, and is identifiable by its variation that is proportional to the temperature difference between the upstairs and downstairs rooms.

It is postulated that this large erratic variation in synchronisation that was observed in spite of the abovementioned measures is due to insufficient distance for disturbances resulting from the burst-process to become regularised. In the simple driver the shock wave only has the length of the straight section in which to become smooth and planar before encountering the splitter. It is believed that the distance is insufficient for the relatively uneven burst-process of the simple driver to even out into a even normal shock wave prior to the bifurcation, resulting in a pair of shock waves of randomly uneven strength.

The piston actuated driver had demonstrated that it could generate shock waves that were stable by the time they encountered the splitter in the investigation conducted by Barbosa (3). The piston-actuated driver did not suffer from the problem of random mis-synchronisation in the Mach strength regions that it had been used to test on. This is probably as a result of the smoother process for the generation of the waves through the operation of the piston and the greater length available, due to the reversed direction of the driver that opens at the upstream side, for the generated wave to become planar prior to encountering the splitter.

The pressure vessel of the diaphragm-less driver was reinstalled and the driver was re-commissioned for the testing on the 96° section.

The curved sections of the bifurcated portion of the shock tube for the 96° arrangement were slightly too curved from the rolling process, as was discovered when the assembly was attempted and final alignment proved impossible. In order to complete the assembly the curved sections were 'relaxed'.

With one end fixed to the partially assembled apparatus the other end was coaxed towards the machined section that had been fitted to the test section, while the middle portion of the curved section was heated with an acetylene torch by a laboratory technician. By this means the residual stresses of the rolling process were relaxed and the downstream section brought into alignment. Once the sections had cooled in their new orientation the final assembly was completed.

Once the ducting had been installed a series of tests were conducted to determine what the consistent mis-synchronisation of the assembled apparatus was. The mean length was then accounted for by inserting a shim of the appropriate width between two flanges at the joint between curved section and the straight tube that led to the machined section.

4.1.5. The piston-actuated driver

The facilities manufactured for the bifurcated shock tube included a diaphragm-less piston-actuated shock tube driver and three sets of bifurcated sections at angles of 40°, 80° and 96°, corresponding to normal reflection studies on wedge angles of 20°, 40° and 48°. While the driver is called 'diaphragm-less' it's operation requires a diaphragm be burst to generate a shock wave. The 'diaphragm-less' description refers to the fact that the shock wave is released by the discharge of air from a pressure vessel brought about by the motion of a free-floating piston.

The driver consists of three pressure-vessel sections; the vacuum section, the piston cylinder and the pressure vessel.

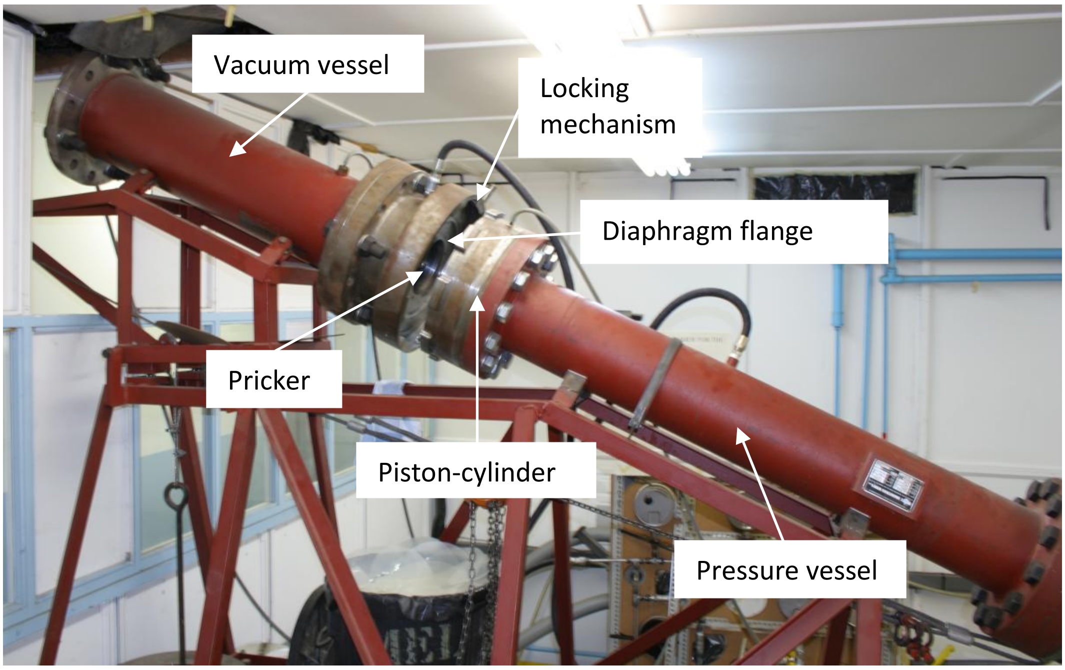

Figure 4.9 Picture illustrating the components of the piston-actuated driver

Figure 4.9 illustrates the main functional components of the piston actuated shock tube driver. The main pressure vessel has its stored pressure released at its one end. The pressurised air is released by a piston constraining it and turns through 180° against the face of the piston that was originally constraining it and proceeds down the shock tube.

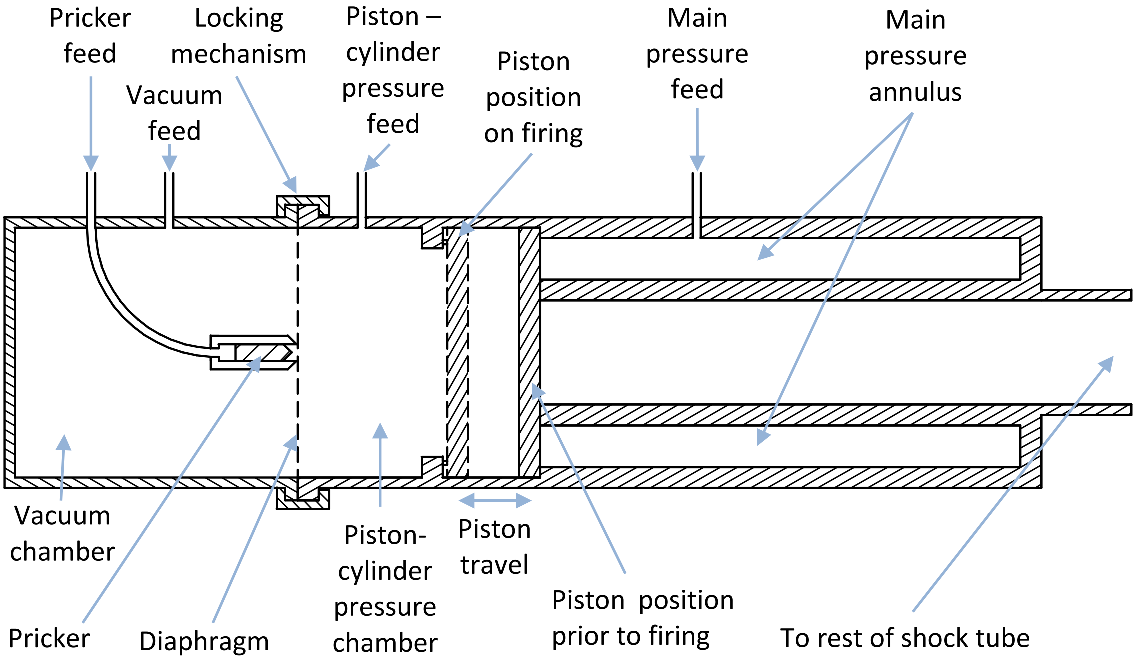

Figure 4.10 Schematic layout of components of diaphragm-less driver

The diaphragm separates the vacuum vessel and the pressurised cylinder of the piston. The pressure on the face of the piston allows it to hold the primary pressure vessel sealed. When the diaphragm separating the vacuum vessel from the cylinder is burst it brings about the motion of the piston by releasing the pressure that keeps the main pressure vessel sealed via the piston. The piston is able to keep a higher pressure of the main pressure sealed by the relative areas on which the pressures on each side of the piston act upon.

The main pressure vessel is an annulus around the discharge pipe, smaller in cross-sectional area than the cylinder side of the free-piston. The main vessel is sealed at the end facing the downstream section of the shock tube. The annulus of high pressure and the inner tube that connects to the downstream section open at a flat face that is sealed by the downstream-face of the piston.

When the diaphragm separating the vacuum vessel from the pressurised cylinder is burst the pressure difference holding the piston in place and hence constraining the main pressure is released. This generates a shock wave that travels out of the annulus, reflects off the face of the piston and travels down the shock tube from the driver. This additional sophistication of the shock wave generation process results in highly repeatable shock wave generation of planar waves.

4.2. Measurement equipment

4.2.1. Optics system

Filipe Barbosa recorded images of the mutual interaction by laser interferometery on a film plate placed against the surface of the window. As there is no distance between the interaction and the imaging material this technique is free from optical distortion. The availability of high resolution digital cameras and the greater speed and simplicity associated with their use was the rationale for selecting a shadowgraph optical system for this investigation.

The shadowgraph optical layout consists of a light source (Hammamatsu C3684 power supply and xenon flash lamp), knife edge, a pair of 100mm diameter spherical mirrors, a pair of condensing lenses and a digital camera (Cannon 350D, serial number 0230109500, 8 mega-pixels). The arrangement is illustrated below:

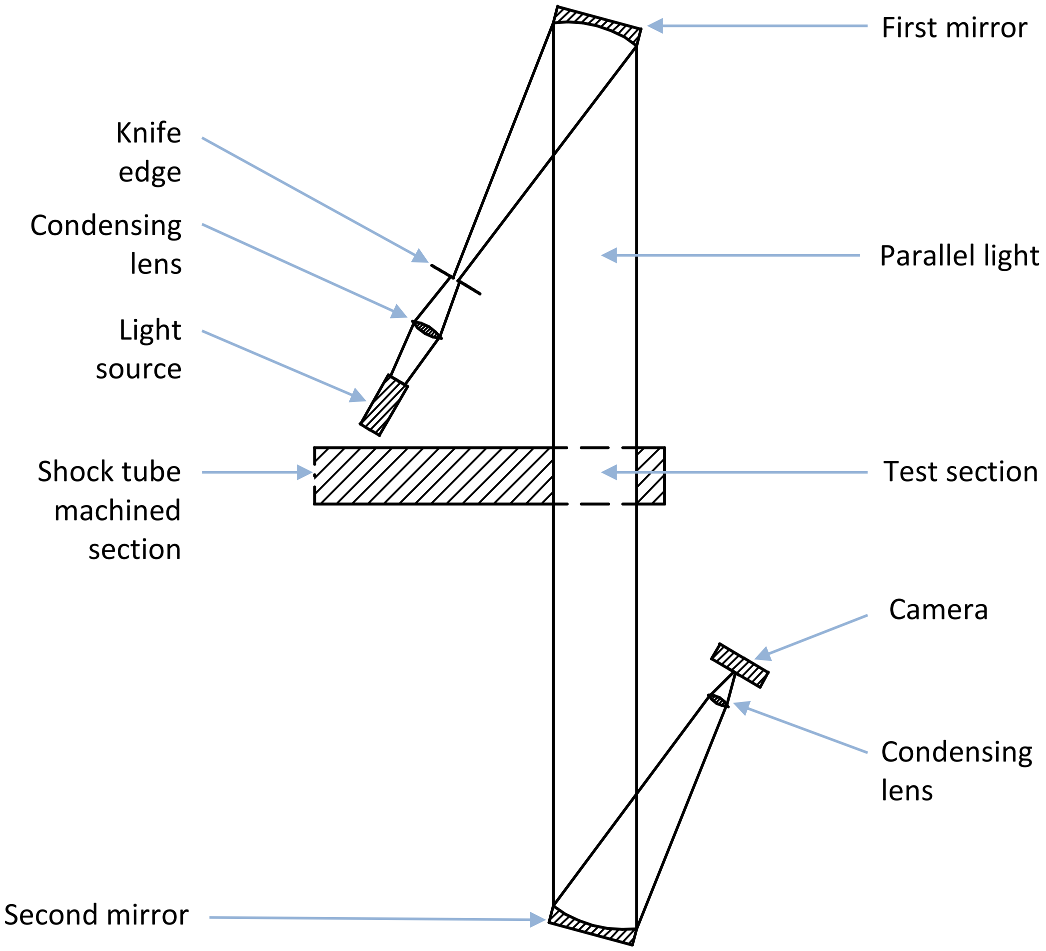

Figure 4.11 Plan view of shadowgraph optical layout

Light is generated by the light source in response to a trigger signal generated by a trigger box attached to a feed from the pressure transducer. The trigger box is set to its maximum sensitivity and detects sharp changes in the voltage in the amplified feed from the transducer. When the trigger box receives a signal that is sufficient to cause it to trigger, it instantaneously generates a +5V signal on its output coaxial feed. This is connected via a delay box that has been pre-set and after the programmed delay causes the light-box to trigger, resulting in the xenon bulb flashing at the appropriate time.

The light from the arc is focused to a point by a condensing lens. An adjustable knife edge is placed at the focal point of the image of the filament to vary the brightness and sensitivity of the image. The knife edge was oriented with its' slit perpendicular to the line image of the filament to turn the line image of the arc into a point source of light in the optical system.

The point source that results from the knife edge is used as the reference for placing the mirror in the optical system. The mirror is placed so that it is its' focal length from the light source and has its centre perpendicular, both horizontally and vertically, to the portion of the test section that is the focus of the image. The lamp, lens and knife edge have their position adjusted until this is so.

This is tested for by using the small fraction of the light that is reflected from the window surface back onto the mirror and focusing it on the face of the knife edge, and adjusting the mirror until the reflected light and the source light coincide at the knife edge. This ensures that the light beam is perfectly perpendicular to the window, and if a point source image is formed on the knife edge, implies that the mirror is located at the correct distance from the knife edge.

A mirror that is located at its focal length from a point source of light will cast a beam of parallel light through the test section. Any light that is refracted by a density gradient within the test section will diverge from this parallel beam and will appear as a dark portion within the uniform light distribution in an image of the beam. This is the fundamental premise of a shadowgraph optical system – shock waves and contact discontinuities bend the portion of the parallel light that is incident upon them and show up as dark regions in the resulting image.

The parallel light that has been flashed through the test section and contains an image of shock wave interaction then passes through, and has superimposed upon it, an image of the calibration grid.

Once it has passed through the calibration grid the light then continues to the second mirror that is aligned at the reverse orientation to the first mirror with respect to the light source. This z-shaped reflection causes the shadowgraph image to be free from distortions resulting from the slightly angled reflection of the original mirror (4).

The image that is converging from the second mirror is then passed through a converging lens to focus it onto the CCD (charge-coupled device) of the digital camera. The entire imaging process takes place in a dark room, the downstairs room of the bifurcated shock tube, with the camera's shutter held open and the flash of the light timed to record the event at the appropriate moment.

4.2.2. Calibration grid

Any optical aberrations arising from a slight misalignment of the optical system can change the aspect ratio of the overall image or cause local distortions. Any distortion of the image that changes the aspect ratio or moves the apparent location of the triple point or tip of the wedge will cause an un-quantifiable error in the measurement of the triple point trajectory angle.

To compensate for these distortions that were evident from early tests calibration grids were designed and installed on the window frames of the test sections of the shock tube in a similar location to where the film would be placed in Barbosa's tests. The calibration grid consists of two sets of four parallel wires stretched between CNC machine-cut grooves in the window frame, forming a four by four grid overlying the portion of the image that the interaction takes place in.

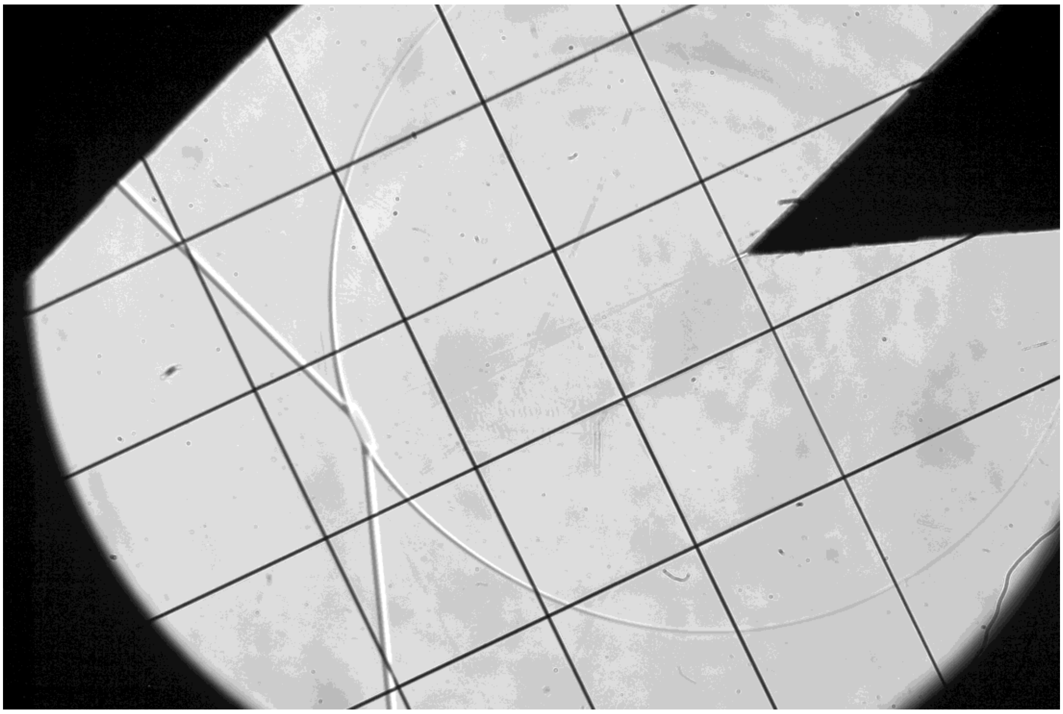

Figure 4.12 Calibration grid and shock wave interaction

(Test 99; M_s = 1.061, stem angle = 2.42°, mis-synchronisation = -0.73mm)

Figure 4.12 shows a typical image of a synchronous symmetrical reflection occurring in a bifurcated shock tube. The image illustrates the calibration grid and the reflection process. The same image is included below illustrating the measurement lines that were superimposed with a CAD (Computer Aided Drawing) program (SolidEdge v.19). The lines were all measured with respect to the bottom-left most intersection of the wires forming the calibration grid. All points of interest on the image were measured with respect to this point, and measurements are recorded by the CAD program as lengths and angles, which were measured to five and four significant figures respectively. All manipulation actions performed on the measured data for processing, i.e. rotation to a Cartesian orientation of the grid, were carried out equally on all the data points.

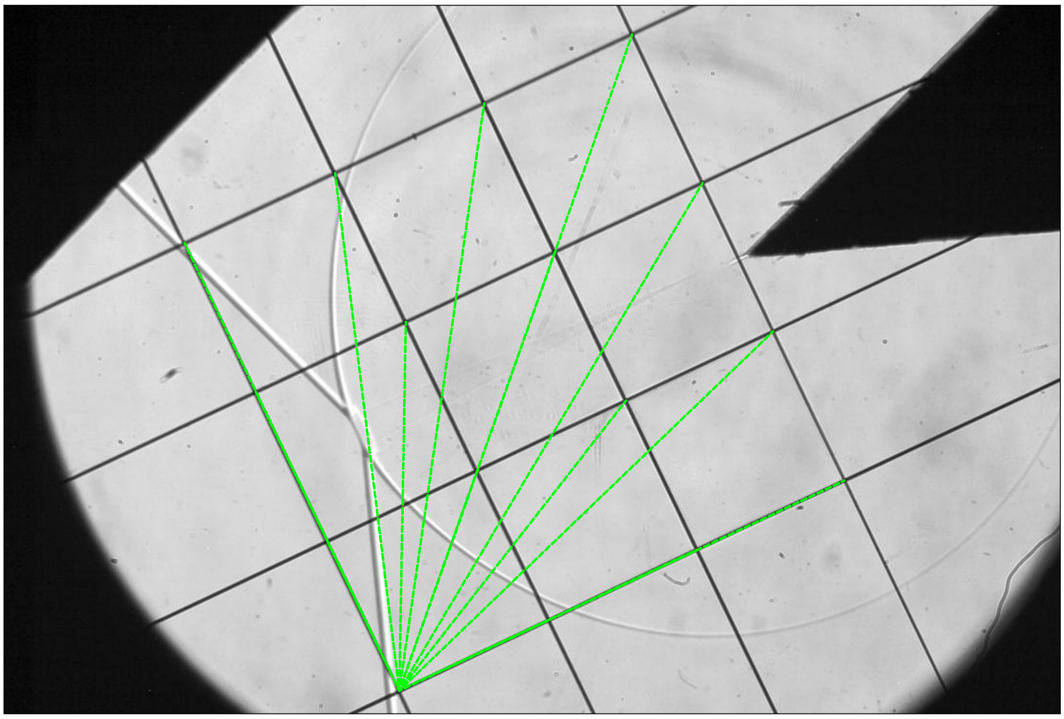

Figure 4.13 CAD measurement lines

The 16 loci of the crossing points of the wires are accurate to within 0.5mm as the wires are set in their CNC grooves under tension. Therefore the spacing and perpendicularity of the lines that make up the image of the grid that is superimposed on the image of the interaction is assured, and if the grid appears to be irregularly spaced or trapezoidal in shape then it can be assumed that it is due to distortion in the optical system. The measurements in this study are susceptible to error as a result of distortion of the image, as a skewing of the image could make the measured angle to appear to be greater or smaller than otherwise.

To correct for any and all optical aberration all images obtained of interactions that are sufficiently-well synchronised are passed through an image correcting code written by R. Paton. The Matlab code is included in appendix C.

The code corrects for optical distortions in the image by using the loci of the calibration grid crossing points and fitting them to a perfectly square grid. It uses the amount of adjustment necessary for each of the grid points, both horizontally and vertically, to develop an adjustment polynomial for each line of the grid, again horizontally and vertically. The co-efficients of each of the adjustment polynomials are then used to find polynomials of how the co-efficients vary with each horizontal and vertical strand that makes up the grid. From these co-efficients, a vertical and horizontal adjustment-polynomial can be found for any point within the grid. The point's new vertical position is found by inserting its' horizontal position into is vertical adjustment polynomial and vice versa for its horizontal position.

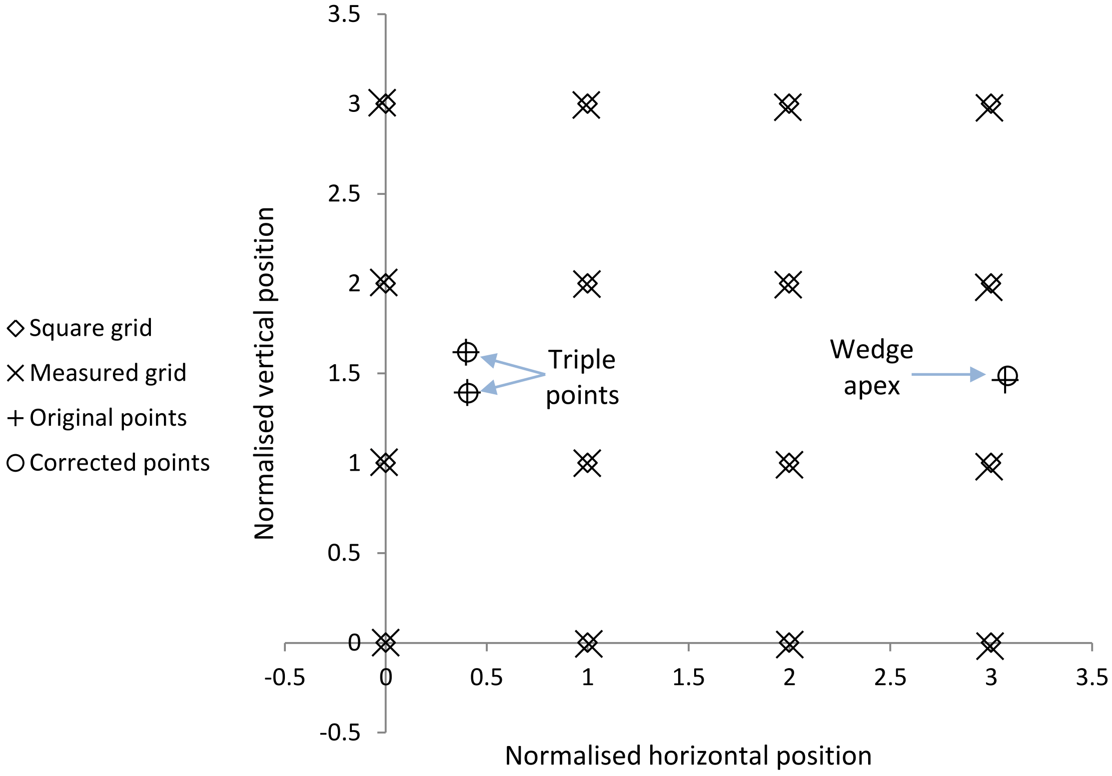

Figure 4.14 Image calibration before and after

Figure 4.14 shows how the measured grid is slightly misaligned from the perfect square grid. The original measurements and the positions of the corrected data points are plotted to illustrate the slight changes in position brought about by the calibration process. Prior to input into the calibration curve all the data are rotated by the average angle of incline of the grid and normalised with respect to the average grid size. As both these processes are applied to all the measured points, of both the grid and the reflection process, no change in the angle or relative position of the points occurs.

As is evident in Figure 4.12 and shown in the measurement in Figure 4.14 the apex of the wedge is slightly outside the grid area. The polynomials developed by the calibration process have been shown to allow accurate corrections to 5% of the grid size beyond the limits of the grid, and the apex of the wedge falls within this region.

4.2.3. Data acquisition

For each test traces were recorded from a pair of pressure transducers in the machined sections just prior to the test section in each leg of the bifurcated shock tube. The input from the piezoelectric pressure transducers (PCB Piezotronics 113A21 serial numbers: 5477, 7343, 8288 and 8728) was amplified 10x before being recorded on a data acquisition unit (Graphtec GL1000-8, serial number D80960037). The pressure traces were then processed in order to determine the Mach number and mis-sychronisation of the incident shock waves.

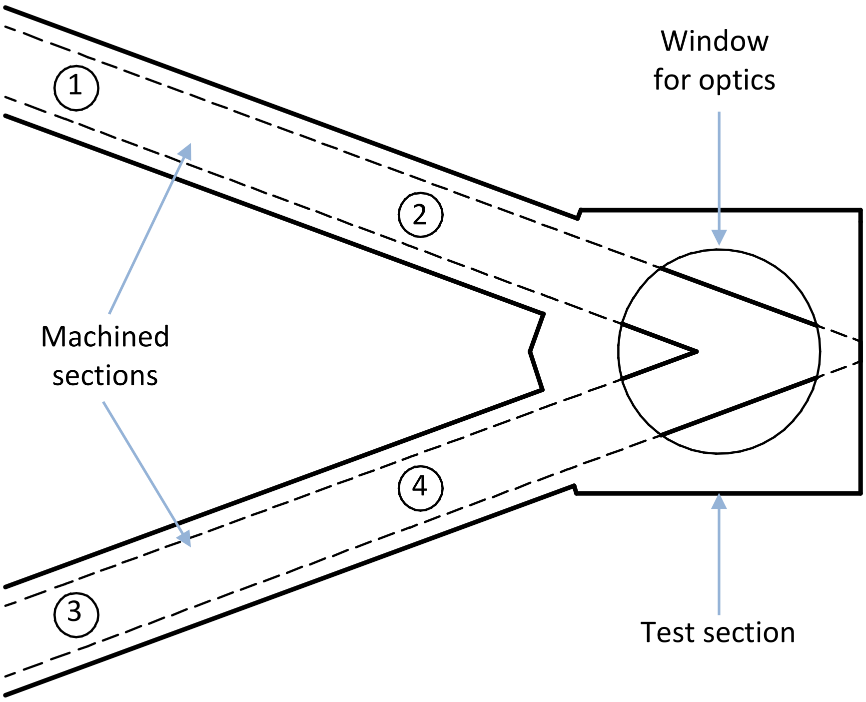

Figure 4.15 Diagram of transducer locations with respect to wedge apex

The plots of the readings from the piezoelectric pressure transducers were used to determine both the Mach number and the synchronisation of the shock waves in the legs of the bifurcated shock tube just prior to the test section. The locations of the transducers are illustrated in Figure 4.15

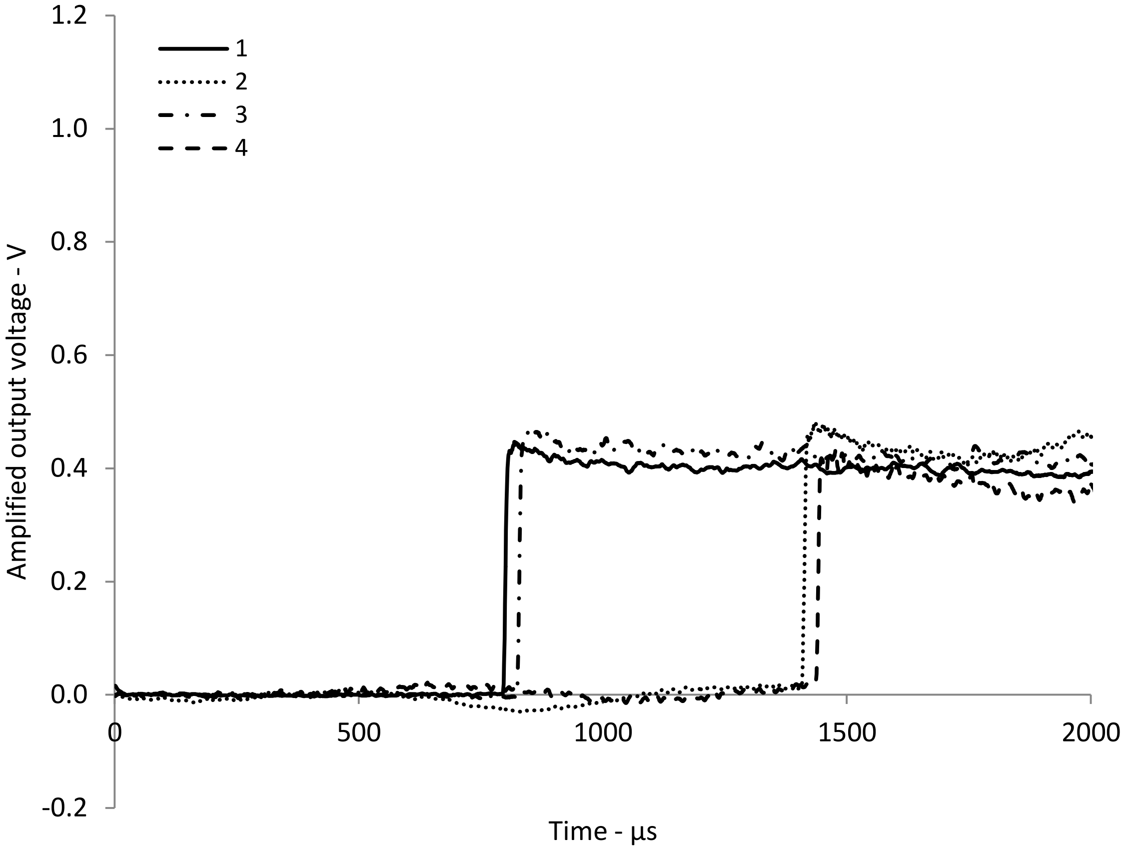

Figure 4.16 Running plot of transducer output

Figure 4.16 illustrates the step change in the output as the shock wave passes over the pressure transducer. From the plot it can be seen that the shock waves pass over transducers 1 and 3 before passing over 2 and 4. The figure also shows that the waves pass over the 1 and 3 at slightly different times and that this difference has increased by the time that the shocks pass over transducers 2 and 4. This is illustrative of two of the sources of error in the bifurcated shock tube, both the mis-synchronisation of the two shock waves and the difference in wave speed and hence Mach number between the shock waves in the two legs of the tube.

The second step change in pressure evident in the readings from transducers 2 and 4 is caused by the shock waves reflecting off the end of test section and back up the shock tube. The rise is not shown in the traces from transducers 1 and 3 as the waves had not reached the transducers by the time the data acquisition system stopped recording the test.

The pressure trace from each channel is filtered to reduce the noise on the signal and allow a more accurate determination of the time that the shock wave passes the pressure transducer. The filtered transducer traces from Figure 4.16 are shown in Figure 4.17.

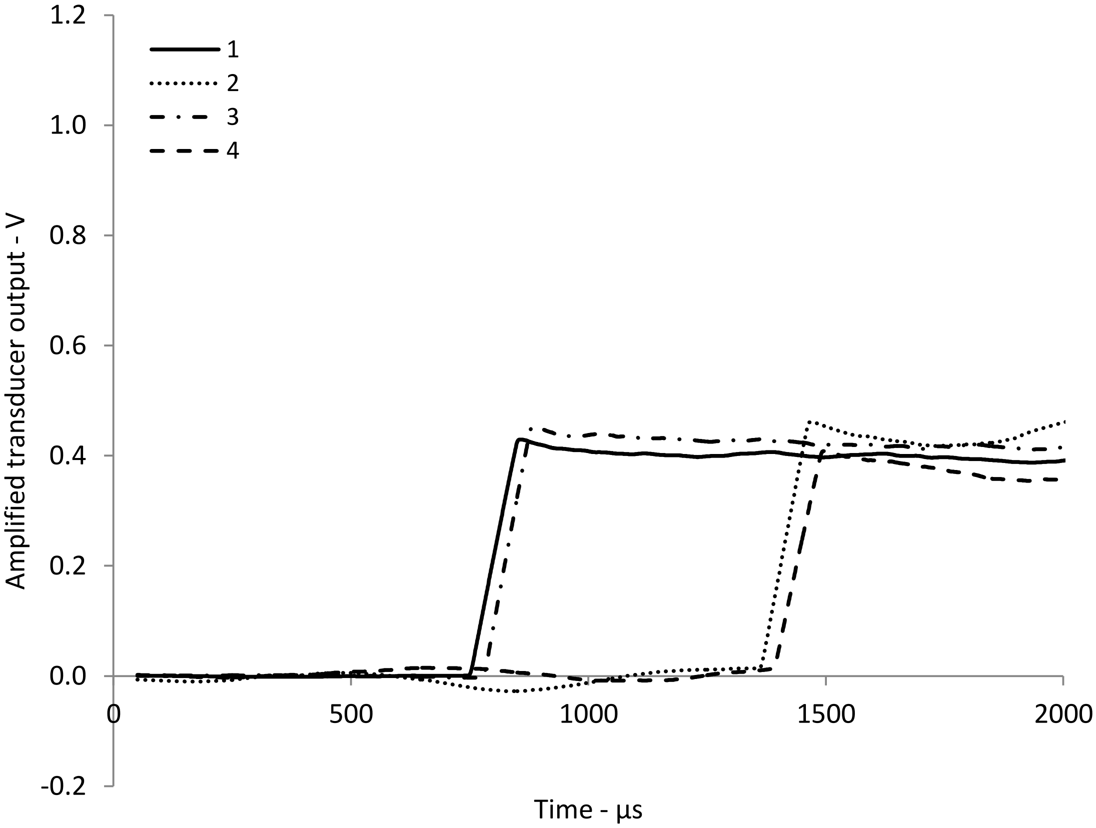

Figure 4.17 Filtered transducer output

The speed of the shock wave in each leg is calculated by dividing the distance between the transducers by the time difference between the shock traversing the transducers. The transducers are located 310mm apart. The transducer ports were machined by a numerically controlled milling machine and as a result the estimated uncertainty of the distance between the ports is 0.1mm.

The time for the shock wave to cross the pressure transducer was calculated from the delta values of the pressure trace. The delta values are the change in the output from the pressure transducer between sequential readings. The delta values for channel 1 from Figure 4.17 are illustrated below.

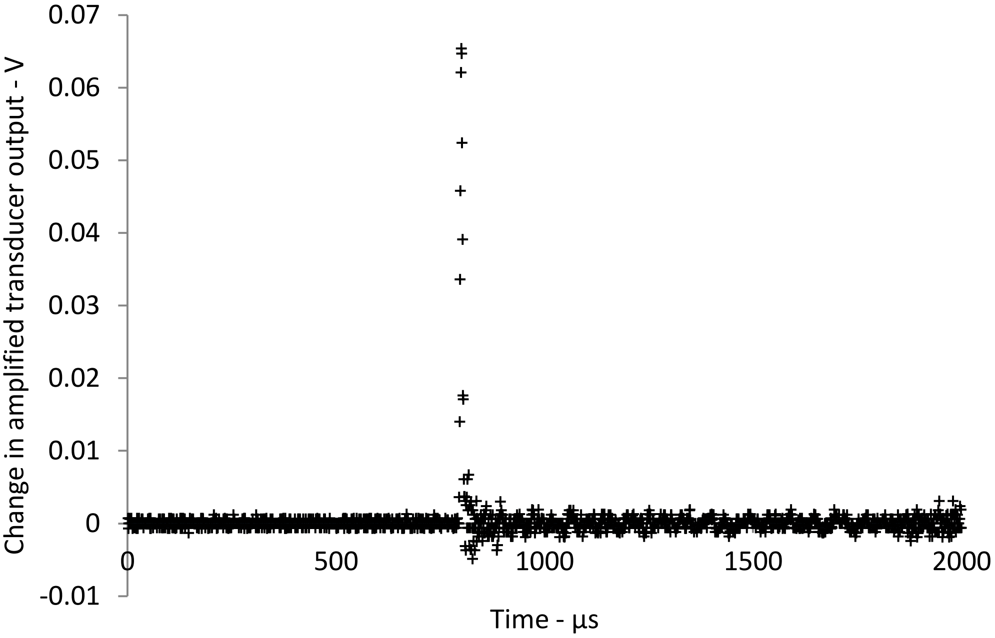

Figure 4.18 Delta values from trace from transducer 1

The sample rate of the data acquisition system was one million samples per second per channel. The spike in the delta values corresponds to the shock wave crossing the pressure transducer. The spike is made up of approximately 14 data points the peak of which could be assumed to be the mid-point of the shock wave crossing the pressure transducer. As all of the pressure traces were logged with respect to a common time reference the wave times for the four channels could be measured this way.

The measured wave time has an assumed uncertainty of 2 µs when based on the peak delta value, with the uncertainty primarily due to the noise band on the pressure trace. While this uncertainty is considered acceptable for the measurement of the time interval between the shock wave crossing the transducers in the same leg of the shock tube it is too large to be an accurate measure of the synchronisation of the shock waves in the different legs of the apparatus. 2 µs is small in comparison to the 600 µs measured as the time taken for the shock wave to cross both transducers in a leg, but is significant in comparison to the maximum mis-synchronisation of 2.83µs that results in a mis-synchronisation of 1mm at Mach 1.029.

In order to increase the accuracy of the measurement of the time that the shock wave crossed the pressure transducer the pressure traces were filtered by replacing each value by the average of 100 data points, 50 from each side of the point. The effect of this filtering is shown in Figure 4.19, below.

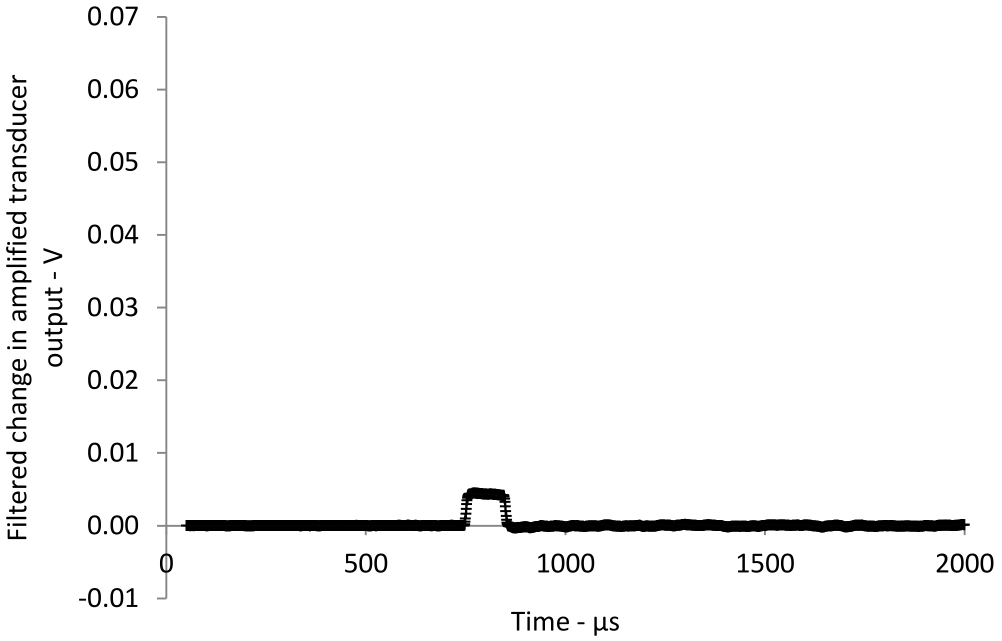

Figure 4.19 Filtered delta values from trace from transducer 1

The effect of filtering the pressure transducer output removes the noise band from the delta values and creates a plateau of delta values corresponding to the smoothed shock wave time. The time-values corresponding to this plateau, the points of which were found by finding the values with a magnitude of 60% of the peak value of the filtered delta values, on each of the four signals. These values correspond to the plateau and are averaged to determine the time the shock wave crosses each pressure transducer without the influence of the noise band. This averaged value corresponds to the time the shock wave traverses the centre of the pressure transducer. The uncertainty is assumed to be 0.5 µs which is half the time interval between respective data points.

4.3. Measurement techniques

4.3.1. Measurement of shock wave Mach number

The Mach number is calculated from a combination of Equation 3.1 and Equation 3.2.

Equation 4.1

$$\mathrm{M} = \frac{\mathrm{v}}{\mathrm{a}} = \frac{\frac{\mathrm{x}}{\mathrm{t}}}{\sqrt{\gamma \mathrm{RT}}}$$

Where x is the distance between the pressure transducers and t is the time interval for the shock wave to travel between the two pressure transducers in each leg of the apparatus. To determine the error in the calculated Mach number a partial differential of the Mach number formula is taken and the partial errors in each of the terms are summed.

Equation 4.2

$$\frac{\Delta M}{M} = \frac{\Delta x}{x} \pm \frac{\Delta t}{t} \pm \frac{1}{2}\frac{\Delta T}{T}$$

The uncertainty in x is 0.1mm, 0.5μs in t and 0.5K in T. For test number 109, a Mach number of 1.062 was calculated from the measured time interval of 845μs for the shock wave to cover the 310mm between the transducers at an ambient temperature of 296.5K. The resulting uncertainty in Mach number is 0.0019 as a result of the accuracy of the component measurements.

There is an additional source of error in the quoted Mach number that arises from the slight difference in shock wave strength in the two legs of the shock tube. This difference in Mach number, 0.0025 in test 109, is then added to the uncertainty from the above calculation. The total uncertainty is 0.0044.

In all the tests that are considered to be sufficiently synchronised (shock waves meet at the wedge apex with a separation of less than 1mm) the largest uncertainty of Mach number is 0.0081. The Mach number can be quoted with confidence to two decimal places as a result.

4.3.2. Mis-synchronisation measurement

The measure of the mis-synchronisation of the shock waves at the wedge apex is quoted in terms of the distance between the shock waves in each of the legs at the apex of the wedge. The distance between the shock waves is calculated from the time separating the shocks and the speed of each of the shocks.

The time separating the shocks is measured 250mm upstream of the wedge apex by the pressure transducers in each leg. This measure is modified by the change in synchronisation that is brought about by the different speeds of the two shocks. This additional time separation is calculated by dividing the distance from the transducers to the wedge apex by the speed difference of the shock waves.

This time mis-synchronisation is multiplied by the average speed of the shock waves to calculate the distance separating the incident shocks.

The images of the mutual shock wave interactions that were well synchronised are analysed to determine the angle subtended by the Mach stem with respect to the reflecting surface. In an effort to measure the angles of the interaction accurately and give an indication of the certainty of the measurement a method that conservatively bracketed the reflection process was adopted.

The inner and outer points of the reflection interaction are found by fitting curves to the incident and reflected shock waves, a straight line and an arc respectively, using a CAD program (SolidEdge v.19) with the image imported as a background. The curves are fitted to each side of the region that the shock wave occupies, meaning that a pair of arcs fitted to the reflected waves and a pair of straight lines fitted to the incident waves, resulting in two intersection points for each reflection.

The self-similar angle subtended by the triple-point with respect to the plane of symmetry, also called the stem-angle, is measured for in the symmetrical case by taking the arctangent of the quotient of its' perpendicular height to the midpoint of the interaction and the length from the midpoint to the wedge apex. As the measured points of the interaction are rotated and described by Cartesian co-ordinates for the image calibration, the horizontal and vertical measures are guaranteed. The horizontal position for the angle is found by averaging the horizontal positions of the interaction points for each of the two angles measured. The vertical position for the angle measurement is found by halving the vertical difference between the intersection points on each side of the plane of symmetry.

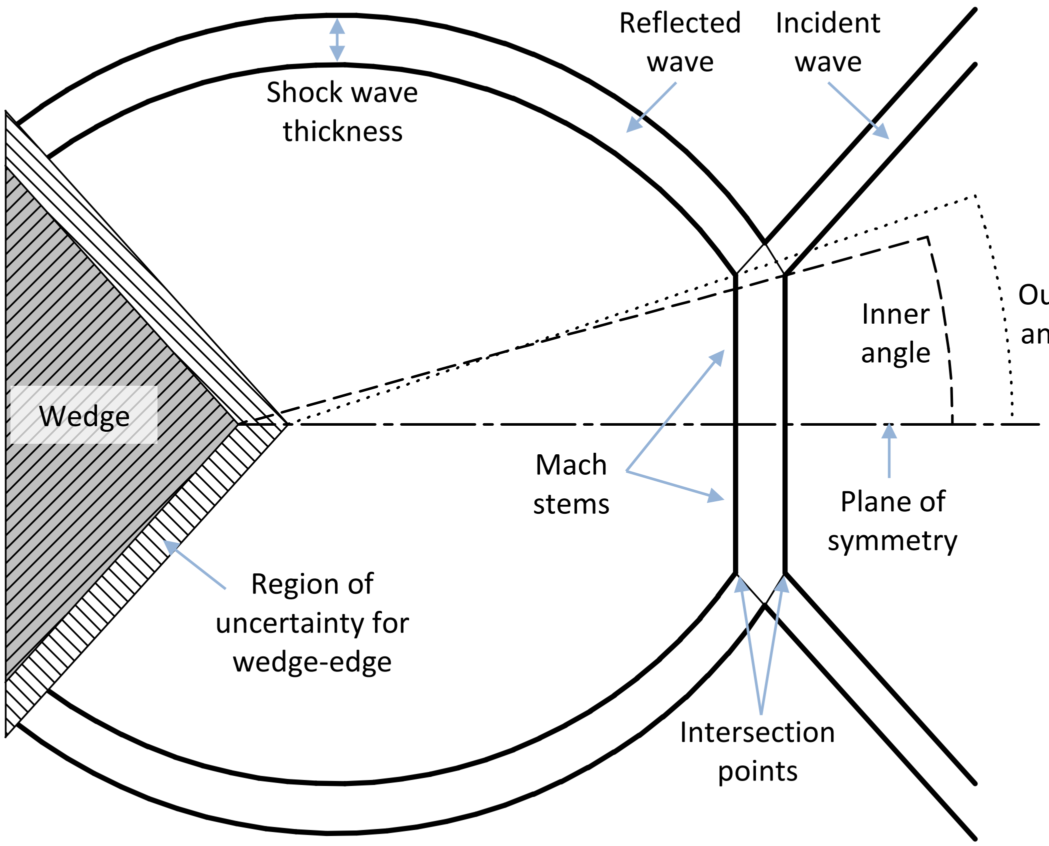

Figure 4.20 Illustration of the angle measurement technique (exaggerated)

Figure 4.20 shows the two measurements that were taken to ‘bracket’ the reflection process. The outer angle is measured from the limit of the uncertain position of the wedge that is closest to the interaction and is measured to the innermost points of the reflection process, thus measuring the broadest possible angle the interaction could take.

The inner angle is measured from the limit of the wedge’s uncertain position away from the from the reflection process with respect to the furthermost point of the interaction of the incident and reflected waves.

The average of the inner and outer angles is assumed to be the angle of the reflection for a particular image, as that should correspond to the midpoints for the wedge and the reflection geometry. Half the difference between the outer and inner measurements is assumed to be the error in the angle measurement, hence the error bounds in the plots of the result indicate the limits of the measured values using the above technique.

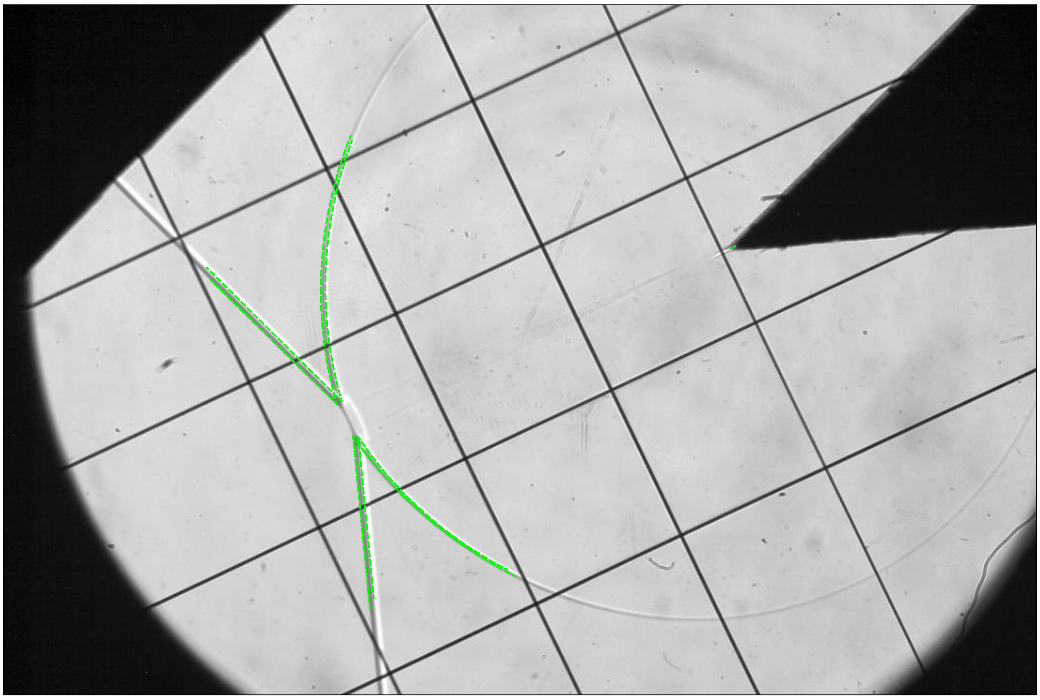

Figure 4.21 Shadowgraph image from test 155 with fitted lines

(M_s = 1.061, stem angle = 2.56°, mis-synchronisation = -0.73mm)

Figure 4.21 shows how the lines and arcs are fitted to the reflection geometry to bracket the possible reflection points.

5. Results, analysis and discussion

The investigation of the transition from regular to Mach reflection on wedge angles of 20° and 48° required a number of well-synchronised images of shock wave reflection over a range of Mach numbers for both the 40° and 96° orientations of the bifurcated shock tube.

Altogether 25 images of sufficient synchronisation and optical quality were obtained from 242 tests conducted on the bifurcated shock tube apparatuses. 11 images were obtained for the 40° bifurcated section with the simple driver and 14 were obtained for the 96° arrangement with the piston-actuated driver.

The successful tests were used with a variety of statistical techniques to infer the Mach number at which the transition from regular to Mach reflection occurred by extrapolating the relationship between the stem angle and Mach number for each of the two arrangements of the apparatus.

This inferred transition Mach number is the transition Mach number that results from reflections that are free from both thermal and viscous transport phenomena.

5.1. 40° bifurcated section, 20° wedge

5.1.1. Typical shadowgraph image

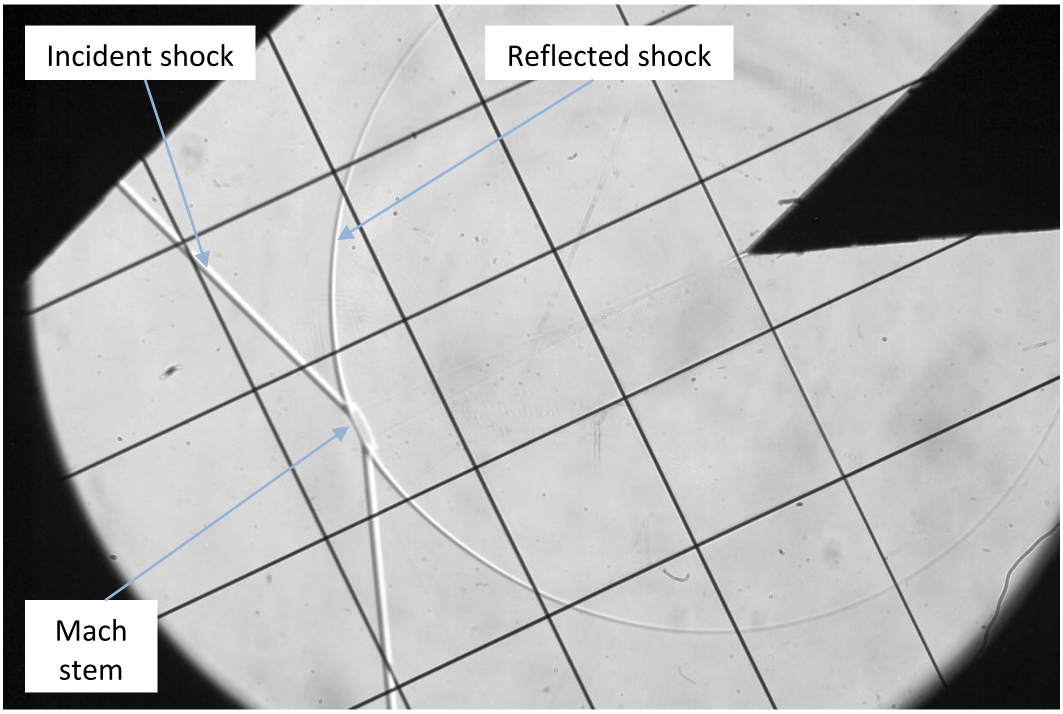

Figure 5.1 Typical image obtained from 40° bifurcated section

(Test 155, Ms = 1.061, stem angle = 2.56°, mis-synchronisation = -0.73mm)

Figure 5.1 is a shadowgraph image obtained with mis-synchronisation less than one millimetre at a Mach number of 1.061. The shock waves are travelling from right to left in the figure.

Due to its relatively high Mach number with regard to the transition Mach number of approximately 1.02, it has a large stem angle and clearly illustrates the features of Mach reflection. The incident and reflected shock waves meeting at the triple-point at the apex of the Mach stem and the reflection geometries formed from each leg of the bifurcated section are mirrored about the symmetry plane.

5.1.2. 40° results

The measurements for the images from the 40° arrangement of the bifurcated section are illustrated in the following figure. The symmetry of the reflection process means that the measurements are comparable to those obtained from a reflection process occurring on a wedge inclined at 20° to the incident shock wave.

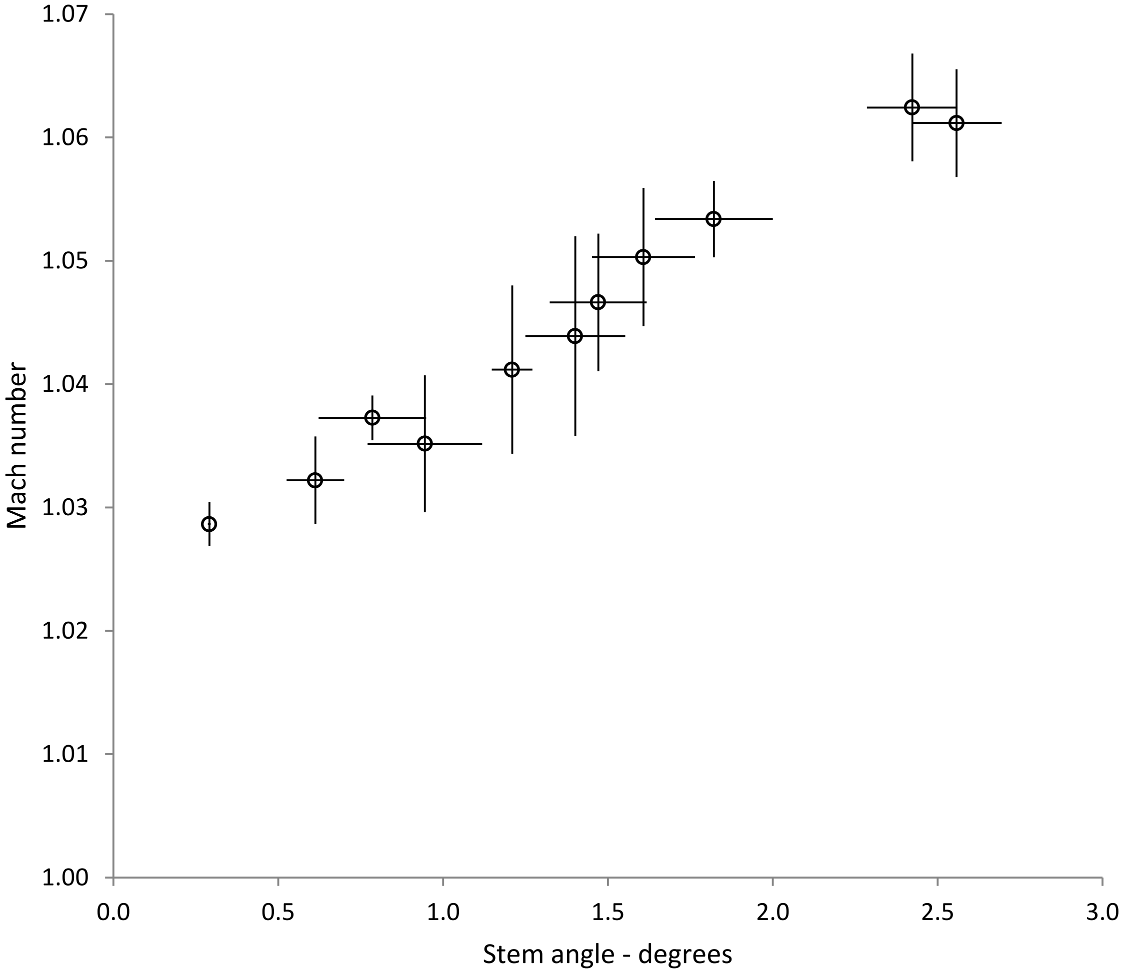

Figure 5.2 Measured stem angles from 40 degree apparatus

Figure 5.2 shows the measured angles and Mach numbers for the viable tests conducted using the 40° arrangement of the bifurcated shock tube with the simple diaphragm driver. Immediately apparent from the data is the trend towards an origin on the vertical axis at a Mach number between 1.02 and 1.03. The theoretical transition Mach numbers for a 20° wedge based on the sonic and detachment criteria are 1.0169 and 1.0178 respectively. Also apparent in the figure is the variability of the error bounds on the data.

The portion of the error in determining the Mach number, ΔM, that is due to uncertainty in the measurements required to determine the Mach number is relatively small in comparison to the uncertainty that arises from the different Mach numbers obtained in the two legs of the apparatus. This uncertainty fluctuated randomly with each test and is the cause of the variation in the size of the vertical error bars.

The method employed to determine the Mach stem angle from the images obtained attempted to infer the size of the Mach stem angle and its corresponding uncertainty by making a pair of measurements that bracketed the reflection process on the images. This technique provided a variable measure of the error in addition to the changing angle sizes depending on the reflection process and the quality of the image obtained. This error technique also accounted for the accuracy of the angle measurement which changed as the reflection process developed. An image of a more-developed reflection, further down the test section, allowed a more accurate measurement of the Mach stem angle. The results obtained for this arrangement of the apparatus are tabulated below in Table 5.1.

Table 5.1 Measurements from 40° arrangement

Mach	ΔM	Stem Angle	ΔA	Mis-synchronisation
[ ]	[ ]	[°]	[°]	[mm]
1.029	0.0018	0.291	0.004	-0.89
1.032	0.0036	0.612	0.088	-0.89
1.035	0.0055	0.945	0.174	-0.71
1.037	0.0018	0.786	0.163	-0.90
1.041	0.0068	1.209	0.062	-0.18
1.044	0.0081	1.401	0.152	-0.36
1.047	0.0056	1.471	0.147	0.00
1.050	0.0056	1.608	0.156	-0.73
1.053	0.0031	1.821	0.179	0.36
1.061	0.0044	2.558	0.136	-0.73
1.062	0.0044	2.423	0.137	-0.37

5.1.3. Trend lines for extrapolation

To determine the transition Mach number from the data in Table 5.1 trend-lines are fitted to the data. To get an initial idea of the best fit to the data the three types of trend-lines that are options in Microsoft Excel that have intercepts are illustrated below. Power series and logarithmic trend-lines were not included as the extrapolation would have no result, it is an implicit assumption of the technique to infer that the transition occurs at the Mach number indicated by an extrapolation to zero stem-angle, that the data extrapolate to an intercept of value greater than Mach 1. Figure 5.3 shows the abovementioned variety of trend-lines with the experimental data.

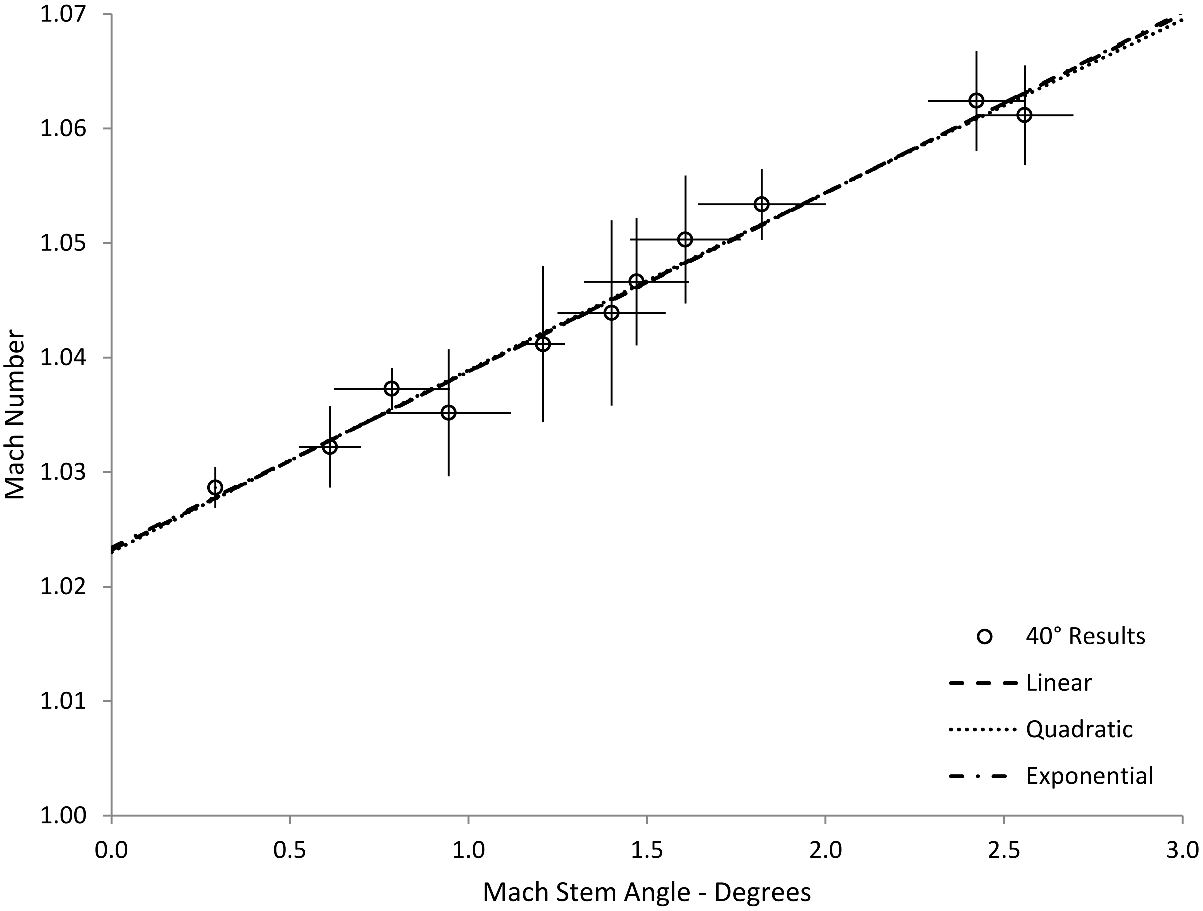

Figure 5.3 Trend lines on 40 degree data

The three trend-lines in Figure 5.3 show very similar behaviour. Their equations and their accompanying co-efficients of determination are given in the table below, where M is Mach number and χ is Mach stem angle:

Table 5.2 Trend-line equations and sum of squares of their residuals

Type	Equation	SS
Linear	$M = 0.0156\,\chi + 1.0232$	2.744E-05
Quadratic	$M = -0.0002\,\chi^2 + 0.0161\,\chi + 1.0230$	2.742E-05
Exponential	$M = 1.0234e^{0.0149\chi}$	2.761E-05

The intercepts of the equations with the vertical axis give the implied transition values. All the curves agree on a transition Mach number of 1.023, considering that the error in Mach determination for a data point typically allows for confidence in quoting to the second decimal place.

The sum of squares of the residuals shows that the linear and quadratic trend-lines have the best fit to the data, with the quadratic curve very slightly more accurate. The quadratic curve is virtually linear, implied by the small value of the co-efficient to the quadratic term, similarly the small co-efficient to χ in the exponential equation yields near-linear behaviour in the range of the experimental data.

The linear and quadratic functions are selected for further investigation and their residuals with respect to the experimental data points are illustrated in Figure 5.4.

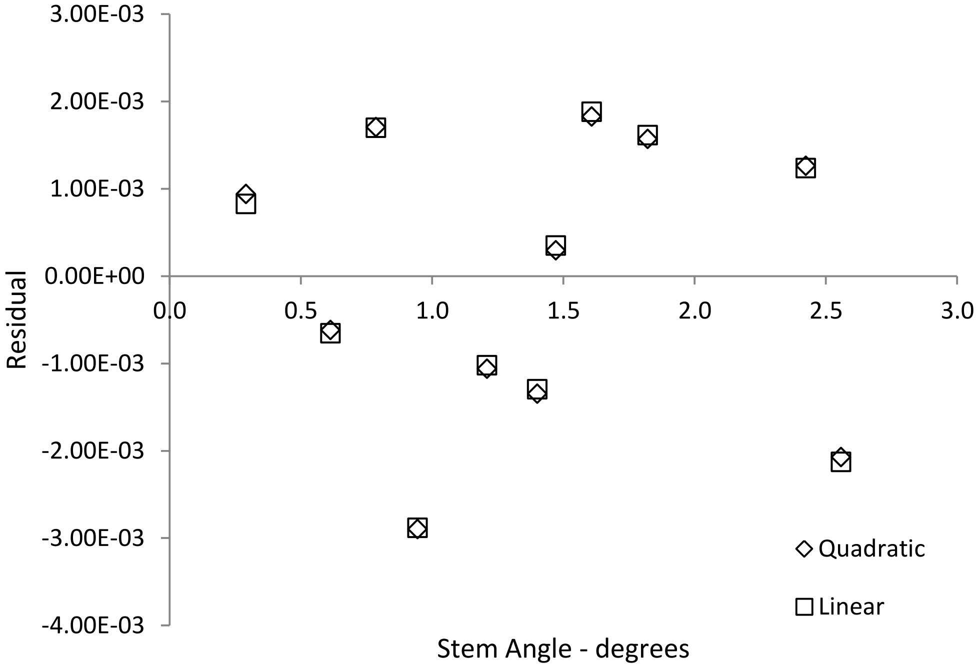

Figure 5.4 Quadratic and Linear trend line residuals

Figure 5.4 shows the residuals of the data scattered randomly about the horizontal axis, implying that the trend line is a polynomial of the correct order.

5.1.4. Iterative curve fits and 95% confidence intervals

The same data were input to Matlab's curve fitting function, *nlinfit* and its statistical confidence limit calculating co-functions *nlpredci* and *nlparci* to maximise accuracy of the fitted curve. The Matlab function solves for an optimum co-efficient set to fit a trend-line function of any type to a set of data. The details of the Matlab code and functions used, with a matrix of alterations for the various different manifestations, are included in appendix D.

The linear and quadratic trend-lines fitted to the data by the Matlab function are shown below, bracketed by their 95% confidence intervals:

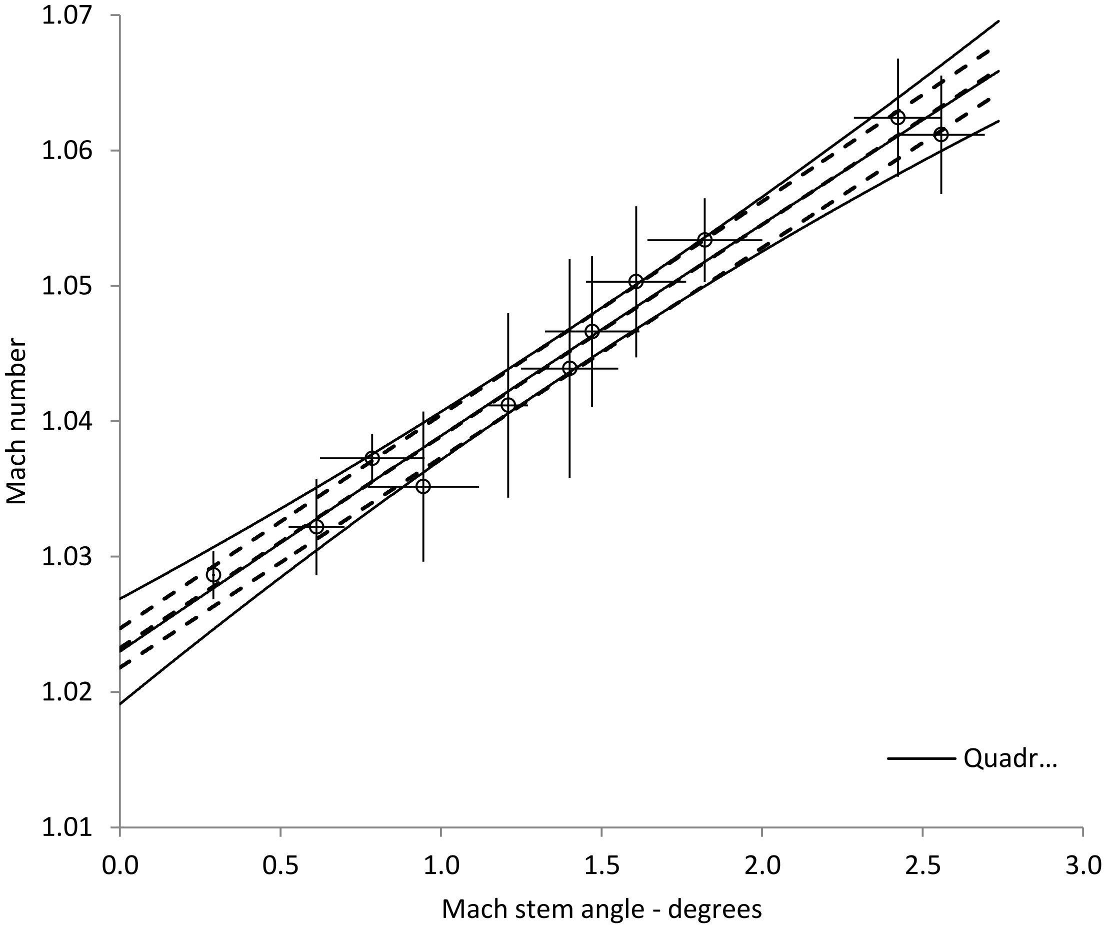

Figure 5.5 Quadratic and linear Matlab trends with 95% confidence intervals

From the figure it is apparent that the trend-lines are not much altered from their predecessors generated by Excel. The confidence intervals from the Matlab function echo the fitted functions and it can be seen that the confidence intervals associated with the quadratic curve fit include more of the data points than those of the linear curve fit. The quadratic confidence interval curves also diverge where the trend line is extrapolated beyond the data, which seems to be sensible, intuitively.

The new trend-lines both have lower sum of squares errors and slightly altered values, indicating a change in the predicted intercept of the trend line with the vertical axis, and hence the transition from regular to Mach reflection. The equations of the linear and quadratic trend lines illustrated in Figure 5.5 are given below in Table 5.3:

Table 5.3 Matlab trend-line equations (simple curve fit)

Type	Equation	SS
Linear	$M = 0.0156\chi + 1.0233$	2.734E-05
Quadratic	$M = -0.0001\chi^2 + 0.0160\chi + 1.0231$	2.729E-05

5.1.5. Robust curve fitting

The distinction between the linear and quadratic fits using the Matlab curve fit function is more apparent, demonstrating that the quadratic curve is to be preferred. This echoes the findings of Barbosa (3), who found that a quadratic curve was the most accurate fit to his data.

There is a further option available using the Matlab curve-fitting functions, that of ‘Robust’ curve fitting. ‘Simple’ curve fitting gives each data point an equal weight in determining the equation of the trend-line, with the result that the end-data points can influence the direction of the curve significantly and that statistical outliers have an equal impact of the trend-line and hence the extrapolation as the points that are not scattered.

‘Robust’ curve fitting uses the initial equation of the trend-line to determine the residuals of each of the data points. Each data point is then allocated a weighting based on the residual and the weightings are used to iteratively solve for the best fit to the data. Robust curve fitting is better than the simple least-squares approach at accurately determining a trend line through scattered data. The equations of the curve fits shown in Figure 5.6 using the ‘robust’ curve fitting in Matlab are included below, along with the equations of the confidence limits that bracket the quadratic fit to the data.

Table 5.4 Robust linear and quadratic trend-lines

Type	Equation	SS
Linear	$M = 0.0156\ \chi + 1.0233$	2.734E-05
Quadratic	$M = -0.0002\ \chi^2 + 0.0166\ \chi + 1.0230$	2.727E-05

The linear equation is unchanged by the robust data fit, although its 95% confidence limits are broader and include more of the data points. The quadratic equation sum of squares error is now significantly lower than the linear equation, marking it the preferred fit to the data.

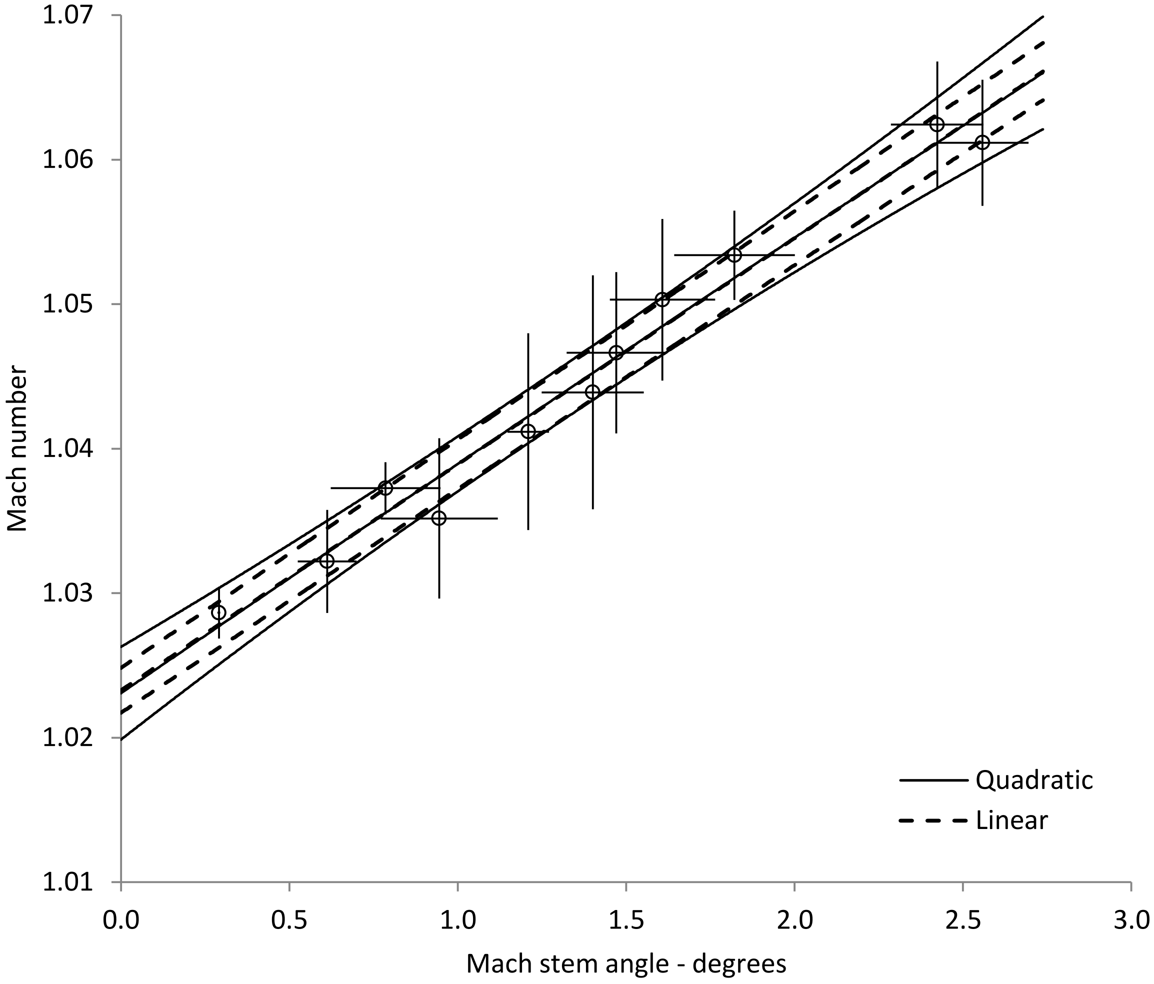

Figure 5.6 Robust trend lines fitted to 40° data

5.1.6. Multivariate analysis

Similarly to Barbosa's (3) study, a multivariate quadratic trend-line was fitted to the data to eliminate the effect of the mis-synchronisation. This is a further extension to the use of the *nlinfit* tool, which finds the optimum suite of co-efficients for any n-dimensional function plotted to a given data set. The equation of the new trend-line is given below, where ψ is a variable representative of the mis-synchronisation.

$$M = -0.0002\,\chi^2 + 0.0166\,\chi + 0.0047\psi^2 + 0.0034\psi + 1.0223$$

The sum of squares for the function, based on the measured angle and mis-synchronisation inputs, is 2.2264E-5, a significant reduction over the value associated with the single-variable quadratic fit to the data. The multivariate analysis also has an impact on the confidence limits, illustrating in the figure that follows that all of the data points are included within the 95% certainty, giving credence to their limits on the extrapolation. An additional support of the accuracy of the multivariate extrapolation comes from the observation that all of the data points have at least one error bar that crosses the central trend-line.

The trend that is plotted below is the above function with the mis-synchronisation variables set to zero.

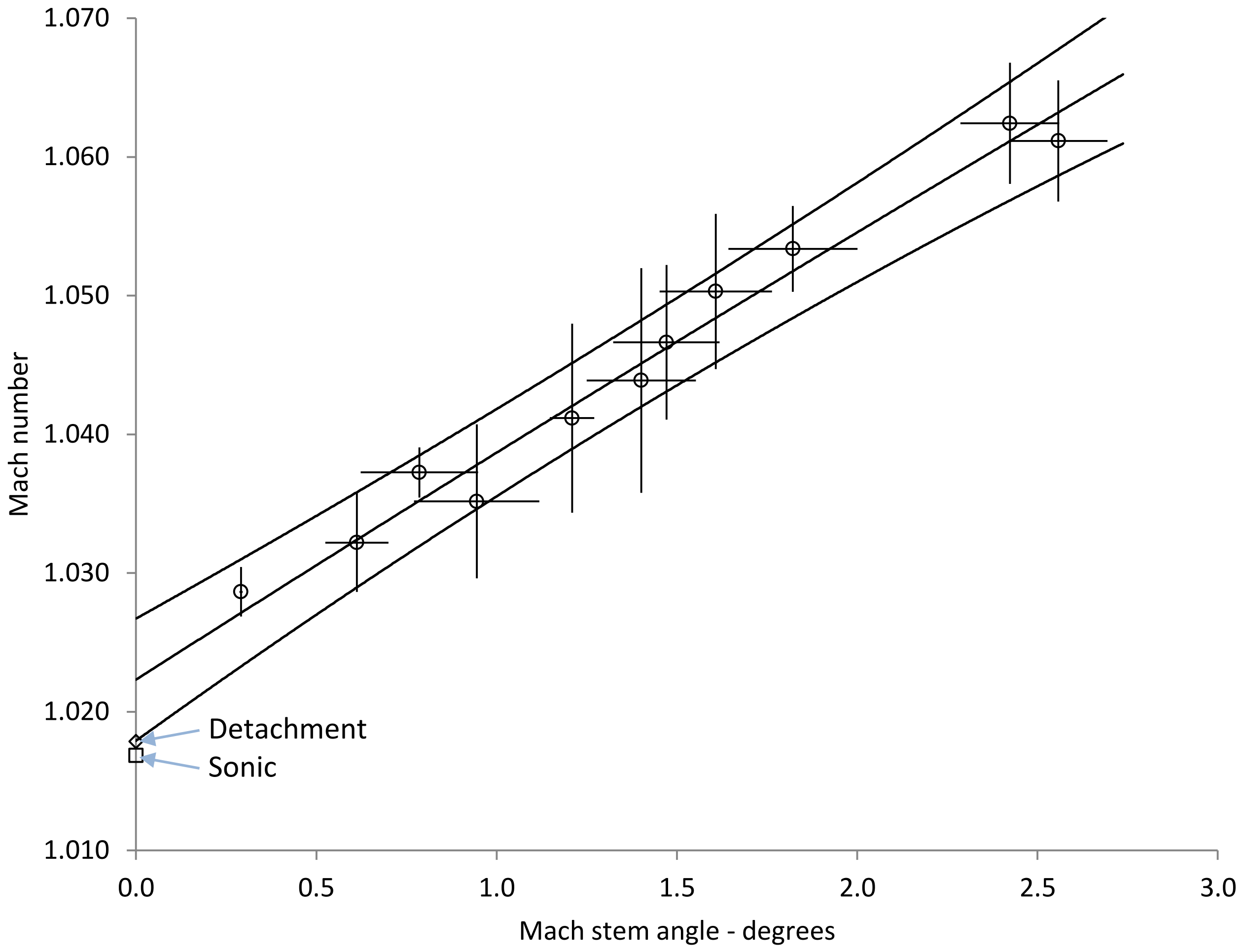

Figure 5.7 Multivariate quadratic trend line with theoretical transition values

The values of transition calculated from the sonic and detachment criteria are plotted on the vertical axis of the above figure. Figure 5.7 indicates an experimentally-extrapolated transition from regular to Mach reflection at a Mach number of 1.0223 with 95% confidence between 1.0179 and 1.0267.

The extrapolation indicates a persistence of regular reflection of ΔM = 0.0045. When it is noted that the average uncertainty in Mach number for the data used to carry out the extrapolation is 0.0046, the persistence indicated is put in some perspective.

5.2.96° bifurcated section, 48° wedge

The design and manufacture of a bifurcated section that is representative of a 48° wedge is a carefully chosen compromise. It is in a range where Mach reflection is just possible (Figure 3.4 indicates that Mach reflection is theoretically impossible beyond a wedge angle of approximately 50° and is often only experimentally observed below approximately 48°), but it is close to the asymptote in the theoretical transition Mach numbers predicted by the sonic and detachment criteria. This is the part of the experimental space where the theoretical transition values predicted by the two criteria are separated by their greatest margin, allowing the experimental transition value to indicate which criterion accurately predicts the transition from regular to Mach reflection in addition to determining whether the theoretically predicted transition value is correct for the inviscid, adiabatic case.

5.2.1. Typical result features

The typical features of a well-synchronised image from the 96° arrangement of the apparatus is shown below. This arrangement provides a method to study the effects, in a two dimensional representation, of a planar shock wave encountering a wedge inclined at 48° to its path.

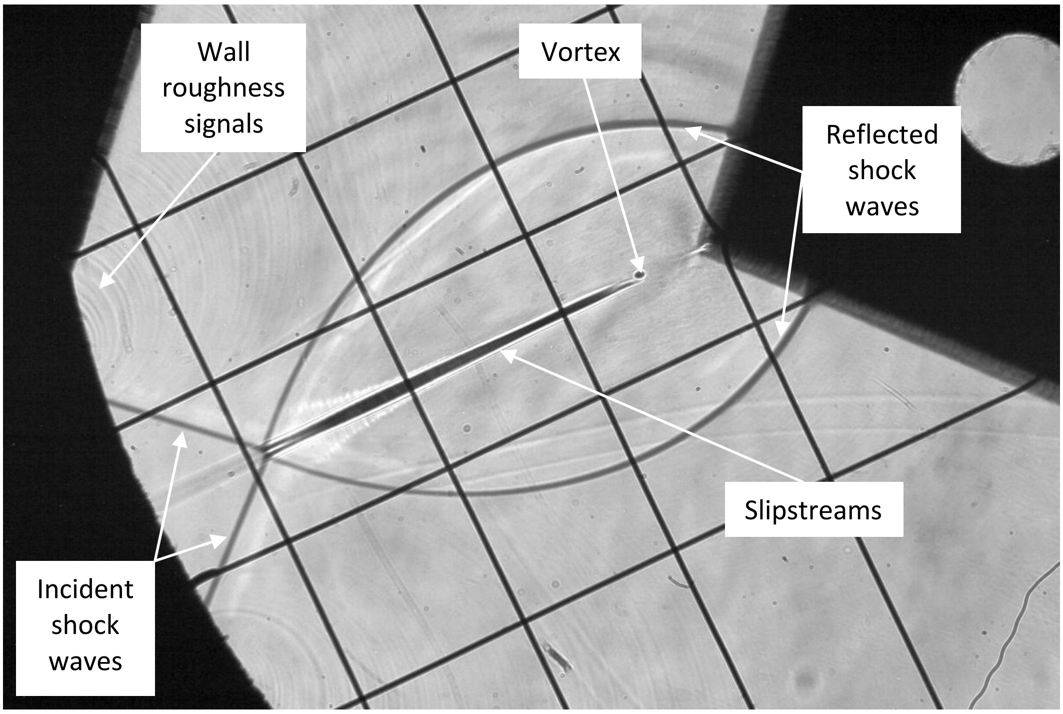

Figure 5.8 Typical image obtained from 96° bifurcated section

(Test 195, Ms = 1.56, stem angle = 0.47°, mis-synchronisation = 0.00mm)

Figure 5.8 shows a typical result image, albeit at the highest Mach number at which a well-synchronised image was obtained. This image most clearly illustrates the features typical of a shadowgraph image captured for this orientation of the bifurcated section.

There are some notable differences between the shadowgraph images for the steeper angle. There are a series of circular signals originating from the incident shock waves' interaction with the walls of the shock tube and the window. The slipstreams are very pronounced, they are the starkest features of the interaction, and appears to contract and then expand and contract again before terminating in a small vortex near the wedge. The edges of the wedge and the outer walls of the test section appear to be blurred.

The signals originating from the incident waves are sharply defined but not particularly bright and are assumed to be sonic waves generated by the passage of the shock over the slight roughness on the surface of the test section from the machining process.

The apparent expansion and contraction of the slip-stream is probably due to diffraction of light from the reflection, which can also be seen on the edges of the wedge.

The apparent continuation of the slipstream further down the test section, than the incident waves, may be due to a lingering glow from the light source illuminating the reflection process as it proceeded down the test section. Bright light diffracted inward from the reflected waves, apparent as a light band between the reflected shocks, makes the slipstream appear to contract after the interaction. It is assumed that diffraction also leads to the blurring of the walls and the edges of the wedge.

The vortex at the apex of the slipstream is very weak and is due to a slight mis-synchronisation of the waves, in spite of the calculated zero mis-synchronisation for this image. The mis-synchronisation is calculated upstream of wedge and extrapolated, which is subject to error. Although the vortex appears in this image to be significant, its evidence in the image is largely due to the strong shock waves to generate Mach reflection interactions at a wedge angle of 48°. A vortex has a strong density gradient and hence appears clearly in the shadowgraph image.

5.2.2. 96° results

A plot of the data from the 96° arrangement shows that the data is more scattered than that of the 40° case.

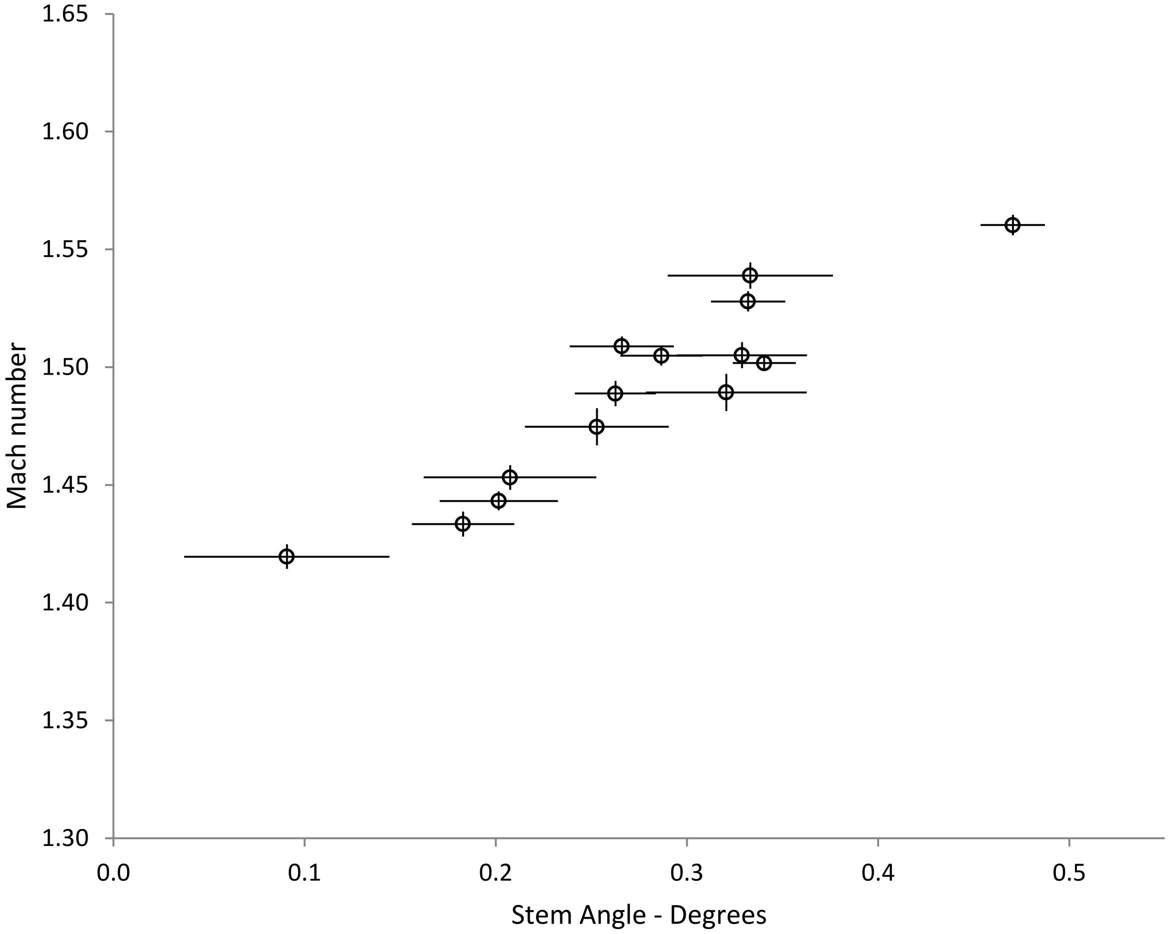

Figure 5.9 Plot of results from the 96° tests.

Relative to the 40° data points two features are immediately apparent in the results for the 96° arrangement. The Mach numbers of the tests are much greater as they are in the region of the transition value for this wedge angle. The transition is near the asymptote in the relationship between wedge angle and transition Mach number, and the measured Mach stem angles are proportionally smaller than the Mach numbers. The entire domain of stem angles for the 96°

results fits within the first interval of the corresponding plot for the results of the 40° bifurcated section, whereas the entire Mach range of the latter would fit into two of the intervals of the former's plot.

One result of the small angles and large Mach numbers is that the dominant source of error, apparent in the figure, is the angle measurement which is at the limit of that resolvable with the current optical set up. A table of all 14 results of sufficient clarity and mis-synchronisation less than one millimetre for the 96° arrangement are tabulated below:

Table 5.5 Measurements from experiments on 96° arrangement

Mach	ΔM	Stem Angle	ΔA	Mis-synchronisation
[ ]	[ ]	[°]	[°]	[mm]
1.420	0.0052	0.091	0.054	0.32
1.433	0.0053	0.183	0.027	0.18
1.443	0.0040	0.202	0.031	0.25
1.453	0.0053	0.207	0.045	-0.45
1.475	0.0079	0.253	0.038	-0.81
1.489	0.0054	0.263	0.021	-0.67
1.489	0.0078	0.321	0.042	-0.59
1.502	0.0029	0.340	0.017	0.52
1.505	0.0042	0.287	0.022	-0.30
1.505	0.0055	0.329	0.034	-0.52
1.509	0.0042	0.266	0.027	-0.52
1.528	0.0043	0.332	0.019	-0.29
1.539	0.0056	0.333	0.043	-0.12
1.560	0.0044	0.470	0.017	0.00

5.2.3. Trend lines for extrapolation

Similarly to the 40° arrangement a variety of types of viable trend-line were fitted to the data and are illustrated below:

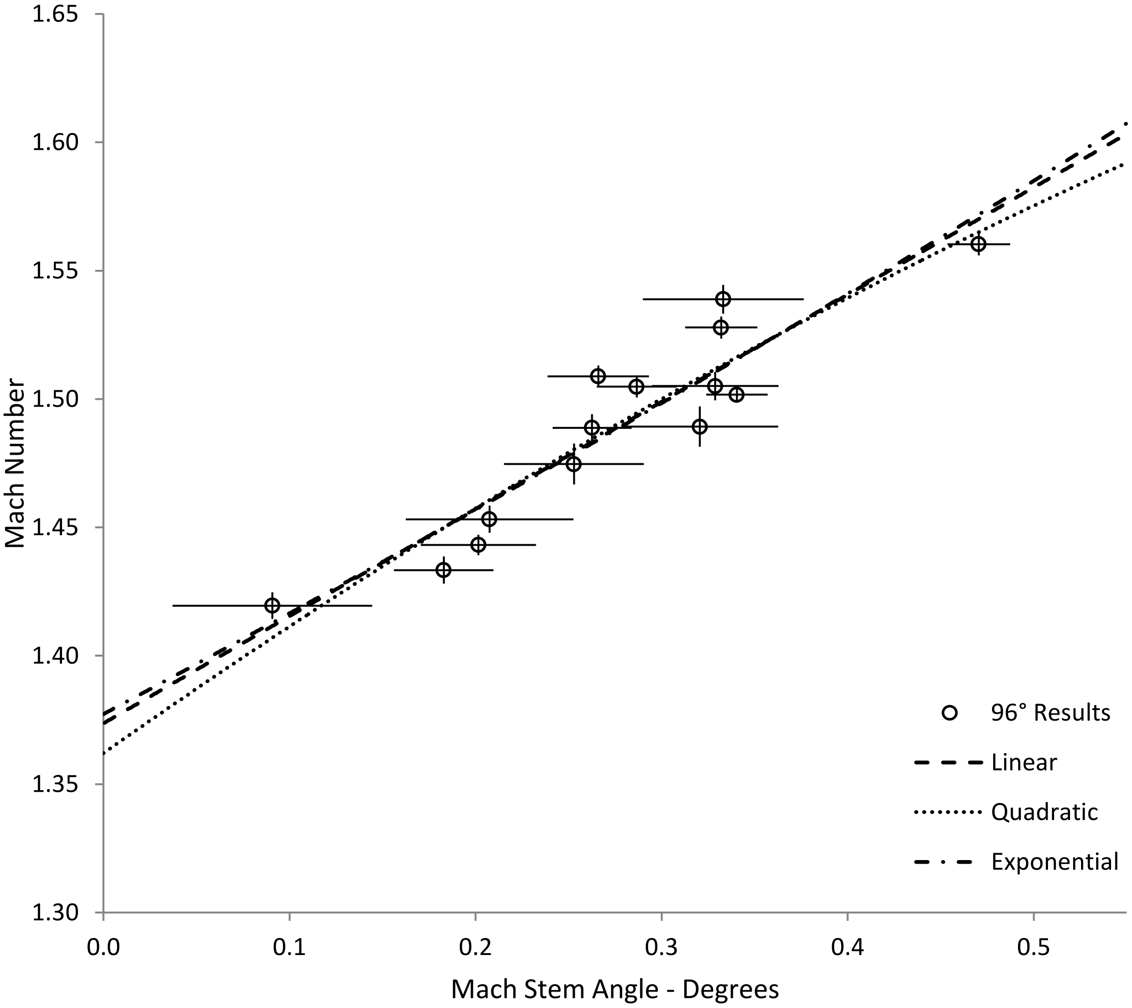

Figure 5.10 96 degree data with basic trend lines

Figure 5.10 clearly illustrates that the trend lines of different types vary significantly in their shape and hence implied transition point. This is borne out by their equations tabulated below:

Table 5.6 Basic trend-line equation fits to 96degree data

Type	Equation	SS
Linear	$M = 0.4174\,\chi + 1.3737$	2.9625E-03
Quadratic	$M = -0.1672\,\chi^2 + 0.5100\,\chi + 1.3621$	2.9076E-03
Exponential	$M = 1.3773e^{0.2809\chi}$	3.0092E-03

From comparison of the sum of squares errors for each of the different trend-lines it is apparent that the data are significantly scattered and that the quadratic trend the best fit to the data.

5.2.4. 'Simple' and 'robust' curve fits

Using the above quadratic curve as a starting point the Matlab function *nlinfit* is used to generate a pair of curves using both the 'simple' and 'robust' curve fitting approaches. The equations of the curves and their residual-errors are summarised in the following table:

Table 5.7 Simple and robust curve fits to 96° data

Type	Equation	SS
Simple	$M = -0.1672\,\chi^2 + 0.5100\,\chi + 1.3621$	2.9076E-03
Robust	$M = -0.1744\,\chi^2 + 0.5149\,\chi + 1.3611$	2.9091E-03

From Table 5.7 it is evident that the simple quadratic curve is unchanged. It is included, however, as the Matlab function *nlpredci* fits confidence intervals to the measured values which are useful to bracket the trend-line and imply an error for the extrapolation point. Interestingly the ‘robust’ fit to the data shows a greater sum of squares error, but this is not significant and the difference between the equations is not marked, as is illustrated in the following figure.

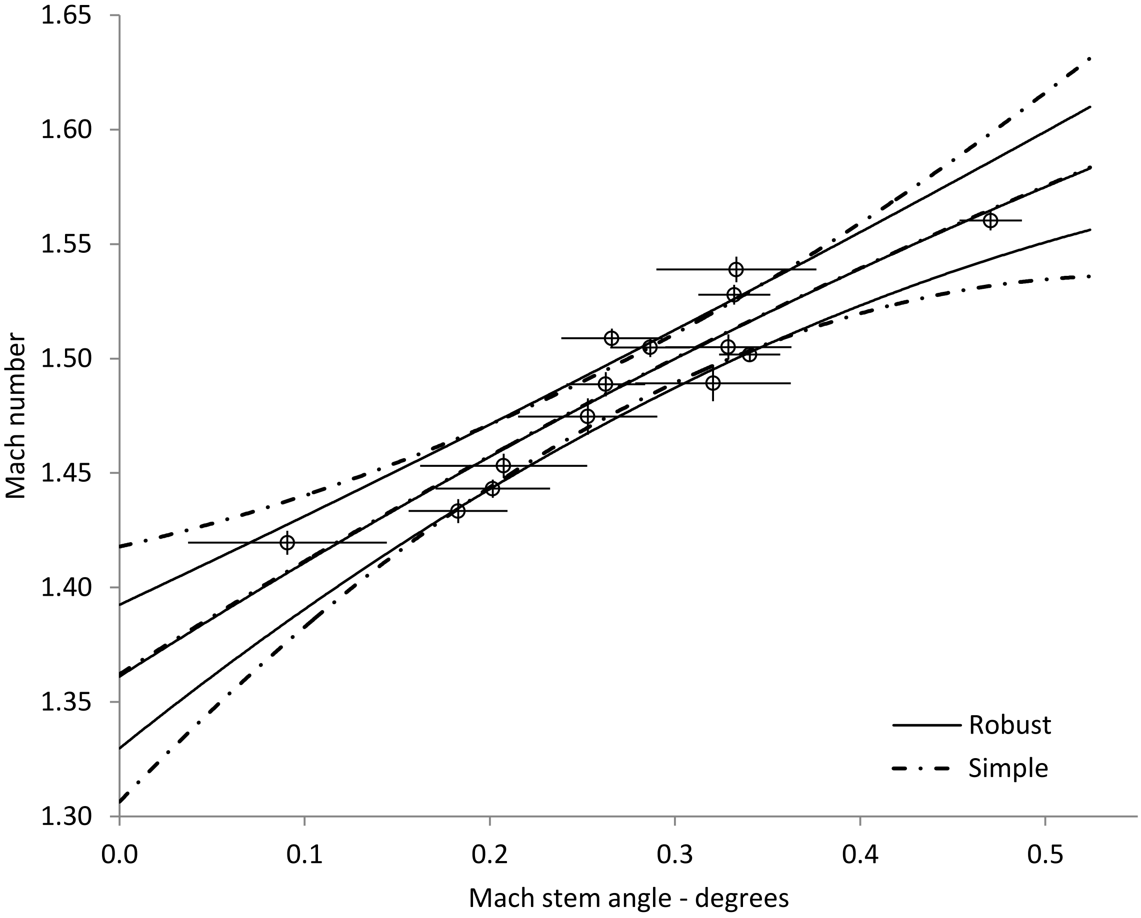

Figure 5.11 Robust and simple trend-lines and confidence intervals

Both of the above trend-lines and their confidence limits are illustrated with the 96° data. The difference between the ‘robust’ and simple data fits is marked in their corresponding 95% confidence intervals with the ‘robust’ confidence intervals showing comparatively smaller curvature. The smaller curvature results in a tighter range of Mach numbers for the predicted transition point.

The data for the 96° bifurcated section shows significant scatter, with half of the data points falling outside the confidence intervals for both types of quadratic data fit. This is largely due to the large uncertainty in the angle measurements.

5.2.5. Multivariate analysis

Again the influence of the slight mis-synchronisation has a marked effect on the accuracy of the data fit. When a multivariate quadratic curve is fitted to the data the following equation is found for the Mach number (M) in terms of the stem-angle (χ) and the mis-synchronisation (ψ):

$$M = -0.1503\,\chi^2 + 0.4838\,\chi - 0.0427\,\psi^2 - 0.0197\,\psi + 1.3724$$

The sum of squares of the residuals for the above equation is 2.332E-03, showing that the above equation is a more accurate fit to the data than the single variable fit and confirming that the mis-synchronisation alters the measured stem angle. The above equation, with the effect of mis-synchronisation suppressed, is plotted with its 95% confidence intervals in the following figure. Also plotted are the Mach numbers for transition at this wedge angle predicted by the sonic and detachment criteria, 1.3760 and 1.4022 respectively.

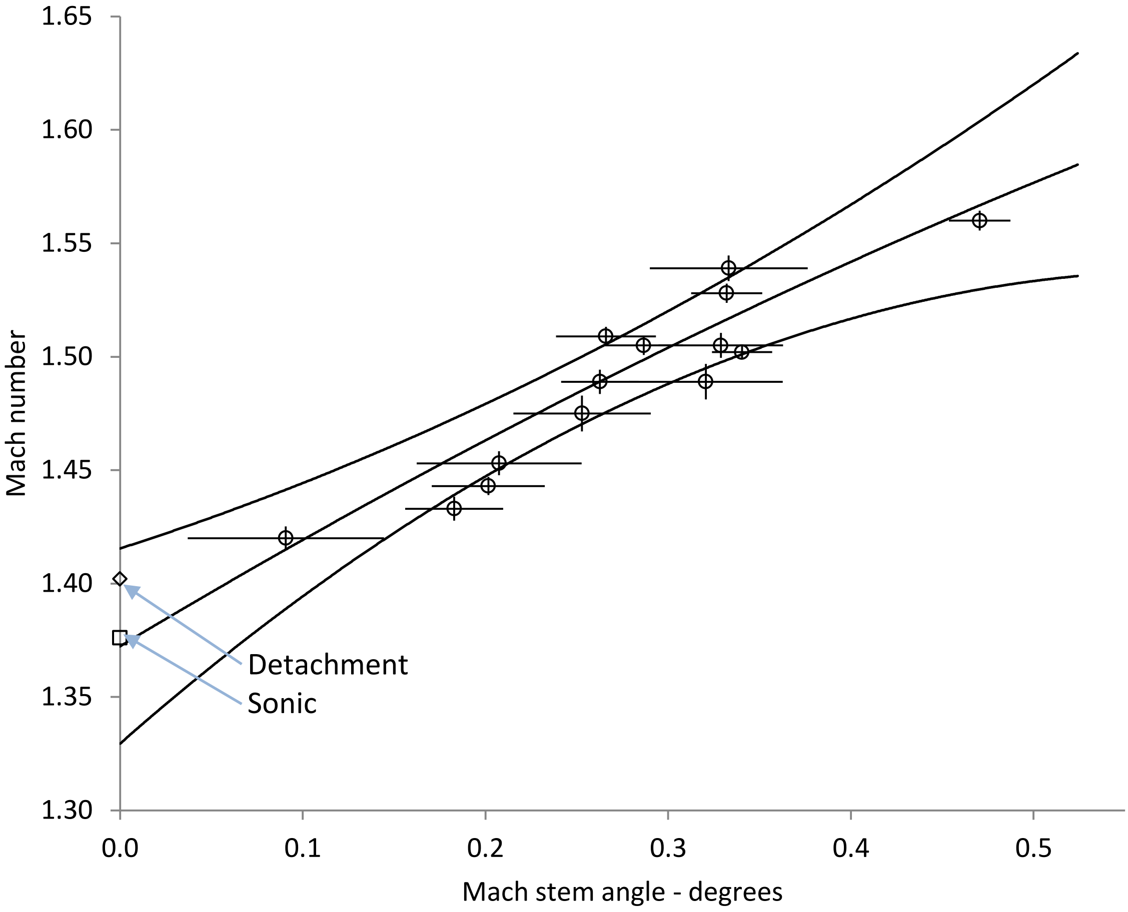

Figure 5.12 Multivariate trend-line and confidence intervals on 96° data

The confidence intervals indicated on Figure 5.12 bracket a Mach range that is a compromise between that of the ‘simple’ and ‘robust’ simple trend-lines. They do not include more than half of the measured data points, although they border on the excluded points, indicating that their 95% confidence range is not an accurate indication of the range of certainty of the extrapolation and points beyond their limits on the vertical axis may be included as the statistical limits of probability of the location of the transition Mach number.

The fitted curve, corrected both for scattered data and the effect of mis-synchronisation, intersects the vertical axis almost directly on the theoretical transition value predicted by the sonic criterion. The experimentally-extrapolated value of 1.3724 differs by just 0.0036, which is smaller than the average uncertainty of Mach number measurement of 0.0051. By this distinction the extrapolation implies that transition occurs at the value implied by the sonic criterion and not the detachment value.

This is contrary to the findings of (Barbosa & Skews, 2002), who found the extrapolation of his data indicated that the transition occurred on the value predicted by the detachment criterion, with the sonic criterion's value within the bracket of his 95% confidence intervals. In the results of the 96° bifurcated arrangement (48° wedge) the transition values predicted by the sonic and detachment criteria are separated by a margin of 0.026, whereas in Barbosa's 80° (40° wedge) study they were separated by 0.007. This is illustrative of the divergence in the predicted values of transition when both the sonic and detachment criteria become asymptotic. In support of Barbosa's finding is the significantly smaller scattering of his data, with all of his data points within the 95% confidence intervals and with an error bar crossing the extrapolation trend-line.

As an *ad hoc* estimate of the uncertainty in the extrapolated curve the major source of error, the angle uncertainty, can be translated from the horizontal to the vertical by taking the average angle uncertainty and dividing it by the gradient of the curve at the vertical axis to translate its' effect to a vertical uncertainty. From an average horizontal uncertainty of 0.127° and a gradient of 0.4838 an uncertainty in the extrapolated Mach number as a result of the uncertainty of the angle measurements of 0.06 can be implied. This is significant because it is larger than the difference between the extrapolated transition value and the detachment criterion.

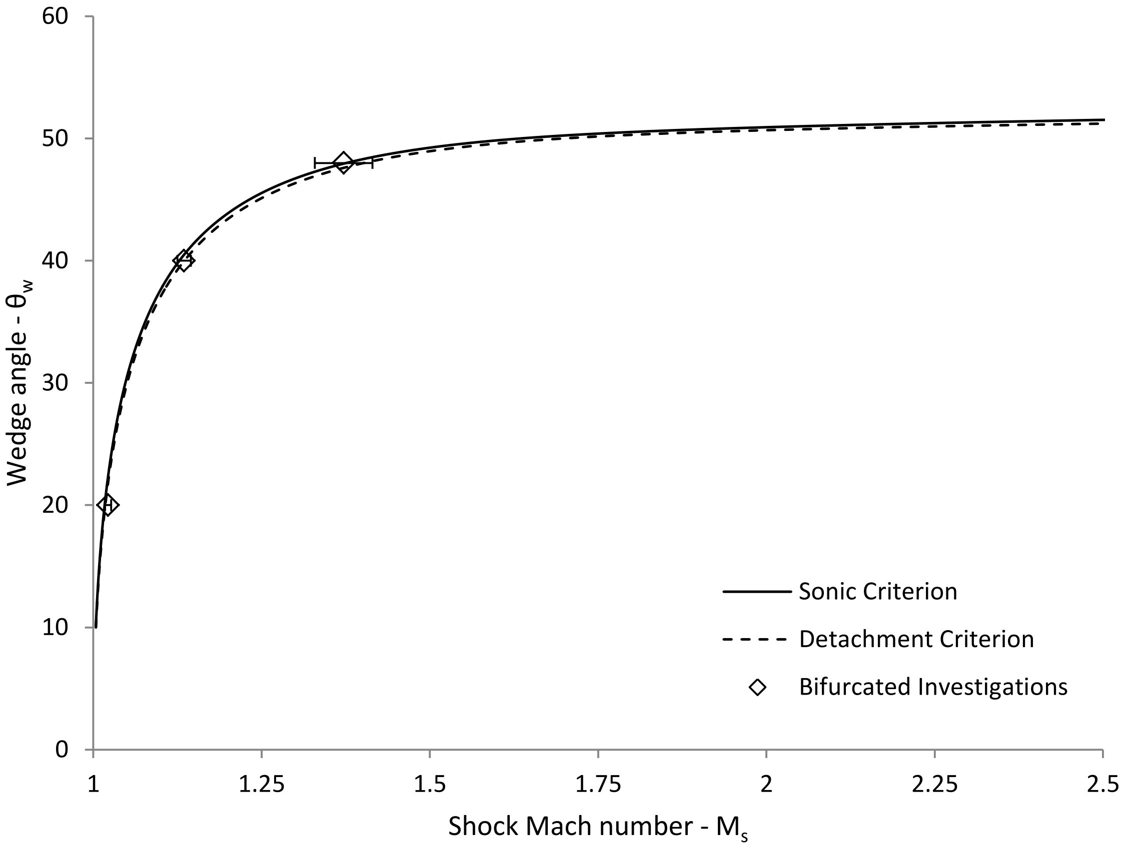

Figure 5.13 Results from all investigations on bifurcated shock tubes

Figure 5.13 is a summary of all of the transition values experimentally investigated using the bifurcated shock tube apparatus superimposed on the transition values calculated from the sonic and detachment criteria.

The error bounds on the experimental data points illustrate the limits of the 95% confidence intervals on the trend-lines used to conduct the extrapolation to the transition value.

While the results from the 40° orientation of the bifurcated section indicate a persistence of regular reflection, they are within their experimental uncertainty of the transition value which is significantly lower than the amount of persistence typically observed, as can be seen in Figure 3.8. The findings are within the average error in Mach number of the transition point and the lower

95% confidence interval agrees with the detachment value within experimental accuracy.

The 96° bifurcated section indicates transition exactly on the theoretical sonic value, however it suffers from a large margin of uncertainty. The uncertainty is due to the very small angles measured in the interaction and is illustrated by the scatter in the results obtained. The 95% confidence intervals encompass the detachment criterion value as well.

6. Conclusions

An investigation into the cause of the persistence of regular reflection was carried out using a bifurcated shock tube of two orientations, 40° and 96°. These two orientations allowed the transition from regular to Mach reflection on wedge angles of 20° and 48° to be determined by extrapolating images of Mach reflection at a range of Mach numbers to zero stem angle and thus infer the transition Mach number.

In order to conduct the investigation on the 20° wedge a driver capable of generating lower Mach number shock waves had to be assembled. A pressure vessel was located and parts were manufactured that enabled a simple driver to generate shock waves of sufficient weakness, the weakest of which that resulted in a synchronised reflection had a Mach number of 1.029 at the test section.

Shadowgraph images of synchronous, equal strength shock wave reflections were obtained using the 40° orientation of the bifurcated shock tube at Mach numbers near the transition point. These images were measured and it was found that a quadratic relationship was the best fit to the resulting Mach number vs. stem-angle trend. This quadratic relationship’s accuracy was increased by using an iterative curve fitting technique, and the residuals between the fitted curve and the data were further reduced by multivariate curve fit that accounted for slight mis-synchronisation between the shock waves incident in the test section of the bifurcated shock tube.

The results obtained from the 40° section implied that a slight persistence of regular reflection on a 20° wedge was observed, but that the persistence was slight and within experimental accuracy of the theoretical transition point. The 95% confidence intervals on the data obtained indicated the narrowest region of transition Mach numbers for an investigation conducted with a bifurcated shock tube. The first objective of the research was satisfied on this arrangement of the apparatus and indicated that no persistence of regular reflection is observed within the experimental accuracy.

In order to conduct the investigation using the 96° orientation of the shock tube a change of driver was necessary, due to the erratic behaviour of the simple driver at the higher Mach numbers in the region of the transition from regular to Mach reflection on a wedge inclined at 48° to the shock wave's path.

The shadowgraph images obtained of mutual reflection of synchronised equal strength shock waves in the test section of the 96° bifurcated section were measured and their corresponding Mach numbers calculated from traces from pressure transducers upstream of the test section. The measurements were quite scattered as a result of the large errors inherent in measurement of very small angles from the images. Again a quadratic trend-line was found to be the best fit to the data and once a multivariate analysis had been performed it was found that the transition Mach number inferred from the trend line ($M_s = 1.372$) fitted to the results was exactly the same as the Mach number calculated from the sonic transition criterion. The first objective of the research was satisfied and the result again indicated that surface viscosity and heat transfer are the cause of the persistence of regular reflection.

Due to the large scatter on the results the 95% confidence intervals fitted to the data also included the detachment criterion with the implication that a distinction indicating the correct transition criterion and hence an identification of the mechanism that causes the transition from regular to Mach reflection cannot be made. Thus the second objective of the research was not met because the transition conditions are very close together and within the error bounds of the experiment. The large margin separating the sonic and detachment criteria however, does infer that the former is the correct mechanism in support of the findings of (Lock & Dewey, 1989).

All of the investigations conducted using a bifurcated shock tube to determine the transition from regular to Mach reflection have indicated no significant persistence of regular reflection. The symmetrical reflection of synchronous equal strength shock waves illustrates, through symmetry, the reflection geometry that results from a shock wave reflecting off a wedge surface that is inviscid, adiabatic and of infinite stiffness. As these properties are the assumptions of the criteria postulated by von Neumann and the observations support the theoretical values within experimental accuracy, the cause of the persistence of regular reflection can be conclusively identified as the difference between investigations on physical wedges that are subject to viscous interaction and heat transfer with the flow and those that are conducted in a bifurcated shock tube, free from these effects. The cause of the von Neumann paradox, the persistence of regular reflection, is viscous and thermal transport phenomena.

7. References

Barbosa, F., & Skews, B. (2002). Experimental confirmation of the von Neumann theory of shock wave reflection transition. *Journal of Fluid Mechanics*, *472*, 263-282.

Ben-Dor, G. (2007). *Handbook of Shock Waves Volume 2*. New York: Springer-Verlag.

Bleakney, W., & Taub, A. H. (1949). Interaction of Shock Waves. *Reviews of Modern Physics*, 584-605.

Henderson, L. F., Crutchfield, W. Y., & Virgona, R. J. (1997). The effects of thermal conductivity and viscosity of argon on shock waves diffracting over rigid ramps. *Journal of Fluid Mechanics1*, *331*, 1-36.

Henderson, L. F., & Lozzi, A. (1975). Experiments on transition of Mach reflexion. *Journal of Fluid Mechanics*, *68*, 139-155.

Hornung, H. G., Oertel, H., & Sandeman, R. J. (1979). Transition to Mach reflexion of shock waves in steady and pseudosteady flow with and without relaxation. *Journal of Fluid Mechanics*, *90*, 541-560.

Hornung, H. G., & Taylor, J. R. (1982). Transition from regular to Mach reflection of shock waves. *Journal of Fluid Mechanics*, *123*, 143-153.

Lock, G. D., & Dewey, J. M. (1989). An experimental investigation of the sonic criterion for transition from regular to Mach reflection of weak shock waves. *Experiments in fluids*, *7*, 289-292.

Netten, A. A. van, Dewey, J. M., & Haimberger, T. von. (1994). The Effects of Surface Temperature on the Shock Wave Reflection Process. *Proc. 11th Mach Reflection Symposium*.

Neuman, J. von. (1943). Oblique reflection of shocks. *Bur. Ord. Explosives Rept.*, *12*.

Skews, B. (1995). Sychronized shock tubes for wave reflection studies. *Rev. Sci. Instrum.*, *66*, 3327-3330.

Smith, L. G. (1945). Photographic Investigations of the Reflection of Plane Shocks in Air. *OSRD*, *6271*.

Smith, W. R. (1959). Mutual Reflection of Two Shock Waves of Arbitrary Strengths. *Phys. Fluids*, 533-541.

Takayama, K., & Sekiguchi, H. (1977). An experiment on Shock Diffraction by Cones. *Rep. Inst. High Speed Mech.*, *36*, 53-74.

Wheeler, J. (1986). An interferometric investigation of teh regular to Mach reflection transistion in pseudostationary flow in air. *UTIAS Technical Note*, *256*.

Zucrow, M., & Hoffman, J. (1976). *Gas Dynamics Volume 1* (pp. 63, 330-337, 359-368). New York: John Wiley and Sons.

8. Appendices

8.1.Appendix A – Calculation of transition Mach number

In the current research the theoretical Mach number of transition from regular to Mach reflection is calculated using a negative feedback iterative loop. Two shock theory is modified in that no calculation is made of the pressures and the calculation of the angle that the second shock wave subtends is replaced with either the sonic or maximum deflection angle, depending on whether the transition value being solved for is for the sonic or detachment criterion.

In the calculation an initial guess of the Mach number is adjusted by an error measurement until the error becomes zero. The error is the difference between the two values of theta calculated by two shock theory, and the loop is iterated until the error becomes zero.

For the theoretical model to be valid for both the Sonic and Detachment criteria the flow is bent towards the surface of the wedge and then back parallel to it, thus the equal angles. When this condition is met the shock wave Mach number used as an input is the Mach number of the transition for either the sonic or detachment criterion, depending on whether the sonic or maximum deflection angle is used.

A flow diagram of the iterative loop is included below, based on Figure 3.7:

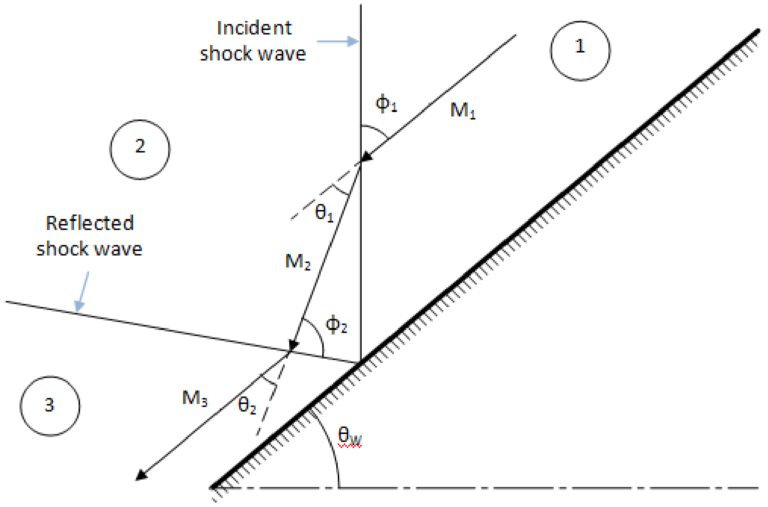

Initial values

$\Delta_M = 0$

θ_W = Chosen value

$\gamma = 1.4$

M_s = Initial guess

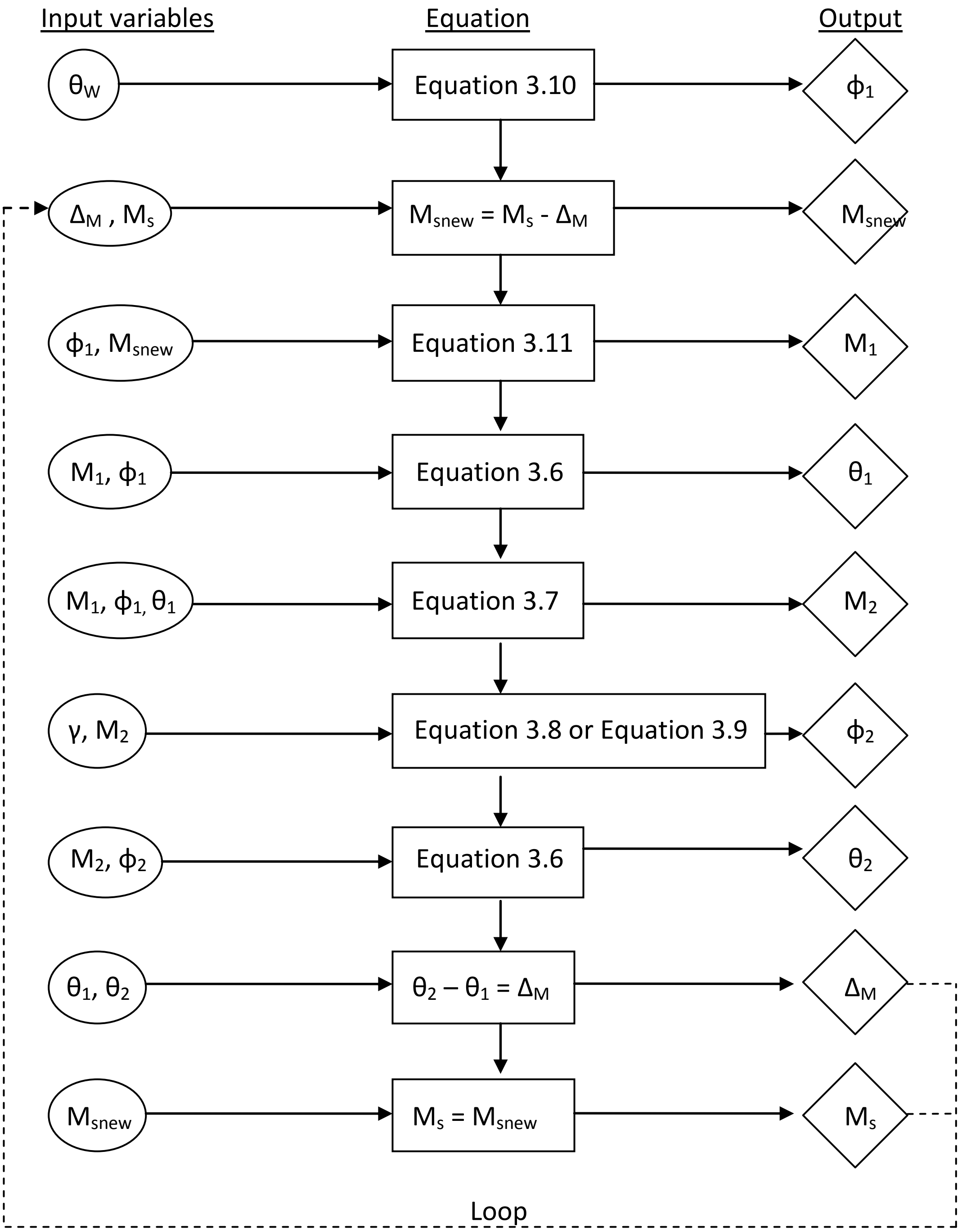

8.2. Appendix B – Manufacturing drawings

8.2.1. Guide rails

The guide rails were manufactured from 50 x 50 x 5 mm angle iron sections that were welded together, with blocks machined from Teflon® bolted to them by recessed M6 bolts.

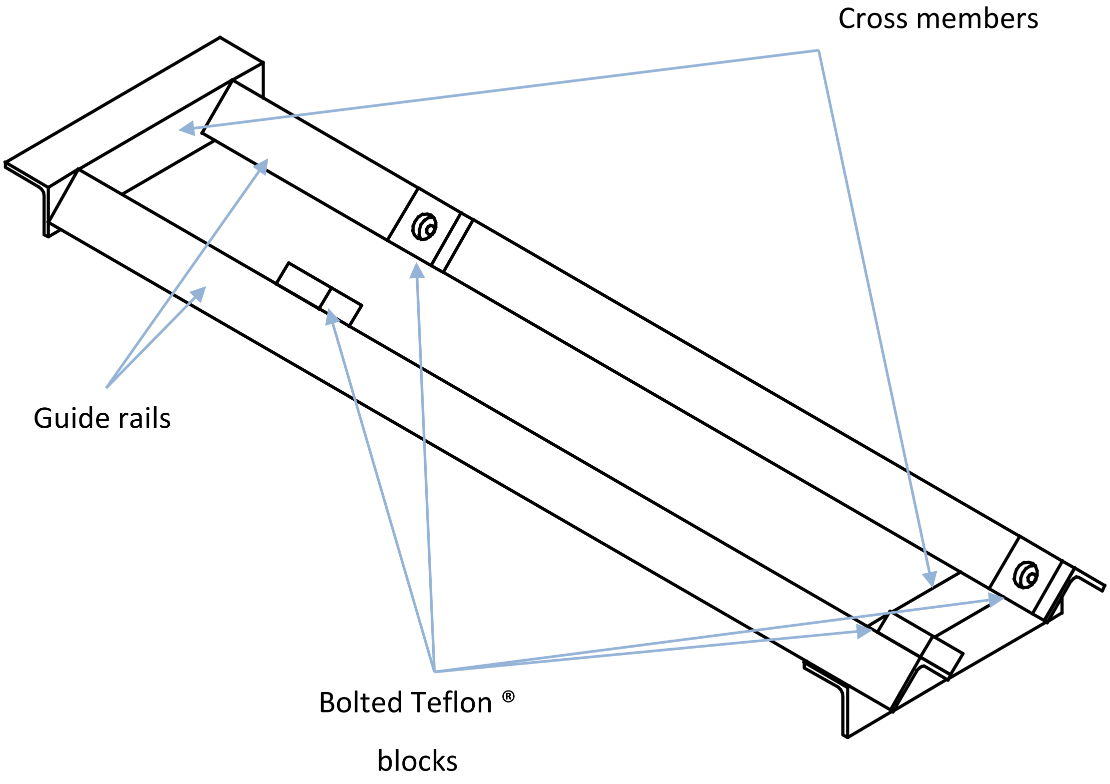

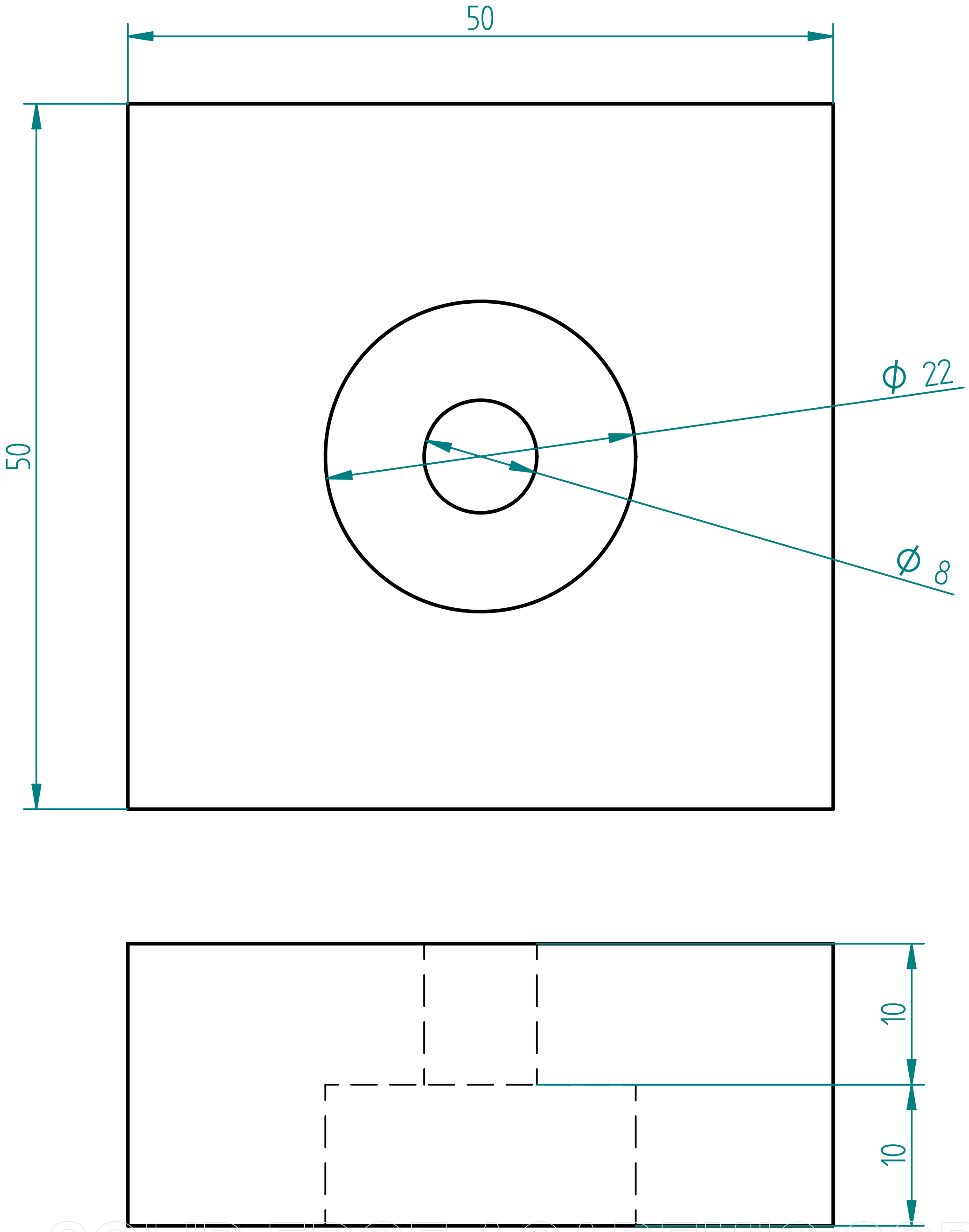

Terence Herron
Student#: 0407950R
Phone: 072 731 7338

Supervisor: Prof Skews

All Dimensions are in mm

Teflon Blocks

4 Blocks are required

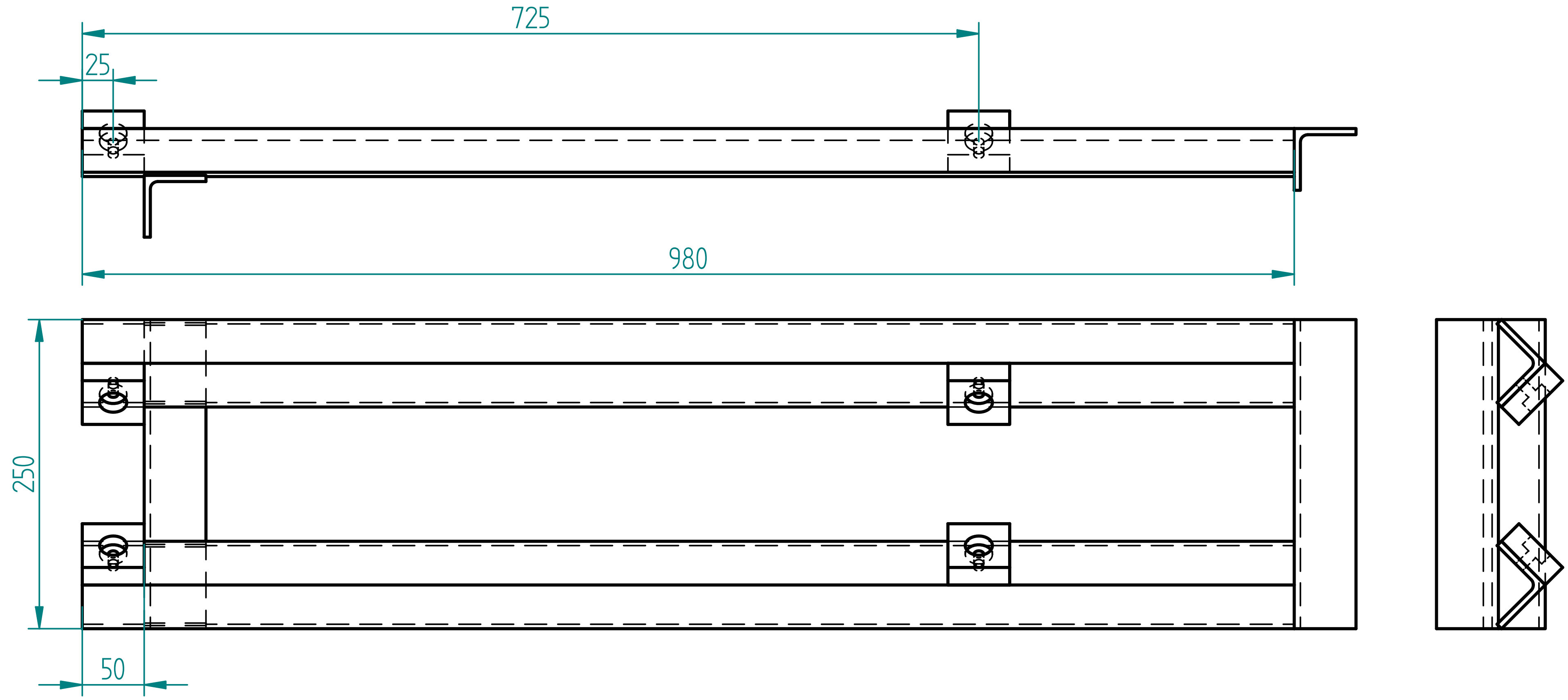

Terence Herron
Student#: 0407950R
Phone: 072 731 7338

Supervisor: Prof Skews

All Dimensions are in mm

Assembly of support for pressure vessel

8.2.2. Adapter flange and securing ring

The adapter flange's rough shape was water-jet cut from 44mm plate. The guide vanes were welded in place later and the threaded holes drilled and tapped. The securing rings were water-jet cut from 5mm plate and were placed on the machined face (reverse of shown) and the reverse-side of the flange at the end of the straight-section.

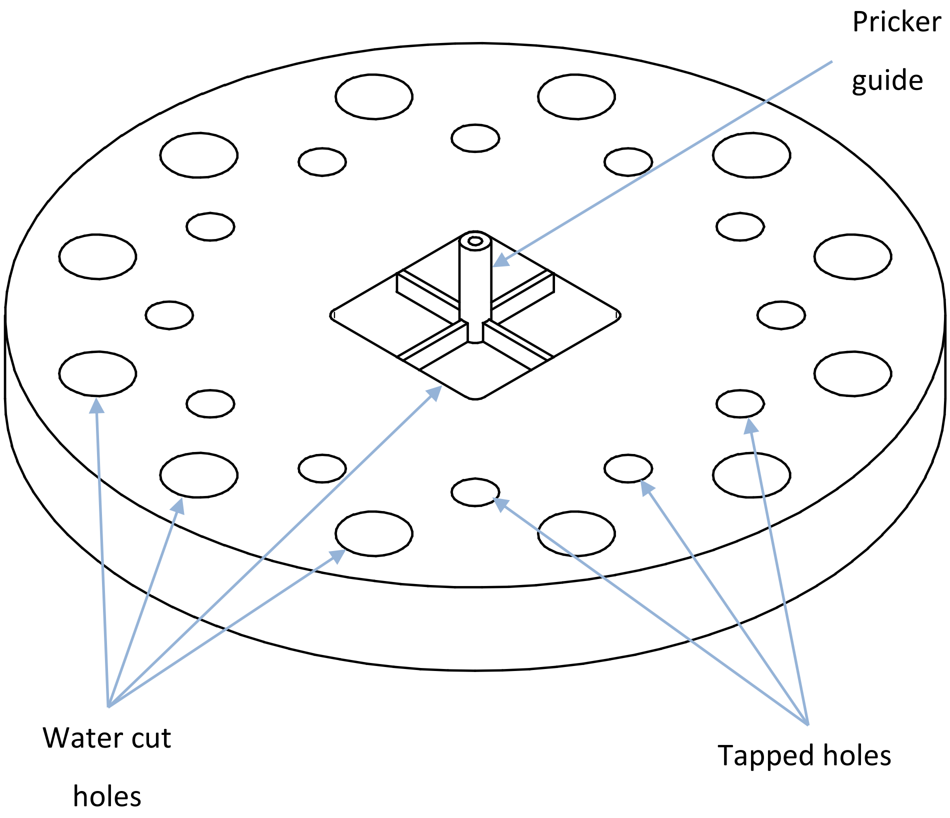

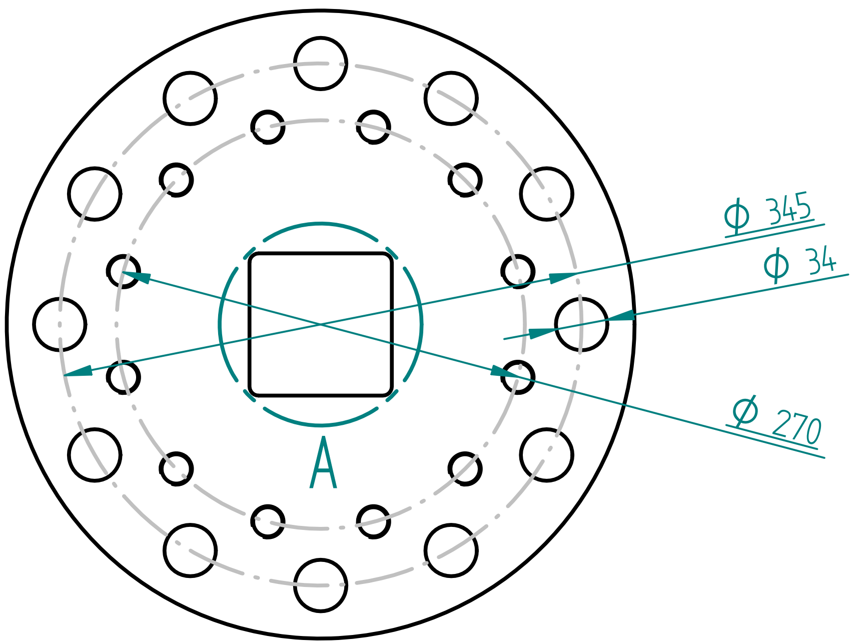

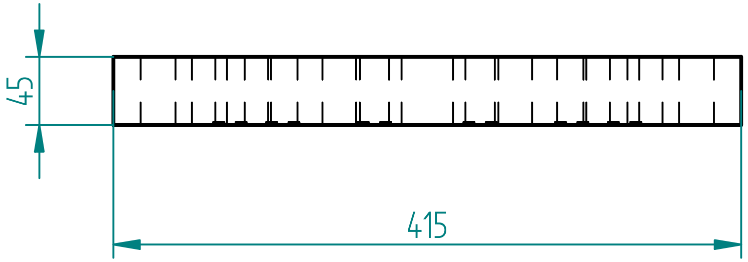

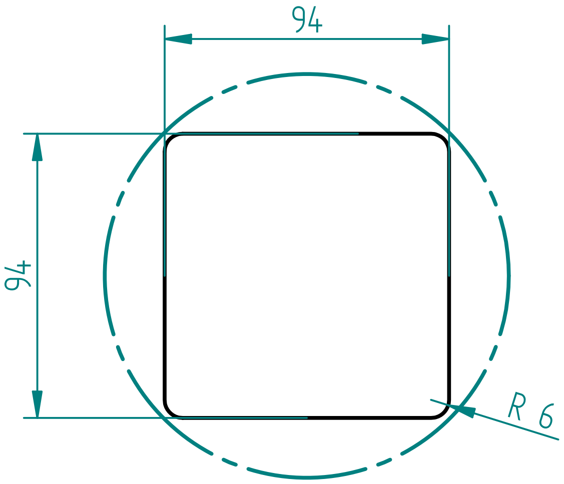

DETAIL A

Terence Herron
Student#: 0407950R
Phone: 072 731 7338

Supervisor: Prof Skews

All Dimensions are in mm

Adapter flange

Inner ring of holes are M22 threaded holes

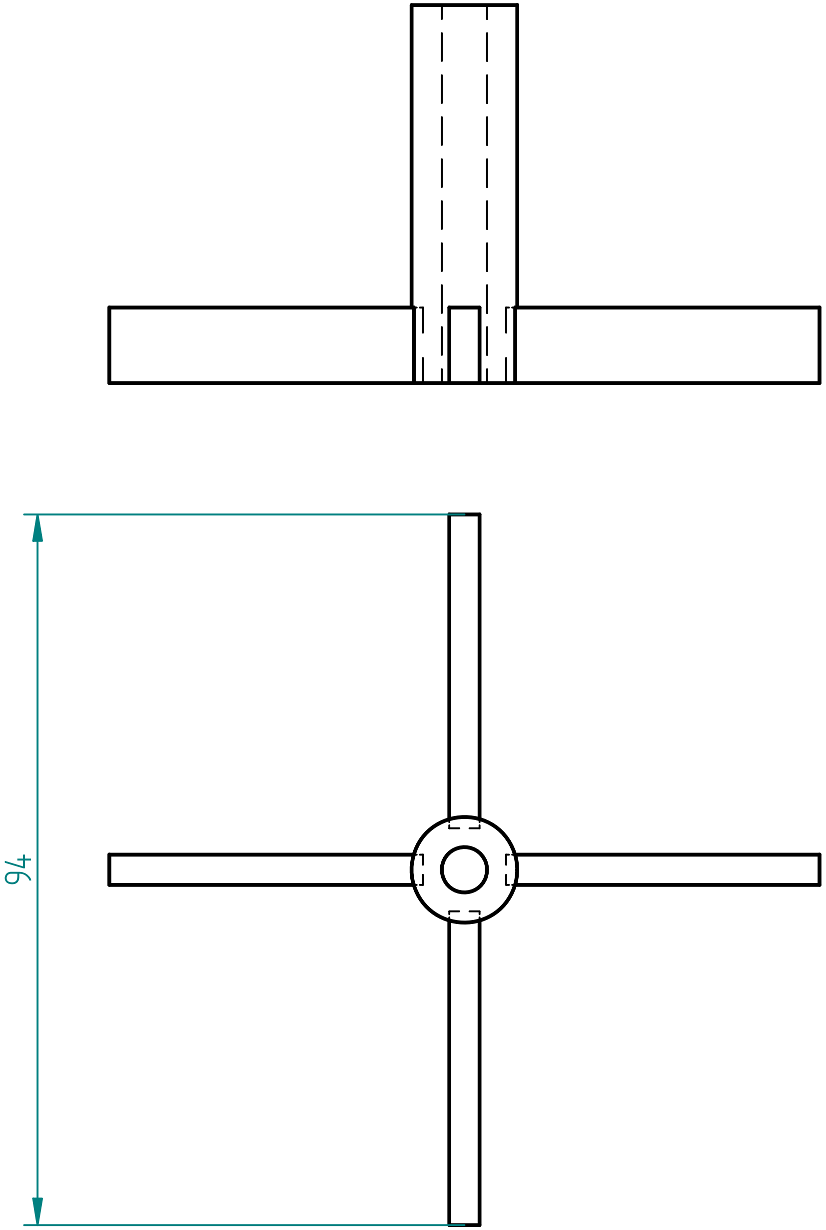

Terence Herron
Student#: 0407950R
Phone: 072 731 7338

Supervisor: Prof Skews

All Dimensions are in mm

Sub Assembly for needle guide

Terence Herron
Student#: 0407950R
Phone: 072 731 7338

Supervisor: Prof Skews

All Dimensions are in mm

Parts of needle guide

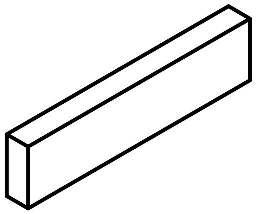

4 Required

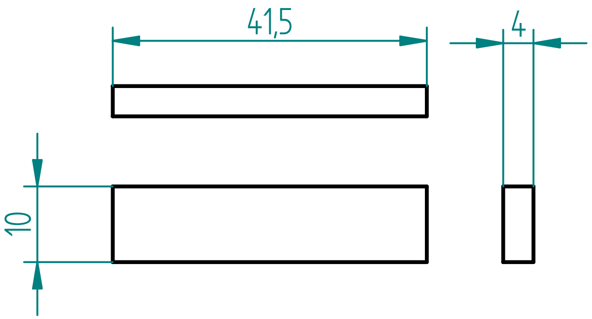

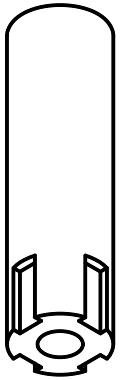

1 Required

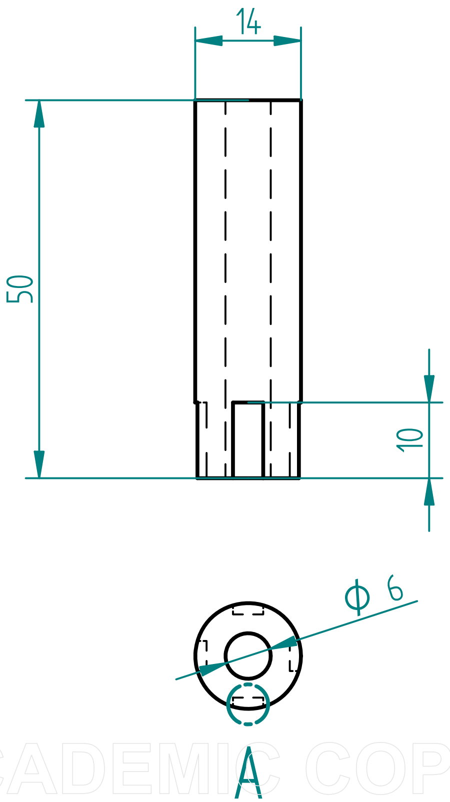

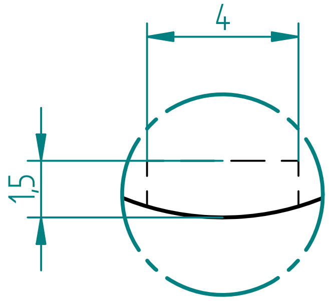

DETAIL A

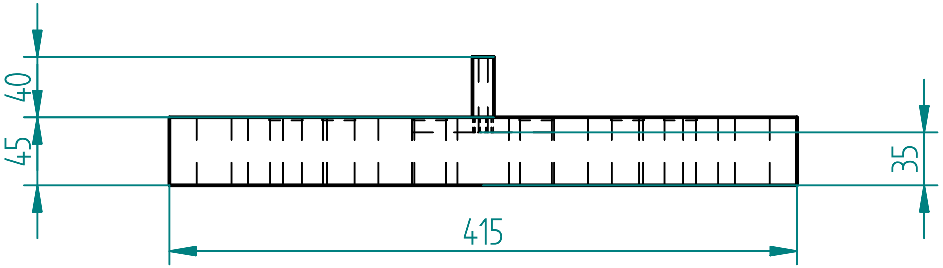

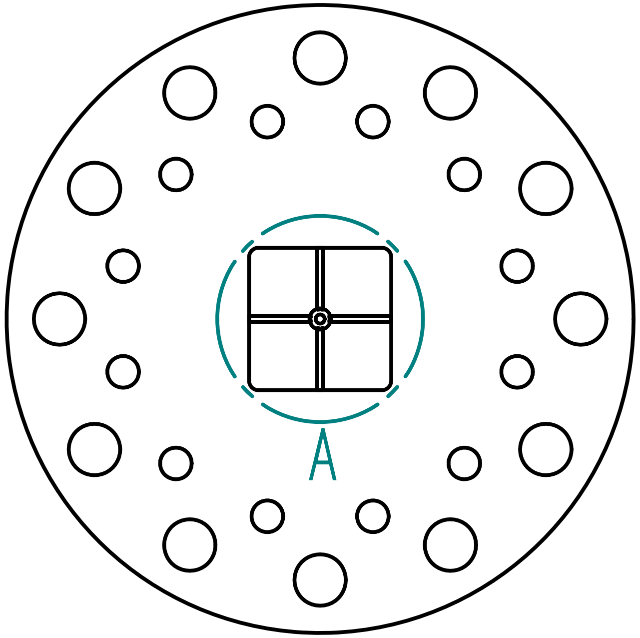

Terence Herron
Student#: 0407950R
Phone: 072 731 7338

Supervisor: Prof Skews

All Dimensions are in mm

Adapter flage with needle guide

PLEASE NOTE: Needle guide to be affixed opposite to smoothed side of flange

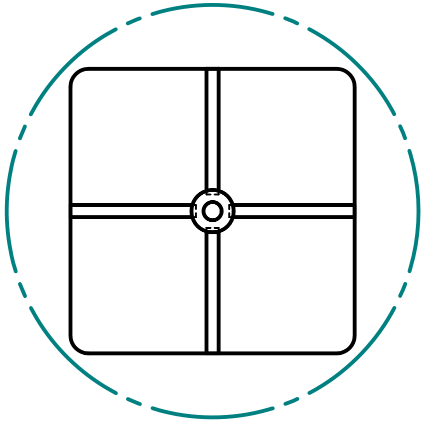
DETAIL A

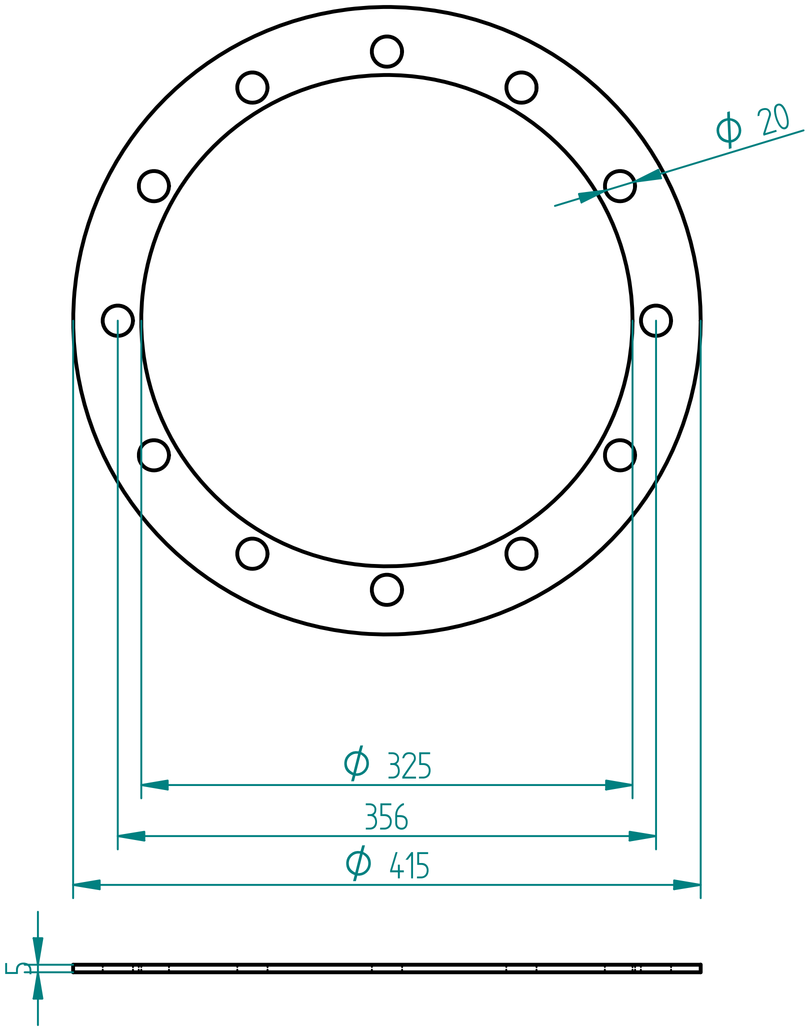

Terence Herron
0407950R
Phone 072 731 7338

Supervisor: Prof Skews

All Dimensions are in Millimeters

Front Bolt Ring

1 Required

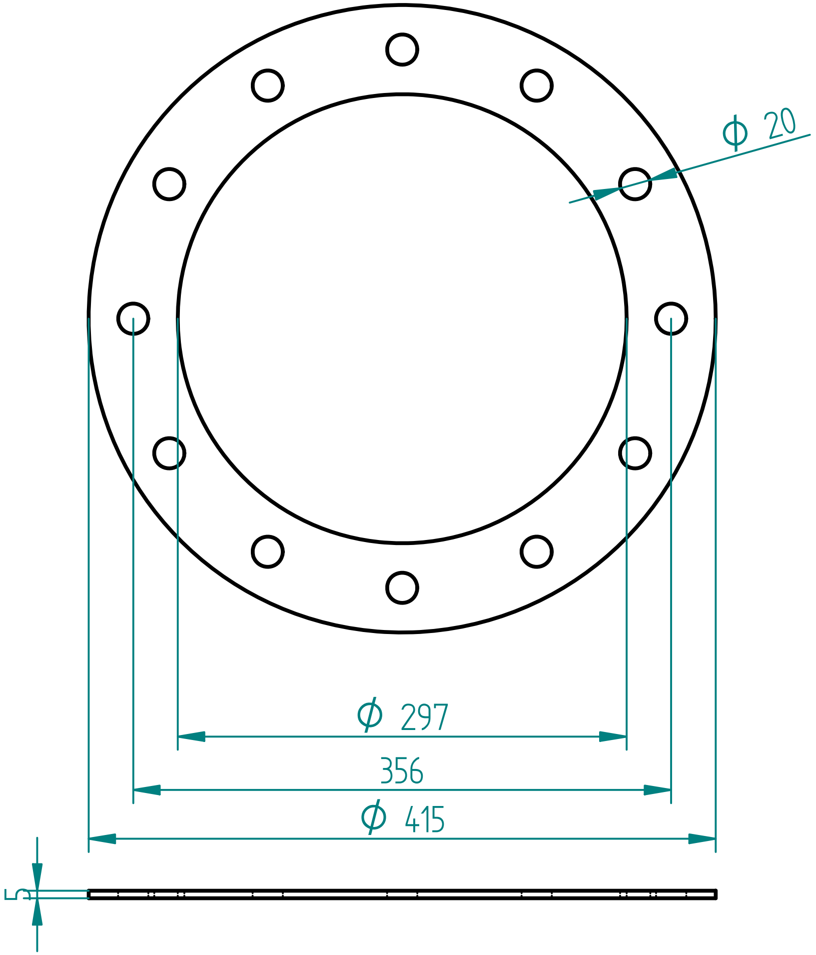

Terence Herron
0407950R
Phone 072 731 7338

Supervisor: Prof Skews

All dimensions are in millimeters

Back bolt Ring

1 Required

8.2.3. Calibration grids

The calibration grid’s grooves were CNC cut into the existing window frames. Once the grooves had been cut, wires were fitted into the grooves under tension and glued in place with epoxy.

The window frame for the 40° bifurcated section is centrally aligned, while the window frame for the 96° arrangement is offset.

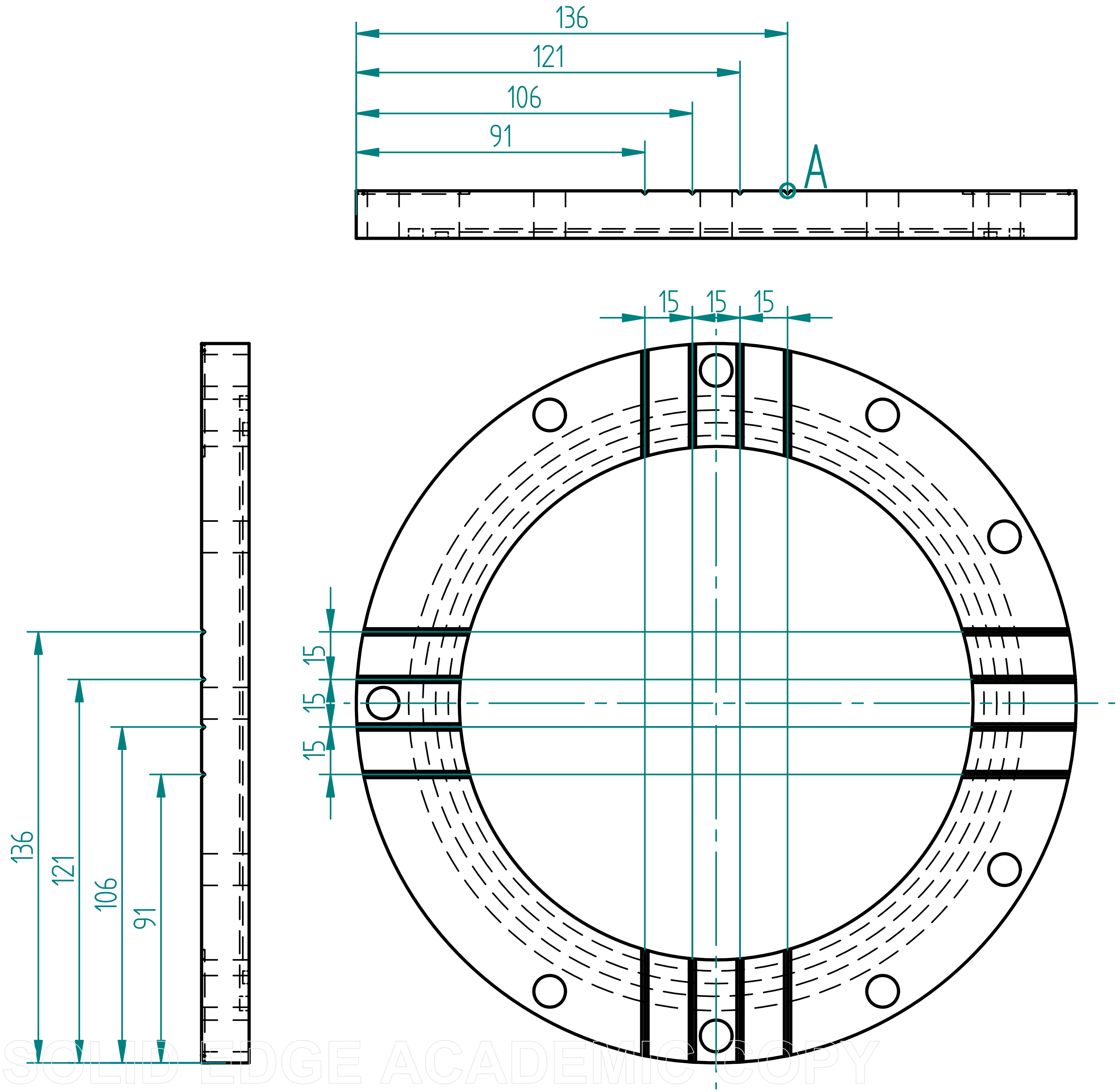

Terence Herron
Student#: 0407950R
Phone: 072 731 7338

Supervisor: Prof Skews

All Dimensions are in mm

Grooves for calibration grid

All grooves have a depth of 1mm

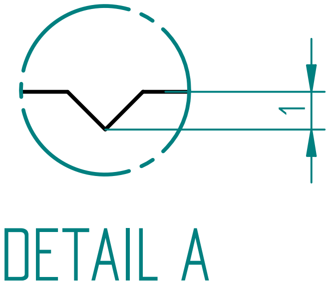

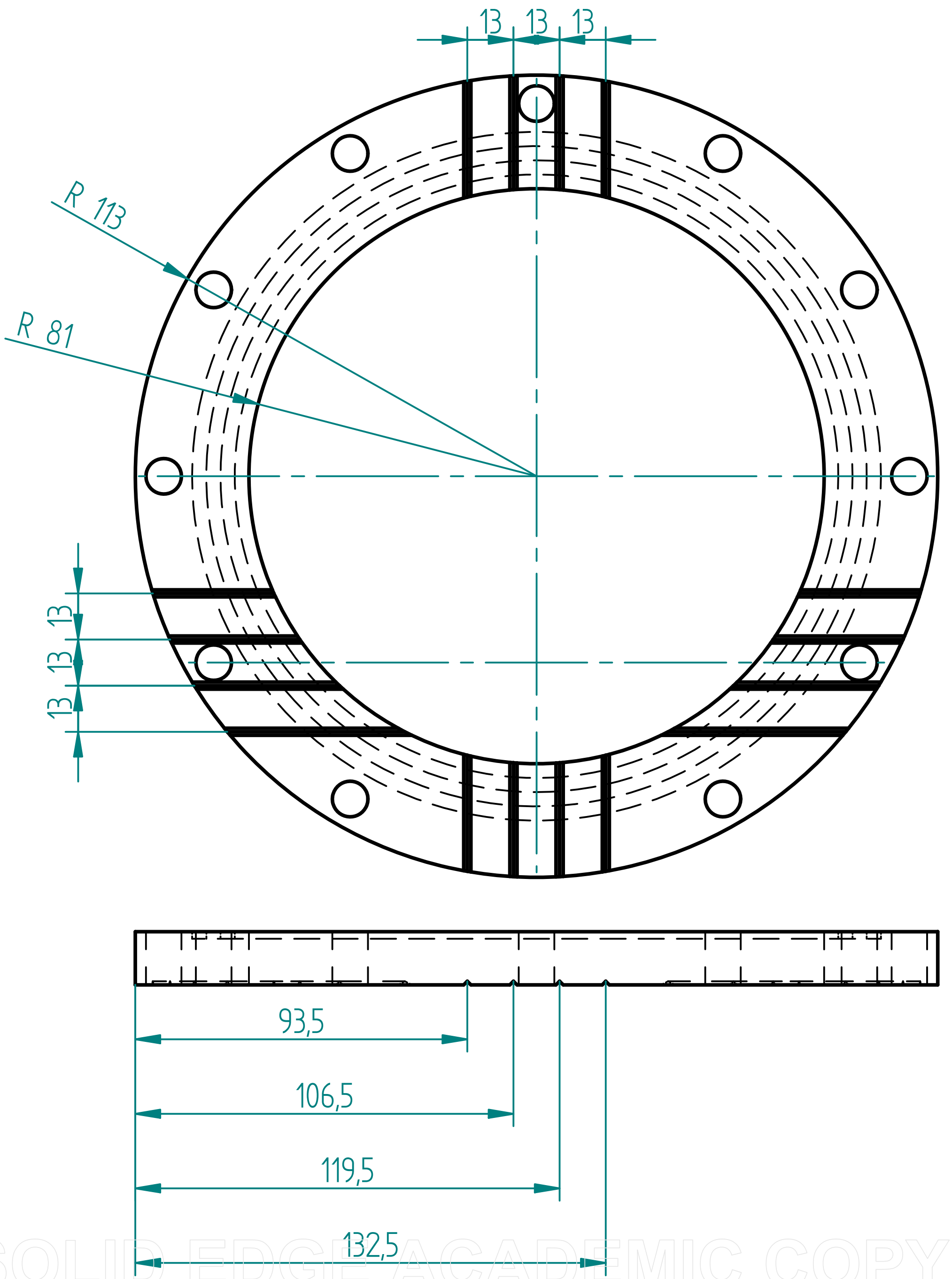

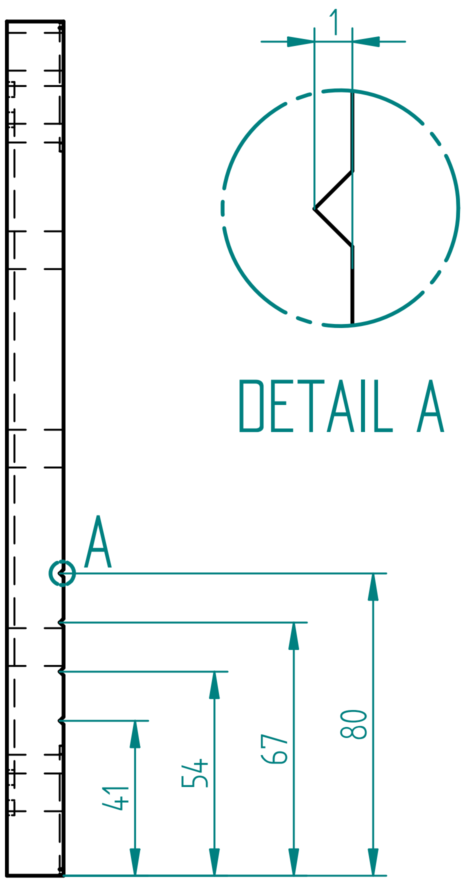

Terence Herron (0727317338)
Supervisor: Prof. Skews
All Dimensions are in mm
Grooves for calibration grid

8.3. Appendix C – Matlab code for image correction

The function *CoordTrans(X)* is described in the text and its code is included below. It was programmed by R. Paton.

```
function A = CoordTrans(X)

i = 1;
j = 1;
k = 1;

[a,b] = size(X);

while i <= b %columwise in X
    delx = X(i).delx;
    dely = X(i).dely;

    xg = X(i).xo - X(i).xo(a,1); %xg is measure of number of
points in matrix?
    yg = -(X(i).yo - X(i).yo(a,1));
    [c,d] = size(xg);
    while j <= c %getting polynomials of x-measured vs x-ideal
        Xpol(j,:) = polyfit(xg(j,:),[0:delx:((d-1).*delx)],d-1);
        j = j + 1;
    end
    j = 1;
    while j <= d %getting polynomials of y-measured vs y-ideal
        Ypol(j,:) = polyfit(yg(:,j)',[((c-1).*dely):-dely:0],c-1);
        j = j + 1;
    end
    j = 1;

    while j <= d %getting poly's of co-eff variation across x
polys
        Xpolx(j,:) = polyfit(yg(:,1),Xpol(:,j),c-1);
        j = j + 1;
    end
    j = 1;
    while j <= c %getting poly's of co-eff variation across y
polys
        Ypolx(j,:) =polyfit(xg(a,:),Ypol(:,j)',d-1);
        j = j + 1;
    end
    j = 1;

    xs = X(i).x - X(i).xo(a,1);
    ys = -(X(i).y - X(i).yo(a,1));

    f = length(xs);

    while k <= f
```

```
        while j <= d
            xpoli(j) = polyval(Xpolx(j,:),ys(k));
            j = j + 1;
        end
        j = 1;
        while j <= c
            ypoli(j) = polyval(Ypolx(j,:),xs(k));
            j = j + 1;
        end
        j = 1;

        xt(k) = polyval(xpoli,xs(k));
        yt(k) = polyval(ypoli,ys(k));

        k = k + 1;
        clear xpoli ypoli
    end
    k = 1;
    X(i).xtrue = xt;
    X(i).ytrue = yt;
    i = i + 1;
    clear xg yg  Xpol Ypol Xpolx Ypolx xs ys c xt yt
end

A = X;
```

The inputs to the code for a typical image follow. The matrix of variables x, xo, y and yo were created previously were updated by copying and pasting from an excel spreadsheet containing the measurements from each image.

```
X(1).delx = 1;%length in meters of the grid spacings x
X(1).dely = 1;%length in meters of the grid spacings y

%96 degree information
%grid co-ordinates numbered from left to right, top to bottom (x)
X(1).xo = xo;
%grid co-ordinates numbered from left to right, top to bottom (y)
X(1).yo = yo;
%points to be calibrated co-ords (x)
X(1).x = x;
%points to be calibrated co-ords (y)
X(1).y = y;

A = CoordTrans(X);
```

8.4. Appendix D – All result images

8.4.1. 40° Results

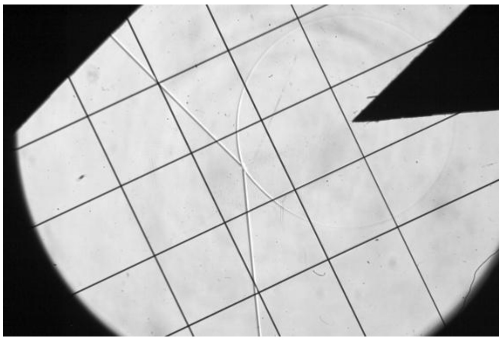

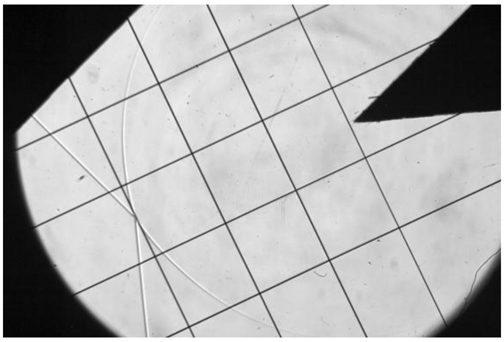

(Test 79, M = 1.032, χ=0.612°, ψ= -0.89mm) (Test 80, M = 1.029, χ=0.291°, ψ= -0.89mm)

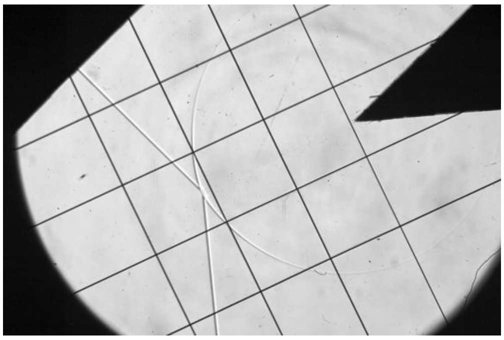

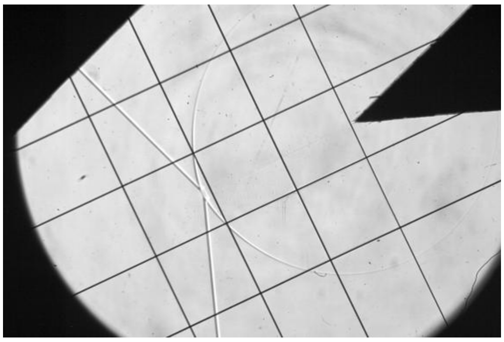

(Test 81, M = 1.041, χ=1.209°, ψ= -0.18mm) (Test 82, M = 1.047, χ=1.471°, ψ= 0.00mm)

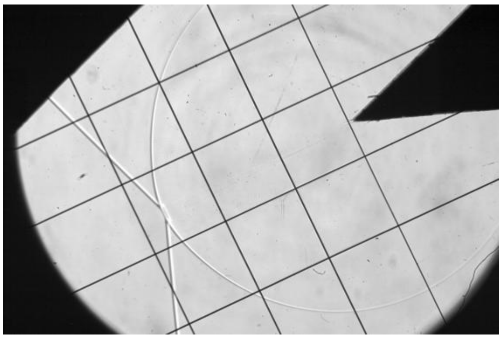

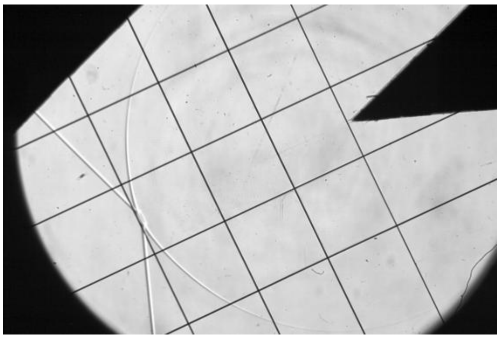

(Test 85, M = 1.053, χ=1.821°, ψ= 0.36mm) (Test 86, M = 1.044, χ=1.401°, ψ= -0.36mm)

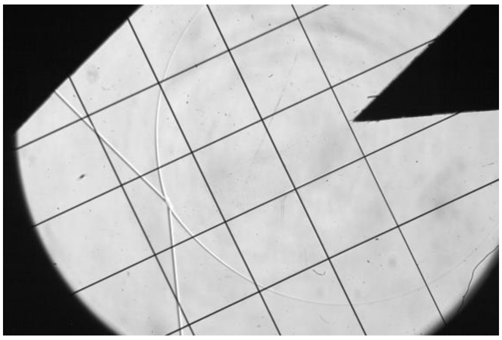

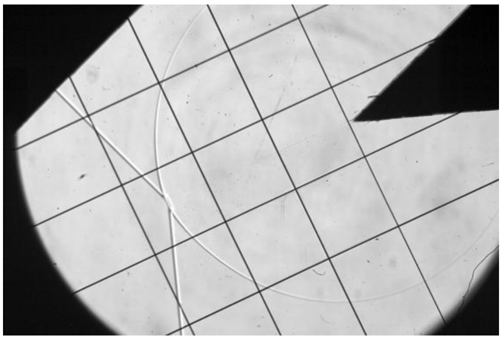

(Test 89, M = 1.035, χ=0.945°, ψ= -0.71mm) (Test 94, M = 1.050, χ=1.608°, ψ= -0.73mm)

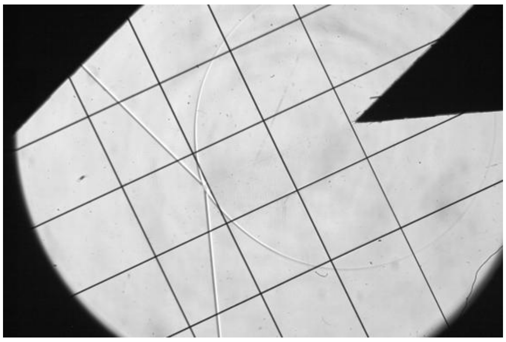

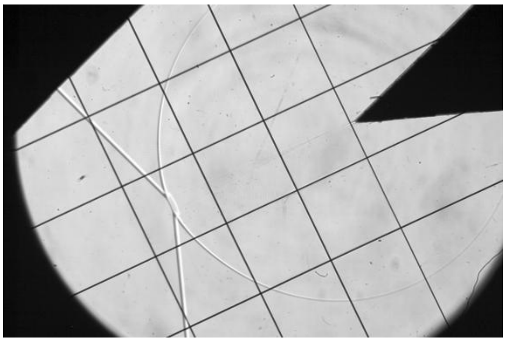

(Test 96, M = 1.037, χ=0.786°, ψ= -0.90mm) (Test 99, M = 1.061, χ=2.558°, ψ= -0.73mm)

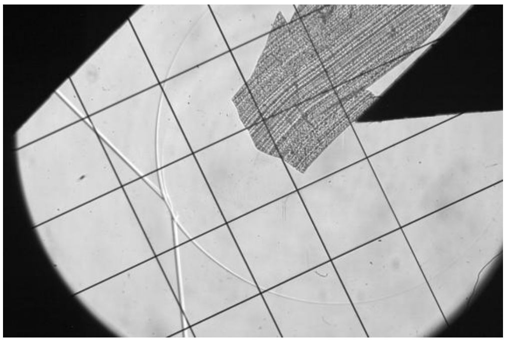

(Test 109, M = 1.062, χ=2.423°, ψ= -0.37mm)

8.4.2. 96° Results

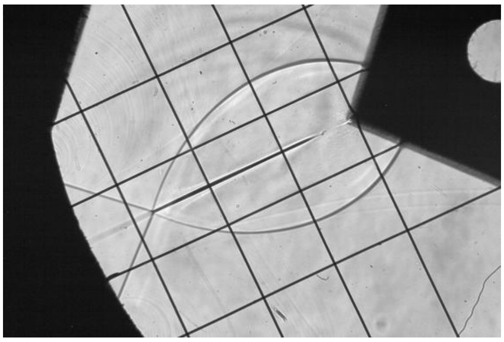
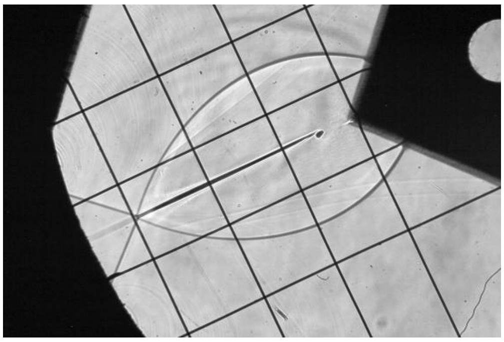

(Test 178, M = 1.489, χ=0.321°, ψ=-0.59mm)(Test 179, M = 1.505, χ=0.287°, ψ=-0.30mm)

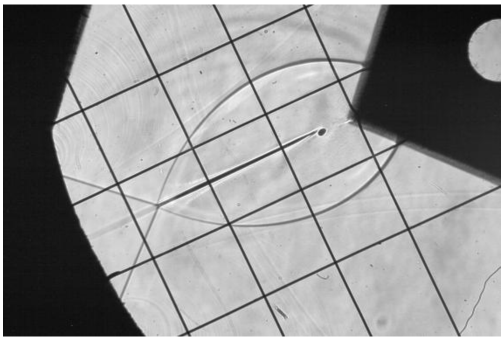
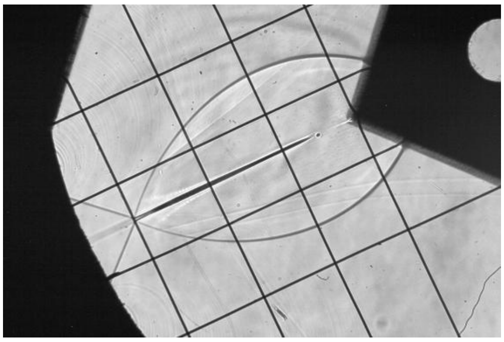

(Test 180, M = 1.502, χ=0.340°, ψ= 0.52mm)(Test 181, M = 1.528, χ=0.332°, ψ=-0.29mm)

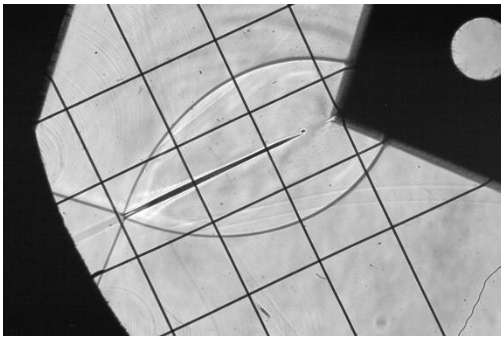
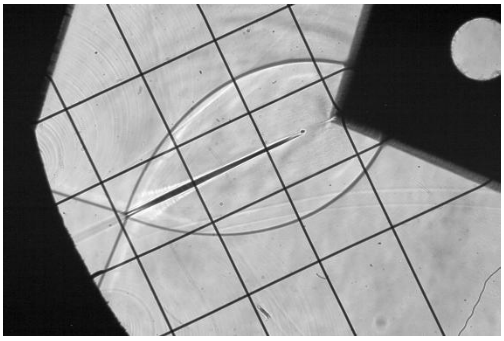

(Test 195, M = 1.560, χ=0.470°, ψ= 0.00mm)(Test 199, M = 1.539, χ=0.333°, ψ=-0.12mm)

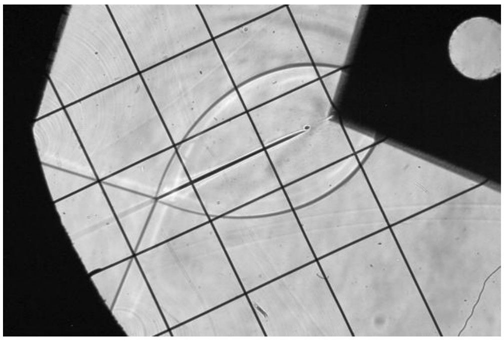
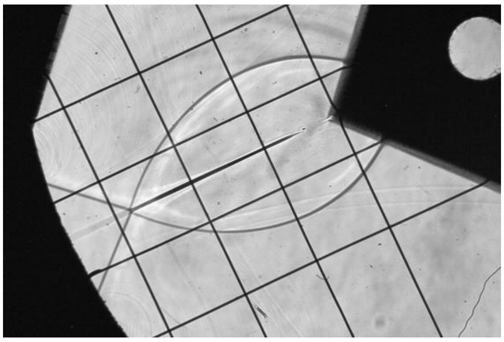

(Test 214, M = 1.509, χ=0.266°, ψ=-0.52mm)(Test 216, M = 1.505, χ=0.329°, ψ=-0.52mm)

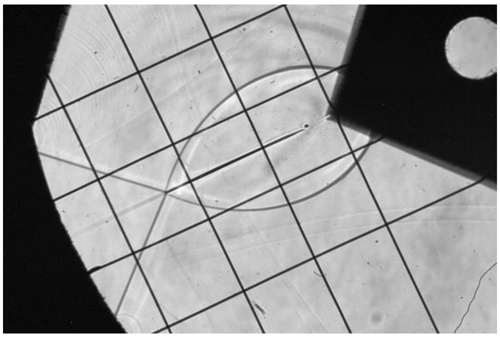
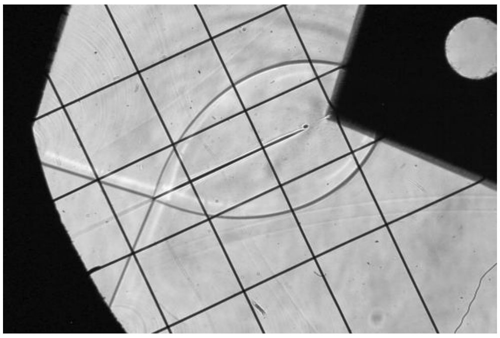

(Test 217, M = 1.489, χ=0.263°, ψ=-0.67mm)(Test 218, M = 1.475, χ=0.253°, ψ=-0.81mm)

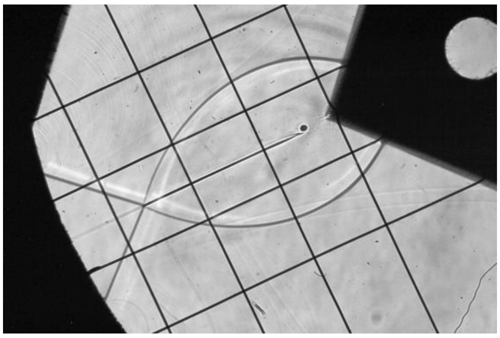
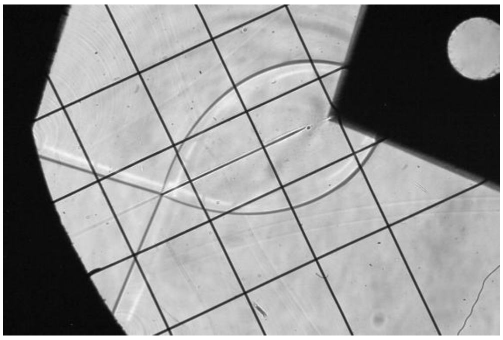

(Test 220, M = 1.453, χ=0.207°, ψ=-0.45mm)(Test 222, M = 1.443, χ=0.202°, ψ= 0.25mm)

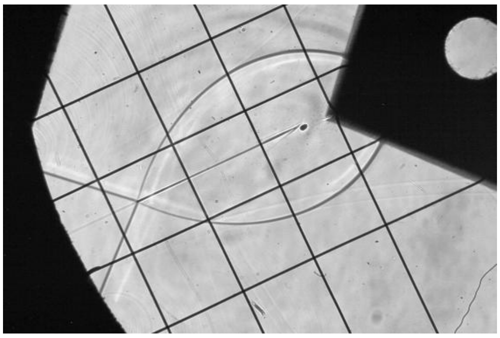
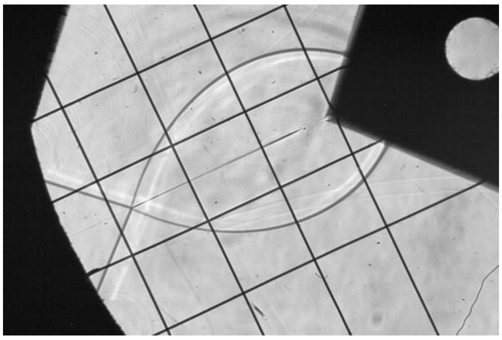

(Test 223, M = 1.433, χ=0.183°, ψ= 0.18mm) (Test 239, M = 1.420, χ=0.091°, ψ=0.32mm)

8.5. Appendix E - Matlab code for trend-line fitting

The Matlab code used to create the multivariate trend-line is based on a function with variable co-efficients that is created prior to calling the *nlinfit*, *nlparci* and *nlpredci* functions. The quadratic multivariate function *quad* is included below as it is the most general. Linear and single variable trend line fits require their own functions, which are variations on the theme of *quad*.

```
function y = quad(gamma,ex)

g1=gamma(1);
g2=gamma(2);
g3=gamma(3);
g4=gamma(4);
g5=gamma(5);

f=ex(:,1);
s=ex(:,2);

y=g1*f.*f+g2*f+g3*s.*s+g4*s+g5
```

The variables *ex*, *n* and *gamma* are created by the following code, and are updated by copying and pasting from excel data created from measurements of temperature and transducer traces.

```
ex = [ -.589    .268    ;
       -.298    .309    ;
       0.518    .401    ;
       -.294    .357    ;
       0.0      .496    ;
       -.12     .45     ;
       0.522    .369    ;
       -.521    .374    ;
       -.666    .305    ;
       0.184    .139    ;
       0.315    .123    ]    ;
```

```
Mach =
[1.4892;1.5048;1.5017;1.5279;1.5603;1.5389;1.5088;1.5050;1.4888;1.
4747;1.4531;];

gamma       = [-.002; .025; -.002; .025; 1.013];
```

The functions *nlinfit*, *nlpredci* and *nlparci* are then called, with settings on nlinfit being called by 'options' and other variables used internally to calculate the co-efficients of a Robust non-linear multivariate trend line that is statistically the best fit to the data.

```
%nlinfit,nlpredci&nlparci with all the variables config'd for
Robust
options=statset('Robust','on');
%'Robust' 'on' - makes robust curve fitting happen
[gammahat,resid,J,sigma,mse]=nlinfit(ex,Mach,@quad,gamma,options);
%nlinfit with modification
[y,delta]=nlpredci(@quad,ex,gammahat,resid,'covar',sigma,'mse',mse
,'alpha',0.05);
%new Mach values and their 95% bounds
gammaci=nlparci(gammahat,resid,'covar',sigma);
%confidence intervals on the fitted data
opd = [Mach y delta];
%data collecting matrix
```

The above calculation gives points on each side of each data point indicating the 95% confidence interval. Robust trend lines are then fitted to these points.

```
%%%Robust 95% trendlines for the new variables%%%
Machminus = y + delta;
[gammaminushat,residminus,Jminus,sigmaminus,mseminus]=nlinfit(ex,M
achminus,@quad,gamma,options);
[yminus,deltaminus]=nlpredci(@quad,ex,gammaminushat,residminus,'co
var',sigmaminus,'mse',mseminus,'alpha',0.05);
gammaminusci=nlparci(gammaminushat,residminus,'covar',sigmaminus);
Machplus = y - delta;
[gammaplushat,residplus,Jplus,sigmaplus,mseplus]=nlinfit(ex,Machpl
us,@quad,gamma,options);
[yplus,deltaplus]=nlpredci(@quad,ex,gammaplushat,residplus,'covar'
,sigmaplus,'mse',mseplus,'alpha',0.05);
gammaplusci=nlparci(gammaplushat,residplus,'covar',sigmaplus);
```